Tese de Doutorado

Simulation Methods for Singlet Excitons: Spectra, Dynamics and Diffusion

Leonardo Evaristo de Sousa
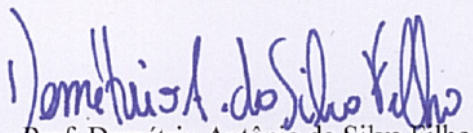
Orientador: Prof. Demétrio Antônio da Silva Filho

"SIMULATION METHODS FOR SINGLET EXCITONS: SPECTRA, DYNAMICS AND DIFFUSION."
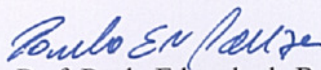
Por

LEONARDO EVARISTO DE SOUSA.

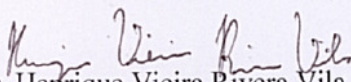Tese submetida ao Instituto de Física da Universidade de Brasília como parte dos requisitos para a obtenção do grau de Doutor em Física.

Aprovada por:

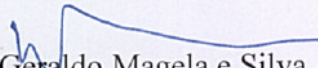Prof. Demétrio Antônio da Silva Filho
IF/UnB

Prof. Paulo Eduardo Narcizo de Souza
IF/UnB

Prof. Paulo Eduardo de Brito
FUP/UnB

Dr. Henrique Vieira Rivera Vila
CMB/DF

Prof. Dr. Geraldo Magela e Silva
Coordenador de Pós-Graduação
Instituto de Física

Pour soulever un poids si lourd,
Sisyphe, il faudrait ton courage!
Bien qu'on ait du coeur l'ouvrage,
L'Art est long et le Temps est court.

Charles Baudelaire

Resumo

A habilidade de simular fenômenos físicos reflete nosso entendimento a respeito desses fenômenos. Ao mesmo tempo, provê uma área de testes para novas ideias. No campo da eletrônica orgânica, há muitos processos relevantes que afetam o funcionamento de dispositivos como os diodos emissores de luz orgânicos (OLEDs, em inglês) e dispositivos fotovoltaicos orgânicos (OPVs, também em inglês). Entre esses processos, é possível listar a absorção de luz, a fluorescência e a difusão de éxcitons em materiais orgânicos. Neste trabalho, várias técnicas são analisadas e utilizadas para simular tais processos na tentativa de obter conhecimento que pode ser útil para o design racional de dispositivos optoeletrônicos. Os métodos usados aqui vão de modelos analíticos e cálculos de química quântica até algoritmos genéticos e modelos de Monte Carlo Cinético. Comparações são feitas com resultados experimentais para ou prover explicaões acerca de fenômenos observados ou verificar predições feitas pelos modelos. Resultados incluem a obtenção de informação a respeito da dependência de temperatura na difusão de éxcitons em moléculas de para-hexafenil e α-sexitiofeno, efeitos de dimensionalidade e morfologia na difusão de éxcitons assim como a predição de comprimentos de difusão para várias moléculas.

Abstract

The ability of simulating physical phenomena reflects our understanding of these phenomena. At the same time, it provides testing ground for new ideas. In the field of organic electronics, there are many relevant processes that affect the functioning of devices such as organic light emitting diodes (OLEDs) and organic photovoltaic devices (OPVs). Among these processes, it is possible to list light absorption, fluorescence and exciton diffusion in organic materials. In this work, several techniques are presented and used to simulate such processes in an attempt to gain physical insight that could be useful for the rational design of optoelectronic devices. The methods employed here range from analytical models and quantum chemical calculations to genetic algorithms and Kinetic Monte Carlo (KMC) models. Comparisons with experimental results are made either to provide explanations of observed phenomena or to verify predictions made by the models. Results include the acquiring of information regarding the temperature dependence of exciton diffusion in para-hexaphenyl and α-sexithiophene molecules, the effects of dimensionality and morphology on exciton diffusion as well as the prediction of exciton diffusion lengths for various molecules.

LIST OF TABLES

LIST OF FIGURES

CHAPTER 1

INTRODUCTION

This journey begins on February 2015. At that time, fellow researchers in Denmark had produced a device composed of alternating layers of para-hexaphenyl (P6P) (Figure 1.1) and α-sexithiophene (6T) (Figure 1.2) molecules. This device was excited with a laser tuned to the absorption band of the P6P molecules, which fluoresce in the blue region of the spectrum. A blue glow was observed particularly at low temperatures, but as temperature increased, the emitted light started to change towards green, which is the part of the spectrum where 6T molecules fluoresce[2]. This behavior, in which light is emitted from the molecules that were not originally excited, pointed to the presence of a phenomenon of energy transfer.
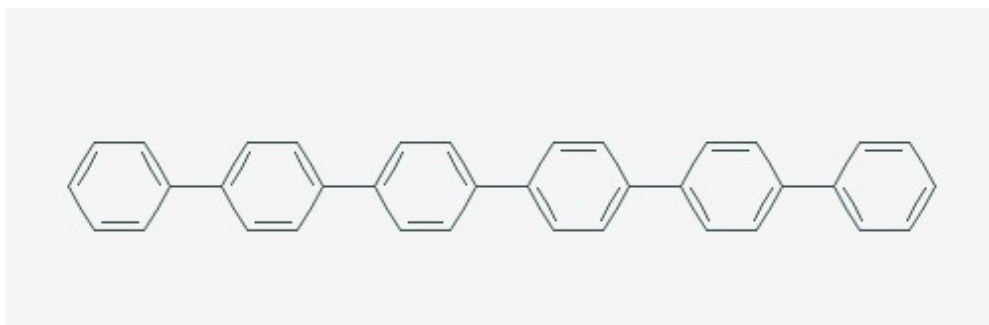
Figure 1.1: The para-hexaphenyl (P6P) molecule.
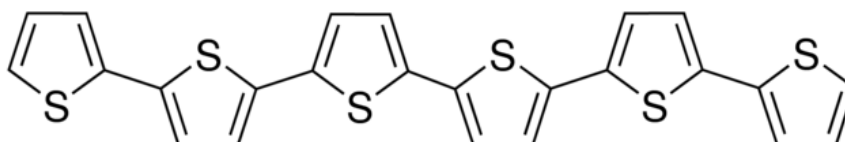
Figure 1.2: The α-sexithiophene (6T) molecule.

Many mechanisms are at play in such an experiment. First, when light is absorbed by the material, an exciton is generated. An exciton is an electron-hole pair that is bound by the Coulomb

interaction between its constituents. Due to the typically low relative permittivity of organic materials, excitons in organic semiconductors tend to be strongly bound and very much localized - the so-called Frenkel excitons[6]. As such, these excitons behave as quasiparticles that are able to move around in the material. This movement corresponds actually to a non-radiative process of energy transfer from an excited molecule - the donor - to a molecule in the ground state - the acceptor. The particular kind of process responsible for exciton transfer depends mostly on exciton spin.

Excitons may be found in singlet or triplet states. Singlet excitons are produced from light absorption whereas triplet excitons must be generated from singlets by means of intersystem crossing[7]. Triplet excitons are transferred thanks to the Dexter energy transfer[8], a process in which the donor's excited electron is transferred to the acceptor with the simultaneous transfer of a ground state electron to the donor molecule. Singlet excitons may also undergo Dexter transfer, but the main process responsible for its diffusion is the Förster resonance energy transfer[9]. In this latter process, the excitation energy is transfered from donor to acceptor by the simultaneous deexcitation of the donor and excitation of the acceptor molecule. No electron exchange takes place, however.

To better understand the behavior of these excitons in organic semiconductors, the focus of this work will be simulations. Simulations have the double purpose of explaining observed phenomena and making predictions. Here, different types of simulations are put to work for the purposes of explaining experimental results regarding singlet exciton dynamics and of predicting diffusion related properties that are key to the functioning of organic optoelectronic devices.

The Danish experiment regarding P6P and 6T will serve as the main motivation, as it was my first contact with the phenomena described here. In this sense, since the excitons in the experiment in question were singlet, the discussion here will be restricted to the behavior of singlet excitons and thus to the Förster mechanism.

In research papers, results are presented in the most linear and didactic order so that they are communicated more clearly. The actual path research takes is seldom as linear. Here, I choose to present the work roughly in the order that it was produced, trying to show at each step how one idea gave birth to the next. It is curious to find that research subjects to which one dedicates oneself during the PhD work eventually take life of their own and one ends up studying subjects that were not even on the radar at the beginning of the four year period. In this sense, it is precisely at the thesis - for which there is only one author - that the opportunity presents itself for producing a more personal account of the work done.

This work is divided as follows: Chapter 2 is concerned about the methods used for spectrum simulation, their reliability and the conditions under which they may be applied. Once the basic conditions for Förster transfers are established, the focus moves to the analysis of exciton dynamics in the multilayered P6P-6T system. Chapter 3 presents a technique that is able to interpret experimental results obtaining insight on physical properties of the system that would be otherwise difficult to measure. This technique consists of a combination of quantum chemical calculations, a Kinetic Monte Carlo model and a genetic algorithm. Results show the need to

account for exciton-exciton interactions and provide estimates for the many parameters necessary to calculate the rates of Förster transfer in the two materials.

Building on the previous results, exciton diffusion is the subject of Chapter 4. The effects of temperature and dimensionality are studied and estimates are provided for diffusion coefficients and exciton diffusion lengths. Results are presented and compared with experimental data. Furthermore, the chapter concludes with a model for ab initio determination of singlet exciton diffusion lengths. The model is tested for various molecules of interest in the field of organic electronics and results are again compared to experimental reports.

Chapter 5 presents the conclusions and perspectives for future studies that may derive from the work presented here. Finally, the papers published during the thesis work are presented. Hopefully, some reader may eventually find it useful to find out what I learned, how I learned.

CHAPTER 2

SIMULATING ABSORPTION AND EMISSION SPECTRA

Learning a Craft

As mentioned in the Introduction, singlet excitons move by means of the Förster resonance energy transfer. For this process to happen, the existence of an overlap between the emission spectrum of the donor and absorption spectrum of the acceptor is a requirement[6]. This will be developed further in the next chapters. With this requirement in mind, the first theoretical contribution may then come from demonstrating that such a transfer is indeed possible by simulating the spectra of the molecules involved and checking for the existence of overlap between them.

Absorption and emission spectrum simulations are of great importance in materials science, particularly when it comes to efforts in designing devices whose functioning rely on the emission or absorption of light, such as light emitting diodes and photovoltaic cells. For the calculation of UV-Vis spectra, the simplest method consists in performing density functional theory (DFT) calculations to obtain optimized molecular geometries followed by time-dependent DFT (TD-DFT) single point calculations for several excited states. This procedure yields excitation energies as well as oscillator strengths associated with each electronic transition. This method in and of itself has however an important shortcoming: it lacks vibrational resolution. An approach that addresses this issue makes use of the Franck-Condon (FC) approximation, to which we now turn.

The Franck-Condon Approximation

In the Born-Oppenheimer approximation, the wave function for a system of electrons and nuclei is given by

$$\Psi_n(\vec{r}, \vec{R}) = \psi_k(\vec{r}, \vec{R})\phi_{kl}(\vec{R}),\tag{2.1}$$

where $\vec{r}$ denotes the set of position vectors of the electrons and $\vec{R}$ the set of position vectors of the nuclei. The function $\psi_k(\vec{r}, \vec{R})$ is the electronic wave function, depending parametrically on the positions of the nuclei. It is an eigenfunction of the electronic Hamiltonian $H_e = T_r + V(\vec{r}, \vec{R})$, T_r being the kinetic energy operator for electrons,

$$H_e\psi_k(\vec{r}, \vec{R}) = \varepsilon_k(\vec{R})\psi_k(\vec{r}, \vec{R}),\tag{2.2}$$

and $\phi_{kl}(\vec{R})$ representing the nuclear wave function, which obeys

$$H_v\phi_{kl}(\vec{R}) = E_{kl}\phi_{kl}(\vec{R}),\tag{2.3}$$

where $H_v = T_R + \varepsilon_k(\vec{R})$ is the nuclear Hamiltonian with v standing for vibrational, for we are to work in the harmonic approximation.

The spontaneous emission rate, obtained from Quantum Mechanics by means of time dependent perturbation theory, is given by [10]

$$\sigma_{em} = \frac{4\omega^3}{3c^3\hbar} \sum_{i,m,f,n} P_{im}(T) \left|\langle\phi_{fn}|M_{fi}|\phi_{im}\rangle\right|^2 \delta(E_{fn} - E_{im} + \hbar\omega),\tag{2.4}$$

where the indices i and f refer to the initial and final electronic states whereas m and n refer respectively to the initial and final vibrational states. $P_{im}(T)$ is the Boltzmann distribution at temperature T, M_{fi} is the electronic dipole operator, ω is the angular frequency, c is the speed of light, and δ is the Dirac delta function.

In the Franck-Condon approximation the electronic dipole is considered to be a constant, which allows us to remove it from inside the bracket, resulting in

$$\sigma_{em} = \frac{4\omega^3}{3c^3\hbar} \sum_{i,m,f,n} M_{fi}^2 P_{im}(T) \left|\langle\phi_{fn}|\phi_{im}\rangle\right|^2 \delta(E_{fn} - E_{im} + \hbar\omega).\tag{2.5}$$

The term $\langle\phi_{fn}|\phi_{im}\rangle$ is the so-called Franck-Condon factor. Now, restricting the calculation for emissions from the first electronic excited state ($i = 1$) to the electronic ground state ($f = 0$), we obtain

$$\sigma_{em} = \frac{4\omega^3}{3c^3\hbar} \sum_{m,n} M_{01}^2 P_{1m}(T) \left|\langle\phi_{0n}|\phi_{1m}\rangle\right|^2 \delta(E_{0n} - E_{1m} + \hbar\omega).\tag{2.6}$$

At 0 K temperature, the only vibrational level populated in the initial state is the ground state. Finally, we must also substitute the delta function with a Gaussian function in order to take into account the broadening of the lines. The result is

$$\sigma_{em} = \frac{4\omega^3}{3c^3\hbar} \sum_n M_{01}^2 \left| \langle \phi_{0n} | \phi_{10} \rangle \right|^2 G(E_{0n} - E_{10} + \hbar\omega, \delta),$$

(2.7)

where now δ refers to the broadening factor. An analogous results is obtained for the absorption spectrum.

The FC simulations use results obtained from geometry optimizations and frequency calculations performed in both the ground and excited states[11], which can be done using DFT and TD-DFT. These calculations can be very time consuming - specially those done in the excited state -, but the actual spectrum phase is usually extremely fast. However, there are difficulties with the FC method that are completely independent from computational capacity. These difficulties become relevant in particular because of their relation to a characteristic that makes some organic molecules of interest to applications: their flexibility. For instance, molecules that present a twisted geometry at the ground state, but a completely planar one at the excited state result in failure for the FC approximation. This is precisely the case of P6P and 6T. At this point, then, I was assigned to test an alternative solution.

The Nuclear Ensemble Method

The Newton-X software[12] is able to simulate absorption and emission spectra, but instead of calculating the overlap integrals directly, it relies on a semi-classical approximation to the electronic dipole operator to obtain an expression for the emission rate - or for the absorption cross section - which in its turn is evaluated by means of an average over an ensemble of nuclear geometries. This is the so-called nuclear ensemble (NE) method[13].

The program requires optimized geometries and normal modes for the initial state - ground state for absorption, excited state for emission. Then, it samples a series of geometries from the probability distribution associated with a set of coupled harmonic oscillators and performs single point TD-DFT calculations on each to obtain the vertical excitation energies and oscillator strengths. Finally, the spectra are broadened by Gaussian or Lorentzian line shapes. For the emission rate, the method yields the following expression

$$\sigma_{em} = \frac{2e^2}{mc^3\hbar^2} \left[\frac{1}{N} \sum_{j=1}^{N} \Delta E_{10}^2(\vec{R}_j) f_{01}(\vec{R}_j) G(\Delta E_{10}(\vec{R}_j) - \hbar\omega, \delta) \right],$$

(2.8)

in which f_{01} is the oscillator strength of the S_0 to S_1 transition and ΔE_{10} its corresponding energy. N refers to the number of sampled geometries employed, usually in the hundreds. Details regarding the derivation of this expression and its counterpart used for absorption spectra can be found at the end of this chapter.

From a computational standpoint, the NE method is much more demanding, since besides the optimizations and normal mode analyses required for FC approximation, it also needs hundreds of single point TD-DFT calculations. On the other hand, these calculations may be parallelized, as they are completely independent.

Having understood the theoretical and practical aspects of these quantum chemical calculations, I now had tools that would prove valuable for different collaborations. The comparison between methodologies for spectrum simulations was going to be my first project.

Comparing Methodologies

To analyze how the Franck-Condon approximation and the nuclear ensemble method fared against one another, we chose a set of small molecules composed of benzene or thiophene rings that differed mainly by the way these rings were connected (Figure 2.1). One set of molecules was flexible whereas the other was rigid. This would allow us to understand the effects produced by the changes in molecular geometry upon excitation.

Full geometry optimizations and normal mode analysis were performed for all molecules in Figure 2.1 for both the ground and first excited states. This was done for three functionals, B3LYP, M062X and wB97XD along with the 6-31G(d) basis set using the Gaussian 09 program suite[14]. We then used the Franck-Condon approximation to calculate the emission spectra of these molecules.

A measurement of the quality of the simulated spectrum is given by the spectrum progression, defined as

$$S = \sum_n |\langle \phi_{0n} | \phi_{10} \rangle|^2 , \tag{2.9}$$

where ϕ_{mn} are the vibronic wave functions. The first index refers to the electronic state, whereas the second refers to vibrational levels. This parameter measures the amount of overlap between the ground and excited states wave functions and should equal to one. The farther away from one, the less reliable is the simulated spectrum.

Results show a large variation of spectrum progression among the different molecules and functionals used. To make the connection between this parameter and geometry modifications upon excitation, we needed a measurement of geometrical changes. Since the main difference between the molecules under study was their flexibility, we chose a measure of molecular planarity
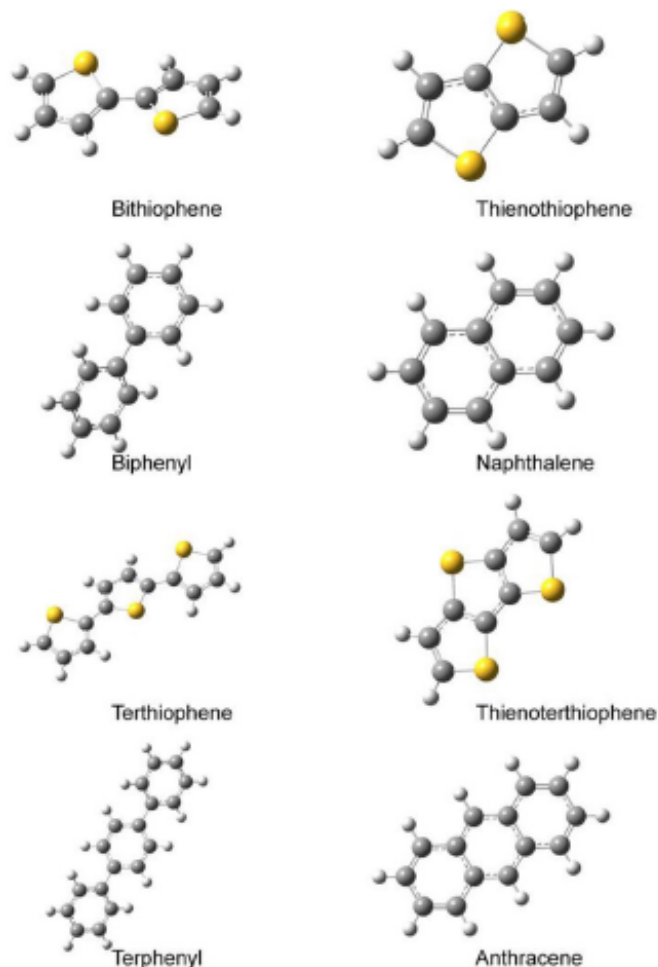
Figure 2.1: Flexible and rigid molecules used for the comparison between Franck-Condon and nuclear ensemble methods for spectrum simulations. Reproduced from reference [1].

given by

$$D = \sum_k \theta_k \tag{2.10}$$

where θ_k is the dihedral angle between two rings. The summation is extended to all pairwise combination of rings. When the molecule goes from the ground to excited state, this parameter D may change in value. The various spectrum progressions plotted as a function of the change in D can be seen in Figure 2.2. This figure shows a clear negative correlation between spectrum progression and changes in dihedral angles. Furthermore, it shows that the different functionals predict changes in molecular geometry that become larger as we go from B3LYP to M062X to wB97XD. The flexible molecules studied here all went from a twisted to planar conformation when excited. The rigid molecules, on the other hand, remained in their original planar conformation with the exception of thienothiophene, which actually becomes less planar when excited. Overall, the important conclusion is that the Franck-Condon approximation is inappropriate for spectrum simulations of flexible molecules.

Given the results above, we went on to test the nuclear ensemble method. The first parame-
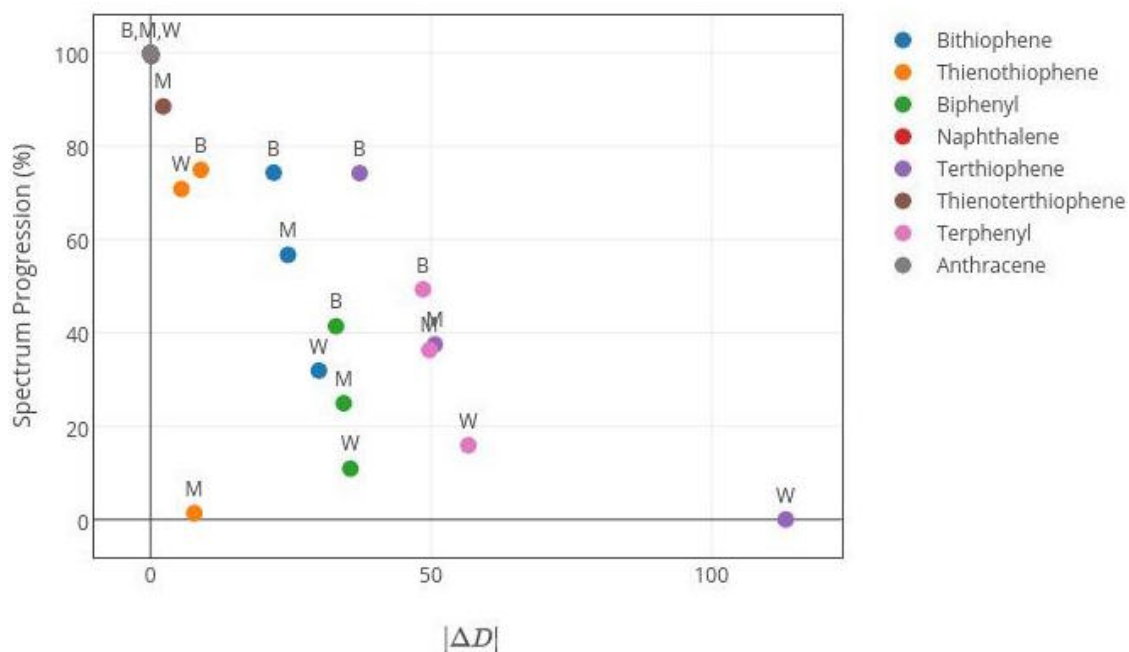
Figure 2.2: Spectrum progressions for the set of molecules shown in Figure 2.1. B, M and W represent results obtained with the B3LYP, M062X and wB97XD functionals, respectively. Reproduced from reference [1].

ter that must be taken into account in this approach is the number of molecular geometries that are sampled. We tested values spanning three orders of magnitude, sampling 50, 500 and 5000 geometries. From a computational standpoint, the need for high numbers of sampled geometries constitute the bottleneck of the procedure, since each one is used for a single point TD-DFT calculation. It is important, thus, to find a number of sampled geometries that constitute a compromise between reliability and computational cost.

Emission spectrum simulations using the nuclear ensemble method were then run for three of the molecules shown in Figure 2.1: biphenyl, naphthalene and bithiophene. Besides the number N of sampled geometries, we also analyzed the effect of functional choice and compared the results of Franck-Condon and nuclear ensemble spectra with experimental data. Our simulations were all performed at 0 K, with a broadening factor of 0.05 eV.

Results can be seen in Figures 2.3, 2.4 and 2.5. Three main conclusions can be drawn. First, when it comes to the number of sampled geometries, 500 is the amount that provides the best results. Simulations performed with 50 sampled geometries showed many peaks and are unable to reproduce correctly the general features of the experimental spectra. On the other hand, when 5000 geometries are sampled, the resulting spectrum becomes mostly broad and featureless as the peak structure disappears. In principle, more is always better when considering the number of sampled geometries used to simulate spectra in the nuclear ensemble method, as it employs an average over an ensemble to obtain approximated values of the overlap integrals. However, since the contributions from each geometry are broadened by a Gaussian or Lorentzian line shape, the addition of a very large number of them ends up blurring any peak structure that may be present.

The second conclusion refers to the fact that the nuclear ensemble simulations are more accurate than the Franck-Condon ones. They are able to better reproduce both the peak structure of
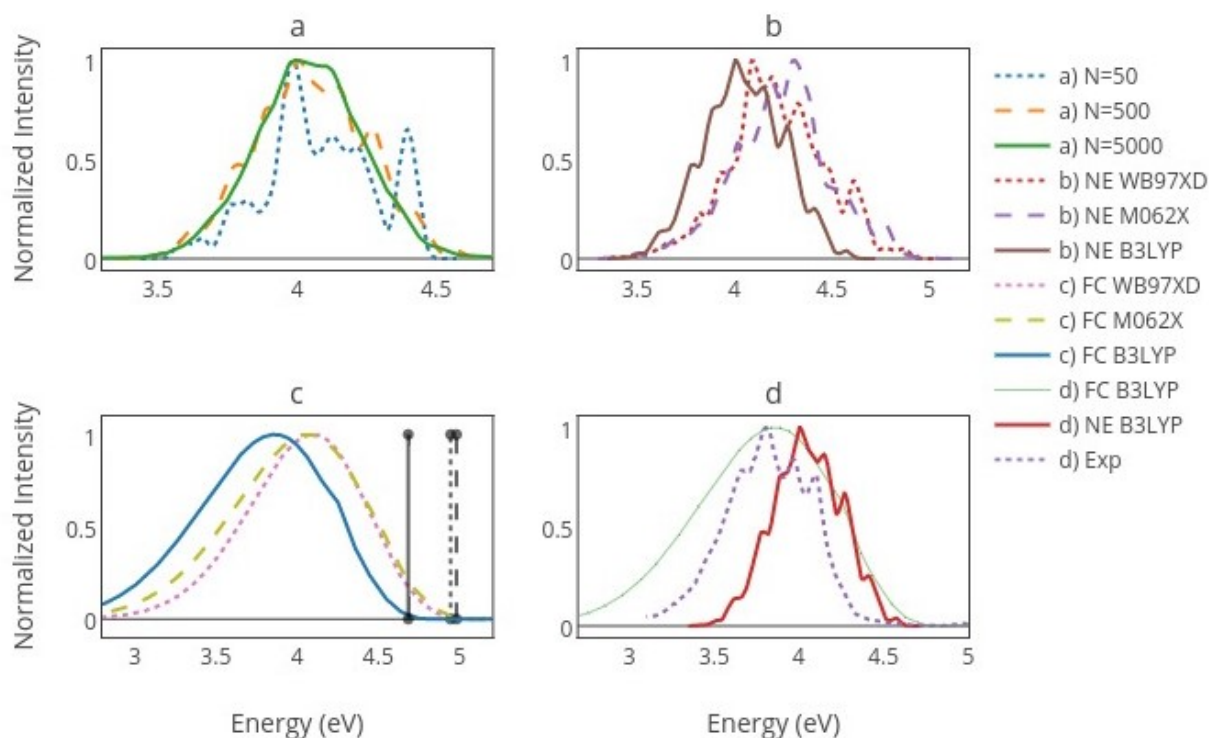
Figure 2.3: Biphenyl: a) Effect of the number of sampled geometries in nuclear ensemble simulations. b) Effect of functional choice to nuclear ensemble spectra. c) Effect of functional choice to Franck-Condon spectra. Vertical lines mark the 0-0 transition. d) Comparison between simulations and experimental data. Reproduced from reference [1].

the spectra and their energies. Only in the case of naphthalene, which is a rigid molecule, was the Franck-Condon simulation able to satisfactorily reproduce the structure of the experimental spectrum.

Finally, the third conclusion regards functional choice. We found that B3LYP actually produced better results, as the other functionals overestimated even more the transition energies for the molecules studied here.

In summary, the nuclear ensemble method proves a valuable tool for spectrum simulations, particularly in the case of flexible molecules. The analysis shown here was published along with a thorough derivation of the theoretical aspects behind the method[1] and the paper is presented in Chapter 6. In addition, the methods employed here were also used to investigate the spectra of acene-thiophene derivatives[15] in a study that is also presented in Chapter 6. Finally, a paper on the electronic properties of carotenoid molecules was also published in which I contributed with spectrum simulations[16].

Back to P6P and 6T

Once I was done with testing the methodology, I went back to the two molecules that got us started in the first place: P6P and 6T. Optimization of these molecular geometries proved tricky both in S_0 and S_1, as normal mode analyses frequently presented imaginary frequencies,
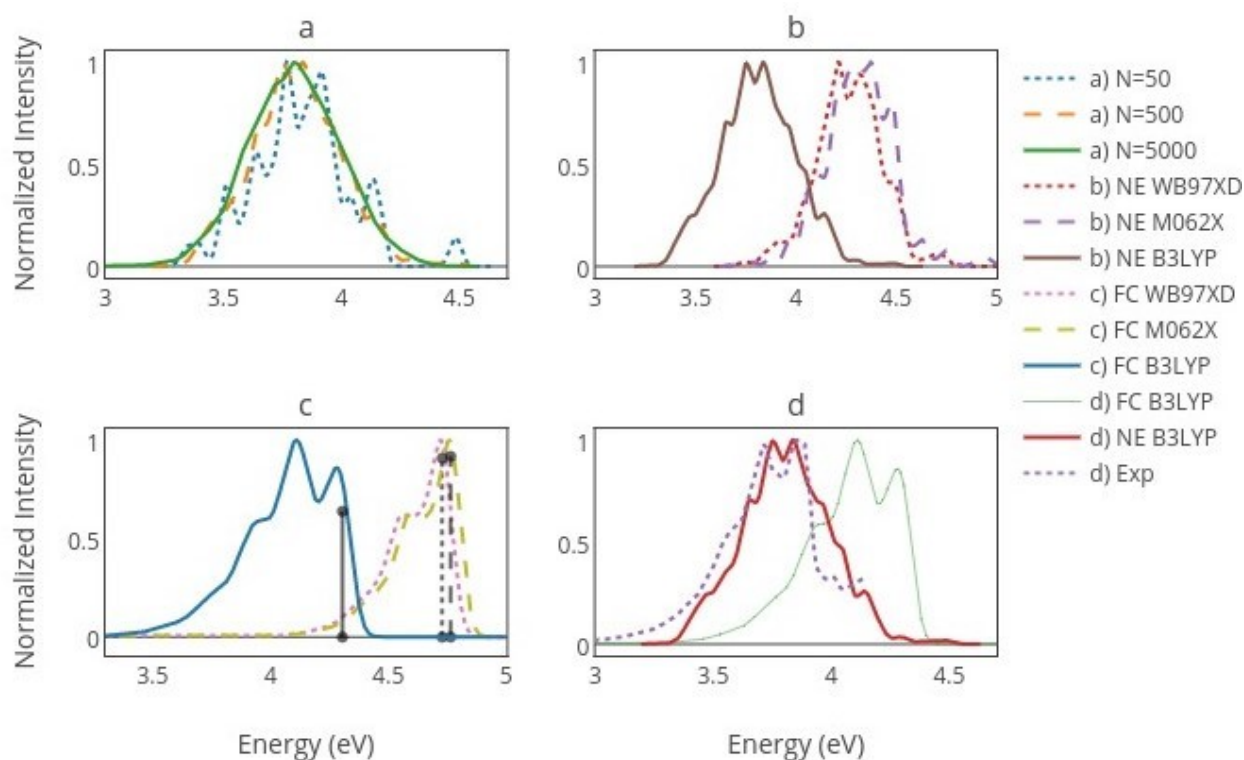
Figure 2.4: Naphthalene: a) Effect of the number of sampled geometries in nuclear ensemble simulations. b) Effect of functional choice to nuclear ensemble spectra. c) Effect of functional choice to Franck-Condon spectra. Vertical lines mark the 0-0 transition. d) Comparison between simulations and experimental data. Reproduced from reference [1].
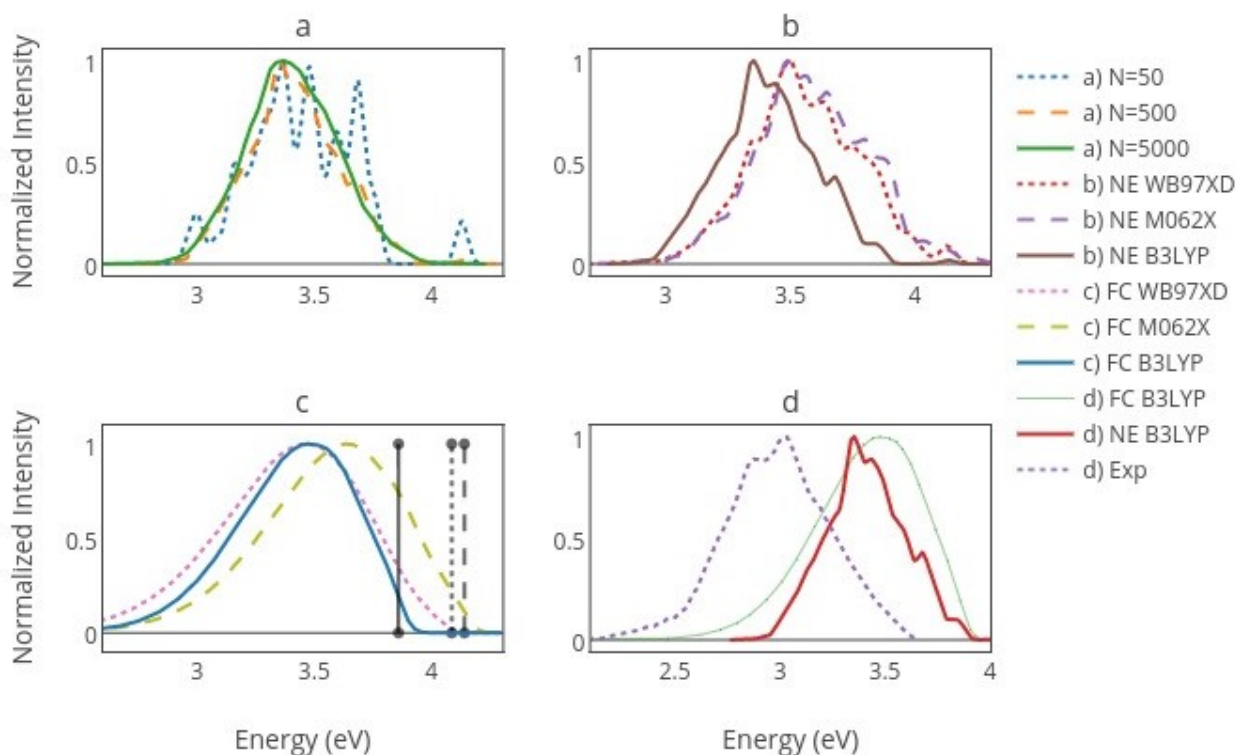
Figure 2.5: Bithiophene: a) Effect of the number of sampled geometries in nuclear ensemble simulations. b) Effect of functional choice to nuclear ensemble spectra. c) Effect of functional choice to Franck-Condon spectra. Vertical lines mark the 0-0 transition. d) Comparison between simulations and experimental data. Reproduced from [1].

indicating that the optimized geometry did not, in fact, correspond to a minimum of the potential energy surface.

Eventually, the simulated absorption and emission spectra of the two molecules were finalized. Unfortunately, by the time they were done the paper on the device built with these molecules in Denmark had long been published. I was left then with four spectra which I had hopes that could be put to some use. How exactly was still unclear.

Appendix: Derivation of the Nuclear Ensemble Method

The starting point of the derivations are the expressions for spontaneous emission rate and absorption cross section obtained from quantum mechanics by means of time dependent perturbation theory. We first study the case of spontaneous emission.

Spontaneous Emission

The spontaneous emission rate is

$$\sigma_{em} = \frac{4\omega^3}{3c^3\hbar} \sum_{i,m,f,n} P_{im}(T) \left|\langle\phi_{fn}\left|M_{fi}\right|\phi_{im}\rangle\right|^2 \delta(E_{fn} - E_{im} + \hbar\omega). \tag{2.11}$$

The indices i and f refer to the initial and final electronic states whereas m and n refer respectively to the initial and final vibrational states. $P_{im}(T)$ is the Boltzmann distribution at temperature T, M_{fi} is the electronic dipole operator, ω is the angular frequency, c is the speed of light and δ is the Dirac delta function.

Writing the Dirac delta function in its Fourier representation yields

$$\sigma_{em} = \frac{2\omega^3}{3\pi c^3\hbar^2} \int \sum_{i,m,f,n} P_{im}(T) \left|\langle\phi_{fn}\left|M_{fi}\right|\phi_{im}\rangle\right|^2$$
$$\times \exp\left[\frac{i}{\hbar}(E_{fn} - E_{im} + \hbar\omega)t\right] \mathrm{d}t. \tag{2.12}$$

We may write the squared term as the product of the expectation value of M_{fi} and its complex conjugate and write part of the exponential in operator form as follows

$$\sigma_{em} = \frac{2\omega^3}{3\pi c^3 \hbar^2} \int \sum_{i,m,f,n} P_{im}(T) \langle \phi_{im} | M_{fi} | \phi_{fn} \rangle \langle \phi_{fn} | e^{H_f t/\hbar} M_{fi} e^{-H_i t/\hbar} | \phi_{im} \rangle$$

$$\times \exp[i\omega t] \, dt, \tag{2.13}$$

with H_f and H_i denoting the final and initial vibrational Hamiltonian, that is, the vibrational Hamiltonian for a given initial and final electronic configuration.

Defining [17]

$$M_{if}(t) = e^{H_f t/\hbar} M_{fi} e^{-H_i t/\hbar}, \tag{2.14}$$

and performing the summation on n by taking advantage of the closure condition, yields

$$\sigma_{em} = \frac{2\omega^3}{3\pi c^3 \hbar^2} \int \sum_{i,m,f} P_{im}(T) \langle \phi_{im} | M_{fi} M_{fi}(t) | \phi_{fn} \rangle$$

$$\times \exp[i\omega t] \, dt. \tag{2.15}$$

We now resort to the semi-classical time-dependent dipole moment approximation [18], which treats the nuclei as fixed, restricting the time dependence of the dipole moment to

$$M_{fi}(t) = M_{fi} \exp\left[i\omega_{fi}(\vec{R})t\right], \tag{2.16}$$

with

$$\omega_{fi}(\vec{R}) = \frac{1}{\hbar}[\varepsilon_f(\vec{R}) - \varepsilon_i(\vec{R})]. \tag{2.17}$$

The term in brackets in the last equation is the so-called vertical excitation energy.

Plugging this approximation in our expression for the emission rate and abandoning the Dirac notation, we obtain

$$\sigma_{em} = \frac{2\omega^3}{3\pi c^3 \hbar^2} \int \sum_{i,m,f} P_{im}(T) |\phi_{im}(\vec{R})|^2 M_{fi}^2(\vec{R})$$

$$\times \exp\left[\frac{i}{\hbar}(\hbar\omega_{fi}(\vec{R}) + \hbar\omega)t\right] dt \, d\vec{R}. \tag{2.18}$$

Now we define $\Delta E_{fi} = \hbar\omega_{fi}$. Since we are analyzing an emission process, $\Delta E_{fi} < 0$, so we

may write $\Delta E_{if} = -\Delta E_{fi} = -\hbar\omega_{fi}$. By making this substitution and integrating with respect to t, we recover the delta function,

$$\sigma_{em} = \frac{4\omega^3}{3c^3\hbar} \int \sum_{i,m,f} P_{im}(T)|\phi_{im}(\vec{R})|^2 M_{fi}^2(\vec{R})\delta(\hbar\omega - \Delta E_{if}(\vec{R}))\,\mathrm{d}\vec{R}. \tag{2.19}$$

Because of the delta function, we may insert the ω^3 factor in the integral as $\Delta E_{if}^3(\vec{R})/\hbar^3$. We may also change the sign of the argument of the delta function, yielding

$$\sigma_{em} = \frac{4\omega^3}{3c^3\hbar^4} \int \sum_{i,m,f} P_{im}(T)|\phi_{im}(\vec{R})|^2 \Delta E_{if}^3(\vec{R}) M_{fi}^2(\vec{R})$$
$$\times\,\delta(\Delta E_{if}(\vec{R}_j) - \hbar\omega)\,\mathrm{d}\vec{R}. \tag{2.20}$$

This result may be written in terms of oscillator strengths f_{fi}, which can be obtained with the aid of electronic structure software. Oscillator strengths are related to the dipole moment as [19]

$$M_{fi}^2 = \frac{3\hbar^2 e^2}{2m\Delta E_{if}} f_{fi}, \tag{2.21}$$

where e and m are the charge and mass of the electron. So the emission rate reads

$$\sigma_{em} = \frac{2e^2}{mc^3\hbar^2} \int \sum_{i,m,f} P_{im}(T)|\phi_{im}(\vec{R})|^2 \Delta E_{if}^2(\vec{R}) f_{fi}(\vec{R})$$
$$\times\,\delta(\Delta E_{if}(\vec{R}_j) - \hbar\omega)\,\mathrm{d}\vec{R}. \tag{2.22}$$

Now, to account for the broadening of the spectral lines, we replace the delta function with a normalized Gaussian or Lorentzian function, denoted by G, with a broadening factor δ, resulting in

$$\sigma_{em} = \frac{2e^2}{mc^3\hbar^2} \int \sum_{i,m,f} P_{im}(T)|\phi_{im}(\vec{R})|^2 \Delta E_{if}^2(\vec{R}) f_{fi}(\vec{R})$$
$$\times\,G(\Delta E_{if}(\vec{R}_j) - \hbar\omega, \delta)\,\mathrm{d}\vec{R}. \tag{2.23}$$

Restricting the calculation for emissions from the first electronic excited state ($i = 1$) to the electronic ground state ($f = 0$), we obtain

$$\sigma_{em} = \frac{2e^2}{mc^3\hbar^2} \int \sum_m P_{1m}(T)|\phi_{1m}(\vec{R})|^2 \Delta E_{10}^2(\vec{R}) f_{01}(\vec{R})$$

$$\times G(\Delta E_{10}(\vec{R_j}) - \hbar\omega, \delta) \, \mathrm{d}\vec{R}. \tag{2.24}$$

This last expression may be interpreted as the average value of $\Delta E_{10}^2 f_{01} G$ with probability density given by $\sum_m P_{1m}(T)|\phi_{1m}(\vec{R})|^2$. To perform this calculation, we may resort to an average over an ensemble, as the Newton-X software does. Thus,

$$\sigma_{em} = \frac{2e^2}{mc^3\hbar^2} \left[\frac{1}{N} \sum_{j=1}^{N} \Delta E_{10}^2(\vec{R_j}) f_{01}(\vec{R_j}) G(\Delta E_{10}(\vec{R_j}) - \hbar\omega, \delta) \right], \tag{2.25}$$

with N random $\vec{R_j}$ points sampled from the $\sum_m P_{1m}(T)|\phi_{1m}(\vec{R})|^2$ distribution, which, since we are working in the harmonic approximation, is the probability density for a set of harmonic oscillators at temperature T [20]

$$\sum_m P_{1m}(T)|\phi_{1m}(\vec{R})|^2 = \prod_{j=1}^{3n-6} \sqrt{\frac{m_j\omega_j}{2\pi\hbar \sinh\left(\frac{\hbar\omega_j}{kT}\right)}}$$

$$\times \exp\left[-\frac{m_j\omega_j}{\hbar} x_j^2 \tanh\left(\frac{\hbar\omega_j}{2kT}\right) \right]. \tag{2.26}$$

The product extends to all normal modes of the molecule in the first electronic excited state, with k being the Boltzmann constant and x_j the normal coordinates, which can be converted back to cartesian coordinates in order to evaluate the emission rate.

This concludes the analysis of the nuclear ensemble method applied to spontaneous emission. Now we turn to the case of absorption.

Absorption

The expression for the absorption cross section is very similar to the one for spontaneous emission [10].

$$\sigma_{abs} = \frac{4\pi^2\omega}{3c} \sum_{i,m,f,n} P_{im}(T) |\langle \phi_{fn} |M_{fi}| \phi_{im}\rangle|^2 \delta(E_{fn} - E_{im} + \hbar\omega) \tag{2.27}$$

Following the same procedure done in the last section, we obtain an expression similar to

Equation 2.23

$$\sigma_{abs} = \frac{4\pi^2}{3c\hbar} \int \sum_{i,m,f} |P_{im}(T)\phi_{im}(\vec{R})|^2 \Delta E_{if}(\vec{R}) f_{fi}(\vec{R})$$

$$\times\, G(\Delta E_{fi} - \hbar\omega, \delta)\, \mathrm{d}\vec{R}. \tag{2.28}$$

Restricting the calculation to absorption from the ground electronic state ($i = 0$), yields

$$\sigma_{abs} = \frac{4\pi^2}{3c\hbar} \int \sum_{f,m} P_{0m(T)} |\phi_{0m}(\vec{R})|^2 \Delta E_{0f}(\vec{R}) f_{f0}(\vec{R})$$

$$\times\, G(\Delta E_{f0} - \hbar\omega, \delta)\, \mathrm{d}\vec{R}. \tag{2.29}$$

Again, this expression may be evaluated as an ensemble average as follows

$$\sigma_{abs} = \frac{4\pi^2}{3c\hbar} \sum_{f} \left[\frac{1}{N} \sum_{j=1}^{N} \Delta E_{0f}(\vec{R_j}) f_{f0}(\vec{R_j}) G(\Delta E_{f0} - \hbar\omega, \delta) \right], \tag{2.30}$$

with the $\vec{R_j}$ points sampled from the $\sum_m P_{0m} |\phi_{00}|^2$ distribution, that is, expression 2.26, now applied for the electronic ground state.

A final remark must be made. For temperatures above zero, one must also account for the phenomenon of stimulated emission. To obtain the proper net absorption, it is necessary to multiply the absorption cross section by a factor γ ([18, 21])

$$\gamma = 1 - \exp\left(\frac{\hbar\omega}{kT}\right) \tag{2.31}$$

This concludes the derivation of the expressions used in the nuclear ensemble method.

CHAPTER 3

SIMULATING EXCITON DYNAMICS

Finding a Problem of My Own

Once I was done with the papers on spectrum simulations, I went back to the experiments performed in Denmark regarding exciton transport in P6P and 6T nanofibers[2]. The studied device is composed of 10 alternating layers of P6P and 6T nanofibers. The P6P layers were 160 Å thick, whereas the 6T ones were 4 Å thick. This device is then excited with a laser with an energy corresponding to the absorption band of the P6P nanofibers. The color of the emitted light is shown to change with temperature and this change is explained in terms of the migration of excitons from the P6P to the 6T nanofibers. This is done by performing time resolved photoluminescence (TRPL) spectra measurements. In this experimental setup, the amount of emitted light from a sample is measured as a function of time. Since P6P and 6T emit light in different regions of the spectrum, by registering photons emitted from only particular wavelengths it is possible to isolate the contributions from each material. The results of such experiment are shown in Figure 3.1. These experiments are especially relevant since they shed light on a key mechanism involved in the working of organic optoelectronic devices: singlet exciton diffusion.

In organic light emitting diodes (OLEDs) excitons are injected in the active layer and diffuse until recombination occurs[22]. In organic photovoltaic devices (OPVs), on the other hand, excitons generated after light absorption must diffuse through the material until they reach an electron donor-acceptor interface[23]. At this interface, excitons may dissociate into free charges, which must be collected to generate current.

Since excitons have a limited lifetime - they eventually recombine -, the capacity for an exciton to reach a donor-acceptor interface becomes an important limiting factor to the efficiency of devices[24]. Strategies to overcome this limitation can be of electronic or morphological nature. In terms of morphology, the development of bulk heterojunctions (BHJs) aimed at reducing the
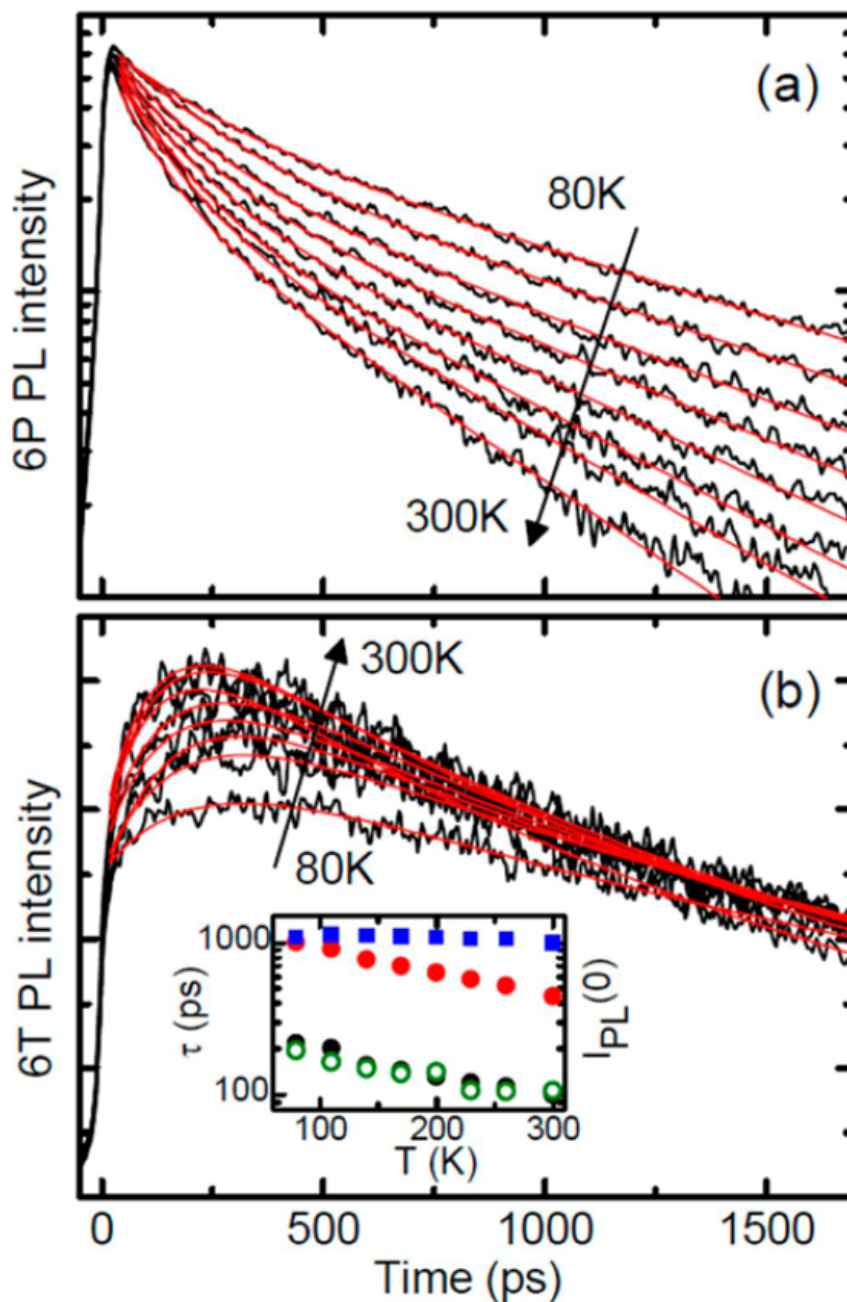
Figure 3.1: Experimental results from TRPL measurements on the P6P/6T device. a) Photons emitted from P6P. b) Photons emitted from 6T. As temperature increases, higher amounts of excitons migrate from the P6P to 6T layers. Reproduced from reference [2].

distances an exciton would need to travel in order to reach an interface, increasing the amount of separated charges[25, 26]. In terms of electronic structure, we must first understand in details the process responsible for diffusion of singlet excitons: the Förster resonance energy transfer.

Förster Energy Transfer for Singlet Excitons
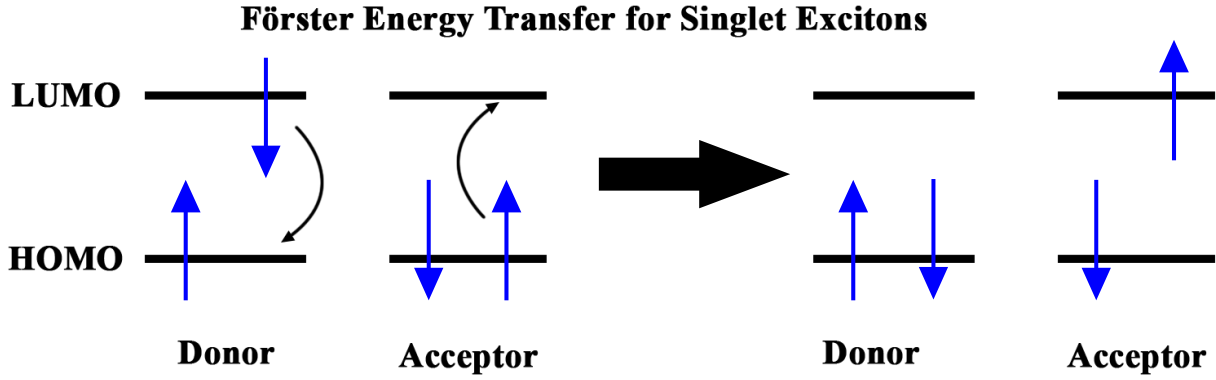
Figure 3.2: Schematics representing the Förster resonance energy transfer mechanism. Energy is transferred non-radiatively from an excited to a ground state molecule.

The Förster Mechanism

Singlet exciton diffusion occurs mainly due to the Förster resonance energy transfer[6]. This is a non-radiative process in which excitation energy is transferred from one molecule to the other as long as there is overlap between the emission and absorption spectra of the donor and acceptor molecules, respectively (see Figure 3.2). The Förster transfer rate is given by [9, 27]:

$$k_F(r) = \frac{9c^4\kappa^2}{8\pi r^6} \int_0^\infty \frac{d\omega}{\omega^4} I_D(\omega)\alpha_A(\omega), \tag{3.1}$$

where c is the speed of light, r is the intermolecular distance, $I_D(\omega)$ is the donor's differential emission rate and $\alpha_A(\omega)$ is the acceptor's absorption cross-section. The term κ is the so-called orientation factor, which takes into account the relative orientation between the transition dipole moments of the donor and acceptor molecules. It is given by[28]

$$\kappa = \hat{\mu}_D \cdot \hat{\mu}_A - 3(\hat{r} \cdot \hat{\mu}_D)(\hat{r} \cdot \hat{\mu}_A), \tag{3.2}$$

in which $\hat{r}$ is the normalized displacement vector between donor and acceptor and $\hat{\mu}_D$ and $\hat{\mu}_A$ are the normalized transition dipole moments of the donor and acceptor, respectively. This term, however, may be hard to obtain in applications. It is often the case that an average value that considers random orientations between molecules is considered, resulting in $\kappa^2 = 2/3$[28].

An important concept regarding the Förster mechanism is the Förster radius. It is defined as the distance for which the Förster transfer rate equals the emission rate. The radiative emission rate (k_{emi}) and lifetime (τ_{emi}) may be calculated from the emission spectrum as[6]

$$k_{emi} = \frac{1}{\tau_{emi}} = \int_0^\infty I_D(\omega)d\omega. \tag{3.3}$$

Equating expressions 3.1 and 3.3 and solving for the desired intermolecular distance results in

$$R_F^6 = \frac{9c^4\kappa^2\tau_{emi}}{8\pi} \int_0^\infty \frac{d\omega}{\omega^4} I_D(\omega)\alpha_A(\omega),$$ (3.4)

which allows us to write the expression for the Förster rate in a simpler fashion

$$k_F(r) = \frac{1}{\tau_{emi}} \left(\frac{R_F}{r}\right)^6.$$ (3.5)

Furthermore, when disconsidering other non-radiative pathways for excitons, the probability of Förster transfer may be calculated as

$$P(r) = \frac{k_F}{k_{emi} + k_F} = \frac{1}{1 + \left(\frac{r}{R_F}\right)^6}.$$ (3.6)

Putting the Spectra to Use

Equation 3.4 shows the Förster radius dependence on the overlap integral between absorption and emission spectra. When this overlap is non existent, the Förster radius becomes zero, which makes the transfer impossible.

In a multi layered morphology, such as the P6P/6T device, exciton transfer may take place between homodimers (P6P to P6P or 6T to 6T) or heterodimers (P6P to 6T or 6T to P6P). To analyze such possibilities, we plot the simulated spectra of all donor-acceptor pairings between P6P and 6T. These are shown in Figure 3.3. These spectra were simulated using the nuclear ensemble method with 500 sampled geometries and using the M062X functional along with the 6-31G(d,p) basis set. This figure shows that exciton diffusion in both homodimers is possible, as there is overlap between the absorption and emission spectra of both P6P and 6T. When it comes to the heterodimers, however, it can be seen that only the P6P to 6T Förster transfer is possible, since it presents a large overlap. The 6T to P6P transfer is, therefore, forbidden. This means that excitons that migrate from P6P to 6T layers become confined in the latter.

In addition to the qualitative analysis above, equation 3.4 further shows that the simulated absorption and emission spectra allow for the actual calculation of Förster radii. Employing equation 3.3 to calculate the radiative lifetime and assuming an average value for the orientational factor ($\kappa^2 = 2/3$), it is possible to obtain Förster radii completely from ab initio calculations. It is important to mention that radiative lifetimes are affected by the medium's refractive index. The exact dependence of an emission spectrum on refractive index has been subject of debate. It has been taken as proportional to n^3 in some studies[29, 13] or n^2 in others[30, 31]. Here, I take the n^2 dependence, as the n^3 one seems to underestimate radiative lifetimes considerably.

Using the spectra shown in Figure 3.3 to calculate Förster radii produces the following results: 32 Å for P6P homodimers, 40 Å for 6T homodimers, 52 Å for the P6P to 6T transfer and 0 for
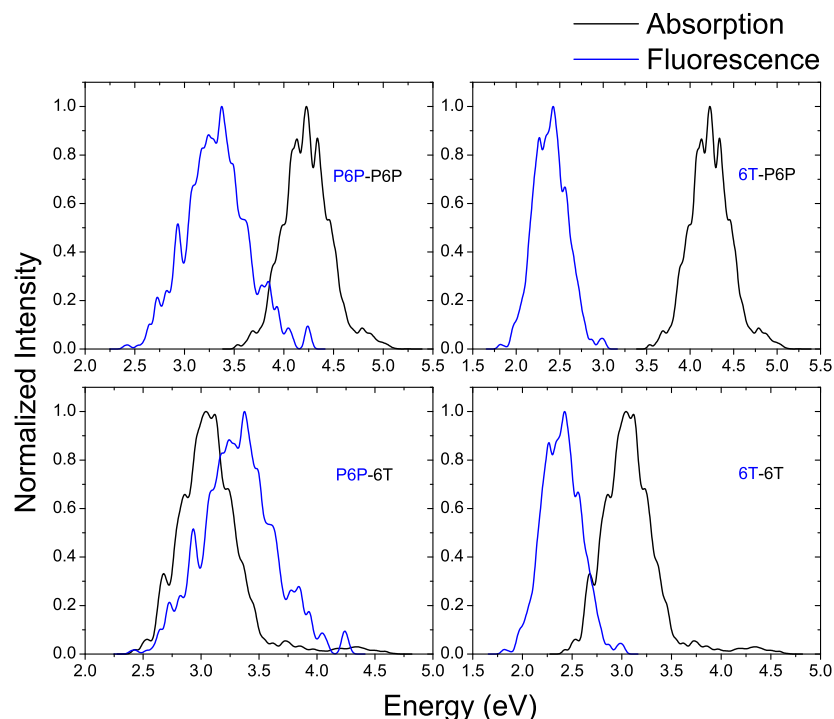
Figure 3.3: Absorption (black) and emission (blue) spectra for each donor-acceptor pairing of P6P and 6T. Only the P6P to 6T pairing does not allow for Förster transfer. Reproduced from reference [3].

the 6T to P6P one. These results indicate that exciton diffusion in 6T should be more efficient than in P6P, given its larger Förster radius. By the same token, exciton transfers from P6P to 6T should be even more efficient.

These calculations must be taken with a grain of salt, however, since they are performed under ideal conditions. Temperature effects, for instance, are not taken into account. On the other hand, they provide a clear picture of the possible transfers and their relative importance.

It would take me still quite some time to find good use for this technique of calculating Förster radii, but this capacity eventually made me notice that if I had some estimate of intermolecular distances, I could find actual numerical values for Förster rates and probabilities (equations 3.5 and 3.6). Having these numbers meant I could simulate the whole process. Now, that was an interesting idea.

A Kinetic Monte Carlo For Exciton Dynamics

On February 2017, I had the opportunity to visit the group of Professor Mathieu Linares at the Linköping University in Sweden. He and his then PhD Student Riccardo Volpi were working on a software with the goal of studying charge mobility in organic materials. The program, called Gorilla, combined molecular dynamics (MD), electronic structure calculations and a Kinetic Monte Carlo (KMC) algorithm to simulate charge transport.

The molecular dynamics simulation had the role of producing a realistic morphology that would take into consideration the interactions between molecules, thus including the effects of static disorder in the simulation. The morphology obtained in this fashion becomes then the background upon which the KMC algorithm is run. Details about the model behind their program had already been published in a work that investigated charge transport in C_{60}[32]. We extended the results by applying the model to charge transport in $PC_{61}BM$, which showed interesting differences with respect to C_{60}, particularly due to its lack of symmetry. Results were published[33] and the paper is presented in section 6.

This trip to Sweden was my first contact with the KMC method and would prove essential to everything I produced afterwards. The algorithm works as follows: an element - whether it be an electron, a hole or an exciton - is positioned at some site, representing one of the molecules. This element has several neighboring molecules to which it may hop. Let the rate of transfer to a given site, meaning the probability of transfer per unit time, be k_i. The probability of hopping to the site i is then given by

$$P_i = \frac{k_i}{\sum_i k_i},\tag{3.7}$$

where the sum is performed over all sites to which hopping is possible. The 0 to 1 interval is then divided as a sequence $a_n = \sum_{i=1}^{n} P_i$. Finally, a random number N_r from 0 to 1 is drawn and the nth neighbor is chosen if this random number is such that $a_n \leq N_r < a_{n+1}$. Once the hop is performed, the simulation time step is updated. This procedure is repeated until some stopping criterion, such as maximum simulation time, is met.

With these ideas in mind, I decided then to develop a Kinetic Monte Carlo code and apply it to the problem of exciton diffusion. In particular, I could take advantage of the available experimental results and attempt to simulate the process.

The work starts at morphology, since it is a key aspect in the experiments. To reproduce this morphology, meaning 10 alternating layers of P6P and 6T, a matrix is created whose first column corresponds to a 6T monolayer followed by a number L of columns representing the number of P6P monolayers that compose the actual P6P layer (Figure 3.4). This arrangement is repeated 10 times and the number of lines in this matrix is set arbitrarily to 100, leading to a $100 \times 10(L+1)$ matrix. Each cell in the matrix is then identified as either P6P or 6T.

Then, excitons are inserted in random positions corresponding to the P6P layers, simulating light absorption by this material. Once the excitons are generated, a simulation round starts. For each exciton, a two-step process defines whether it hops to a nearby cell, stays put or recombines. In the first step, the program decides randomly with which of 9 cells the Förster transfer is going to be attempted. These 9 cells are the 8 first neighbors of the exciton in question plus the very cell where the exciton stands.

To decide which neighbor cell is chosen, the algorithm presented above is employed. Transfer rates to all neighbors are calculated (Equation 3.5) and the probabilities are taken as the ratio between each rate and the sum of all rates. A random number is then generated and a cell is selected
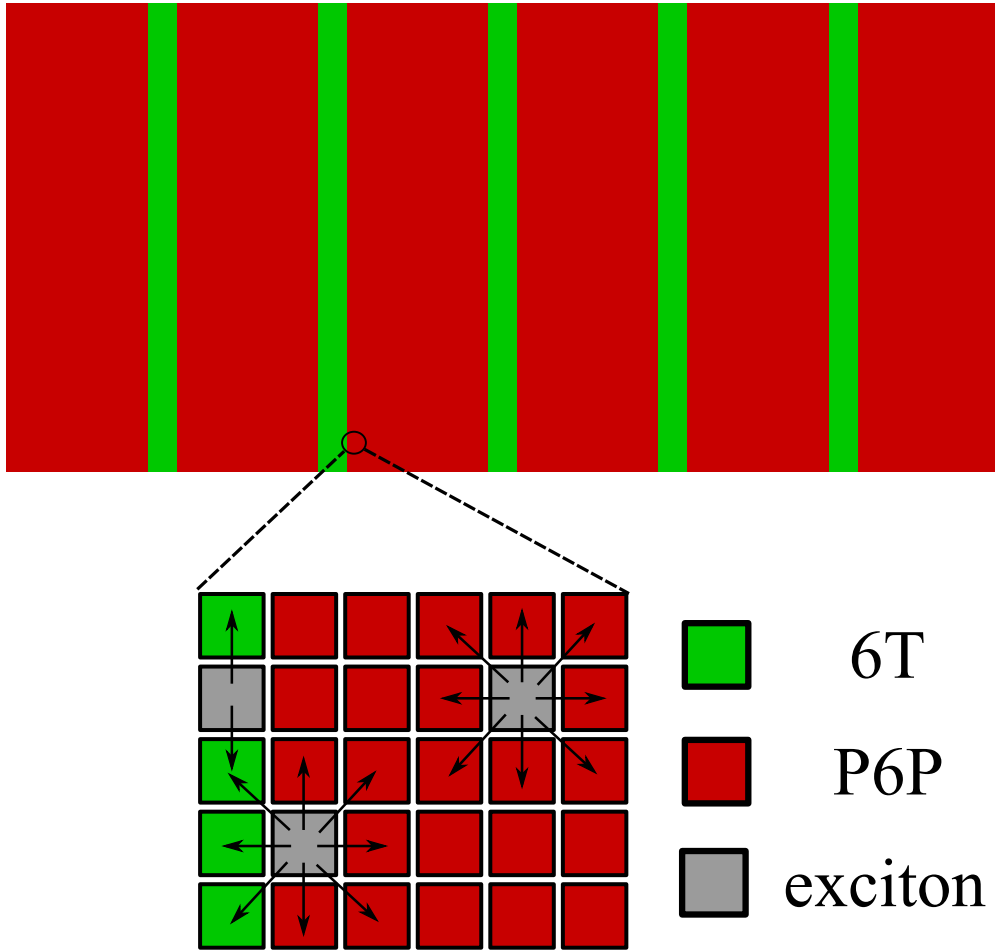
Figure 3.4: Schematics of the morphology of the multilayered P6P-6T system. In detail, the cells corresponding to each site that stands for the P6P or 6T portions of the system. The arrows show the possible hopping directions for excitons in each material. Reproduced from reference [3].

for the attempted Förster transfer. Next, to decide whether the transfer succeeds or recombination occurs, a second random number is generated and compared to the probability given by Equation 3.6. This procedure is repeated for every exciton in the simulation after which the time step is increased by one unit.

The time it takes for an exciton to hop may be taken as the inverse of its Förster rate ($t_{hop} = 1/k_F$). Since the transfer rates k_F are different for each pair of materials, meaning that the Förster radius for each kind of dimer is different, two measures are necessary. First, the time step unit of the simulation is taken as the inverse of the largest Förster rate selected in a given round ($t_{step} = min(t_{hop})$). Second, at each time step, the excitons are tested for hopping only if a randomly generated number from 0 to 1 is less or equal to the ratio t_{step}/t_{hop} where t_{hop} is the time it takes for hopping in the material where the exciton is. This ensures the consistency between exciton speeds in both materials.

As shown above, calculations indicate that the Förster radius from P6P to 6T is much larger than for the other possible cases. This means that the Förster rate in this case is much larger, and thus, the hopping time for this transfer is much shorter than for the other two. So, for simplicity, the P6P to 6T transfer probability was set to 100% and was considered to take as long as the time

step of the simulation. This approximation holds because of the layered morphology, in which the amount of P6P to 6T transfers is much lower than the number of transfers between homodimers.

To simulate the TRPL experiments, the time and the material at which recombination occurs are registered. The simulation round ends either after all excitons have recombined or after the maximum time step has been reached. To improve the reliability of the results, this process is repeated several times and the results are added over.

Notice that to calculate both the Förster rate and the transfer probability it is necessary to use values for the intermolecular distance to Förster radius ratio in P6P (P6P d/R_F) and in 6T (6T d/R_F) as input in the model. The number of P6P monolayers L is also required as input. The question then becomes how to find the values for these parameters in order to reproduce experimental results?

Fortunately, Professor Jakob Kjelstrup-Hansen, from the University of Southern Denmark, provided us with the raw data from the TRPL measurements for 8 different temperatures. However, the large number of configurations resulting from the many combinations of input parameters meant that a simple survey over the configuration space was impracticable. We needed a smarter method.

The Genetic Algorithm

The problem we were facing was an optimization problem. We needed to search the configuration space looking for a set of parameters that produced the most realistic simulations. A method that had been used before as an optimization procedure in applications regarding molecular physics and physical chemistry was the so-called genetic algorithm[34, 35, 36, 37, 38]. This method consists of an automated search for optimal parameters that is particularly useful in the case of complex configuration spaces. We decided to give it a go.

In the genetic algorithm, the model parameters correspond to the genes. The process starts by randomly selecting N sets of genes. These sets of genes are used to run N simulations. Once these simulations are done, they are evaluated by a fitness function, which measures their quality. The function is designed in such a way that the lower the results it yields, the higher the quality of the simulation. In our context, quality refers to how close a simulation reproduces experimental results. These results are then ordered from lowest to highest fitness and the first S individuals are considered to be survivors. From the genes of these survivors a next generation of individuals is born.

Each individual in the following generation is chosen in two steps. First, two survivors are selected randomly as progenitors. The higher the quality of a simulation - that is, the lower its fitness function value -, the higher the probability of a certain individual being chosen as a progenitor. After that, new genes are also selected randomly. To do so, a gene value is sampled from a gaussian distribution with mean given by the average between the corresponding genes from the

progenitors and with a standard deviation that is inserted by hand. The standard deviation of the distribution plays the role of mutations and is a number that has to be chosen with care. If it is too high, it may result in practically no correlation between progenitors and offspring, which amounts to producing a random search of the configuration space. On the other hand, a very low standard deviation makes the process too dependent on the initial sampling, which may prevent the algorithm from exploring certain areas in the configuration space. Furthermore, the standard deviation has to be set having in mind the order of magnitude of the parameter in question. To address all these issues, we set instead the coefficient of variation (the ratio of the standard deviation to the mean) as 0.05. As such, the standard deviation for each gene is adjusted by its mean value.

To implement this optimization procedure, all that was left was figuring out how to measure the fitness of each simulation. As mentioned earlier, the quality of a simulation is linked to how well it reproduces experimental results. Therefore, the fitness function should return a number that measures how close it resembles the experimental data.

In the original study, the experimental TRPL spectra had been fitted with biexponential functions, which allowed for the identification of characteristic times. We then attempted fitting the simulated TRPL spectra also with biexponential functions and comparing the characteristic times with the experimental ones. This did not work at all. The fittings were often inconsistent and needed different initial guesses to actually produce decent results. From the point of view of a process that was supposed to be automated, this shortcoming was fatal.

To overcome this issue, we resorted to calculating the root mean squared deviation between the simulated and experimental curves. We also add the root mean squared deviation between the derivative of the simulated and experimental curves to improve the scheme further. To do so, the TRPL curves for P6P and 6T were normalized by the sum of their areas. This procedure amounts to equating the number of excitons that recombine in both the experiment and simulation, while keeping the correct proportion of photon emission from the two materials. Since the TRPL curves - both experimental and simulated - were very much jagged, we applied a Savitzky-Golay filter [39] to smooth the data. The sum of these two root mean squared deviations then constitutes our fitness function, which the genetic algorithm searches to minimize.

The algorithm was run comparing simulations with experimental data obtained from eight temperatures ranging from 80 K to 300 K. A number of 10 individuals was set as first generation. These were created using d/R_F ratios and a number of P6P monolayers randomly selected from a 0.2 to 1.2 and a 10 to 40 intervals, respectively. The following generations of 10 individuals derived from crossings between the five best simulations found thus far. A total of 40 generations was produced. Each simulation employed $100,000$ excitons for producing its TRPL curves.
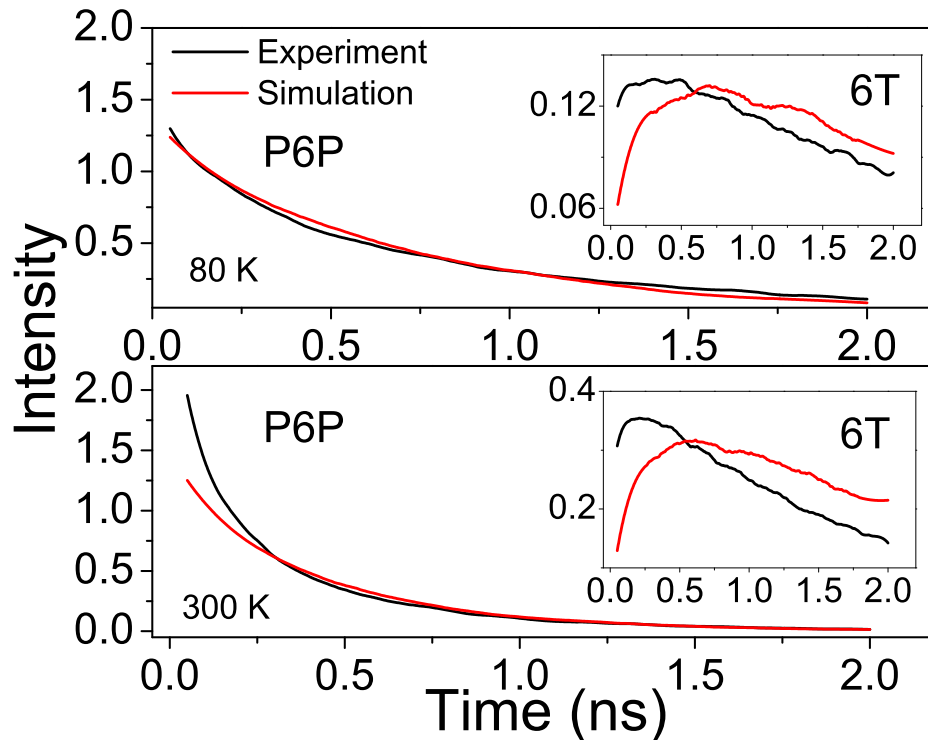
Figure 3.5: Comparison between simulated and experimental TRPL spectra of P6P and 6T at 80 K and 300 K. For both temperatures, poor agreement is found. Reproduced from reference [4].

Frustrating Results

After countless hours of running the genetic algorithm in the attempt to reproduce the TRPL curves for eight temperatures, results were less than inspiring. Figure 3.5 shows the comparison between simulated and experimental TRPL spectra of P6P and 6T for two temperatures, 80 K and 300 K. The simulated spectra shown in this figure correspond to the best simulations found by the genetic algorithm. It is clear, however, that there is poor agreement between simulations and experiment.

Some features of these results are noteworthy, though. First of all, it can be seen that the simulations performed at 80 K manage to reproduce quite well the experimental P6P curve, but as temperature increases this agreement disappears. In particular, the initial behavior of the experimental P6P curve is not observed in the higher temperature cases. The 6T curves, on the other hand, are systematically undervalued, with simulations being unable to match the increase in intensity observed in the first 0.5 ns.

These results allowed for some conclusions, though. It was clear that whatever the cause for the poor agreement, it resided in the initial moments of the simulation, when exciton concentrations are larger. Furthermore, the quality of the simulations decreased with temperature, which correlates with higher amounts of exciton migration. These observations suggest that the source of the poor agreement between simulation and experiment is the neglect of some kind of exciton-exciton interaction.

Exciton-Exciton Interactions
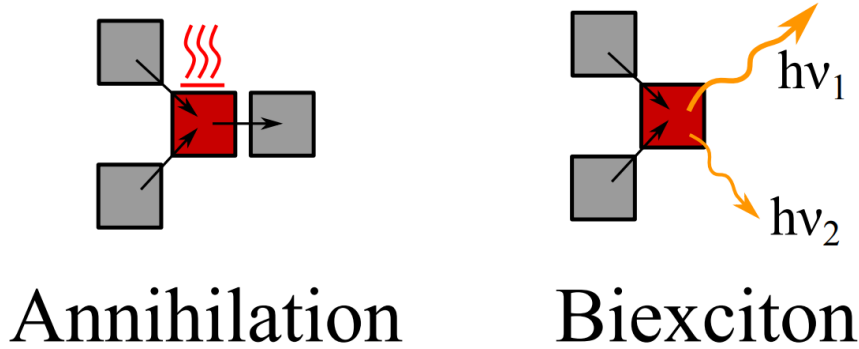
Figure 3.6: Schematics of the two mechanisms of exciton-exciton interactions considered here.

When it comes to exciton-exciton interactions, the phenomenon that is most often cited is the exciton-exciton annihilation[28, 40]. In this process, two excitons (S_1) that find each other produce a higher excited state (S_n) which, in turn, returns non-radiatively to the excited state (S_1). In other words, the interaction between two excitons results in the non-radiative annihilation of one of them (Figure 3.6-Left).

By looking at the experimental results, it can be seen that this should not be the effect responsible for the mismatch between experiment and simulation because of its non-radiative nature. It would not contribute to the faster rise in photoluminescence intensity observed in the 6T portions of the system.

A second bimolecular phenomenon involving excitons is the biexciton cascade emission[41, 42]. In this process, after the excitons meet, a biexciton is generated with an energy given by twice the exciton energy minus its binding energy. The cascade then takes place in a two-step process: a first photon is emitted corresponding to the deexcitation of the biexciton. This photon then stimulates the emission of a second one, with an energy corresponding to the excited state of the molecule (Figure 3.6-Right). In addition to this cascade emission, a non-radiative mechanism for biexciton recombination has also been reported. In this process, the biexciton's energy is transferred to electrons or holes in a kinetic form instead of resulting in radiative recombination[43, 44].

If the cascade emission effect is able to overcome its non-radiative competitor, the inclusion of biexcitons in the simulation could indeed anticipate the rise of the photoluminescence intensity in 6T and, concurrently, make the PL intensity decay faster in P6P. This is particularly so because the biexciton lifetime is much shorter than that of the excitons. In other words, the presence of biexcitons had the potential to increase the agreement between simulations and experiment.

To include these effects in the simulations, excitons that hop to the same site form biexcitons and recombine promptly, either radiatively or non-radiatively. To decide which form of recombination takes place, a probability of cascade emission in 6T (P_{XX}) is included as a parameter to the simulation. We restrict the use of this parameter to the 6T layers because, since excitons become

confined in this material and the 6T layers are very thin (4 Å), exciton concentrations are bound to get large there and bimolecular processes should become more relevant. Finally, the inclusion of exciton-exciton interactions in the simulations requires the addition of another parameter: the initial exciton concentration in the system (ρ_{ex}).

With these modifications made, a new round of calculations using the genetic algorithm had to be run. The new parameter P_{XX} had initial values randomly selected from a 0.01 to 0.9 interval. In the case of ρ_{ex}, this interval was set to range from 0.001 exciton per P6P site to 0.01 exciton per P6P site.

Enter the Biexciton
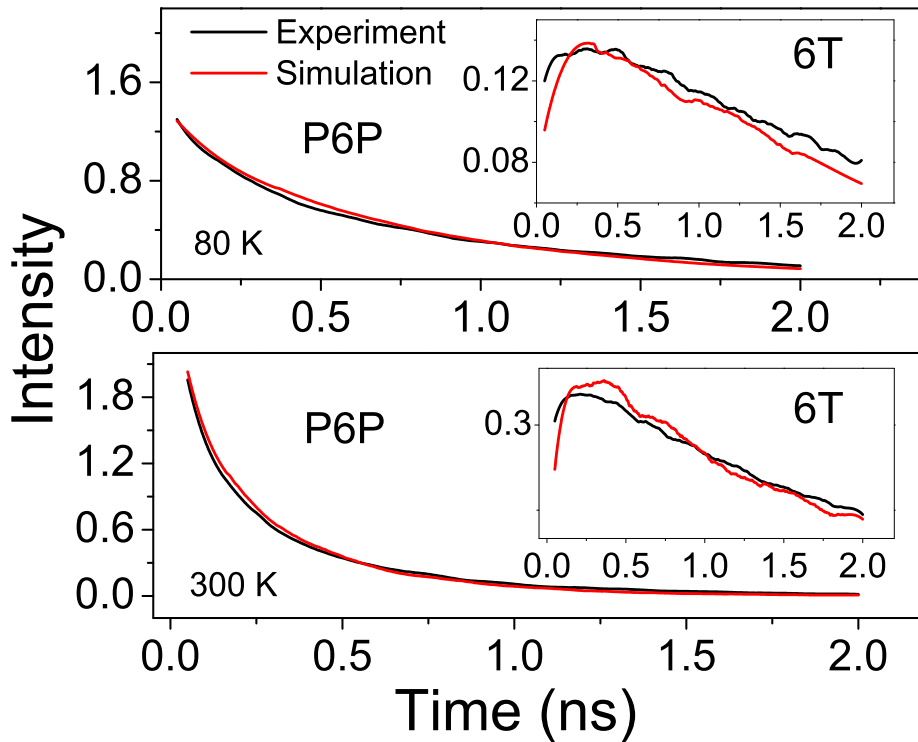
Figure 3.7: Comparison between simulated and experimental TRPL curves for two temperatures including the biexciton cascade emission. Much better now. Reproduced from reference [4].

Figure 3.7 shows the comparison between experiment and the best simulations found by the genetic algorithm, now including biexciton cascade emissions. The agreement is now remarkably better. The P6P curves are correctly reproduced both at the initial and latter times. The same can be said about the 6T curves, which show a faster rise in intensity, followed by an appropriate description of the PL decay. In addition, the simulations now present agreement with experiment in the whole temperature range.

The original experimental paper did not consider the role of bimolecular phenomena in explaining its results. In light of this perceived gap, our results were published[4] and the paper is

presented in section 6.

What Does the Genetic Algorithm Tell About the System?

Once the correct physical picture was employed, we could look at the parameters obtained by the genetic algorithm for each temperature. Figure 3.8 shows these results. The first parameter is the number of monolayers that constitute the P6P layers. Since the P6P layers are approximately 160 Å thick, the ratio between this thickness and the number of monolayers allows us to estimate the distance between P6P sites. Results indicate this distance to be around 10 Å (Figure 3.8-Top, blue points), which means that a number of 16 or 17 monolayers is needed to represent the P6P portions of the system. It is interesting to note that this value remains practically unchanged in the temperature range considered. This is expected, but the fact that such consistency was found with the genetic algorithm being run independently for each temperature speaks to the reliability of the method.
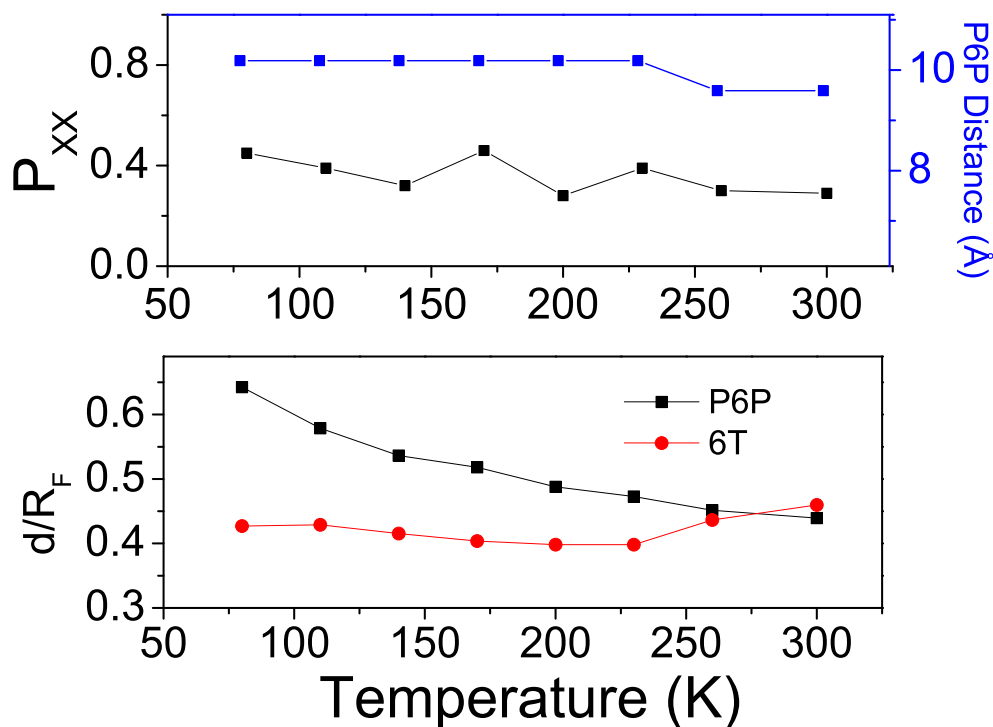
Figure 3.8: Model parameters obtained by the genetic algorithm for all temperatures considered. Top: intermolecular distances in P6P (blue) and probability of biexciton cascade emission (black). Bottom: ratio between intermolecular distance and Förster radius in P6P (black) and 6T (red). Reproduced from reference [3].

The second parameter is the probability of biexciton cascade emission once excitons hop to the same site. Results show a little more fluctuation, but remain around 0.4 in the whole temperature range, revealing that this process is temperature insensitive and that most of the exciton-exciton interactions result in non-radiative annihilation, rather than in cascade emission. Furthermore, exciton concentrations were found to be around 0.007 exciton per P6P site in the simulations.

The temperature dependence of the d/R_F ratio in P6P and 6T are shown in Figure 3.8-Bottom. This ratio measures the efficiency with which Förster transfers take place in each material. It can be seen that P6P presents a strong temperature dependence, with Förster transfers becoming more efficient as temperature increases. In 6T, on the other hand, the efficiency of the Förster process is practically temperature independent. This is in line with experiments that have demonstrated exciton diffusion in 6T to be temperature independent[45].
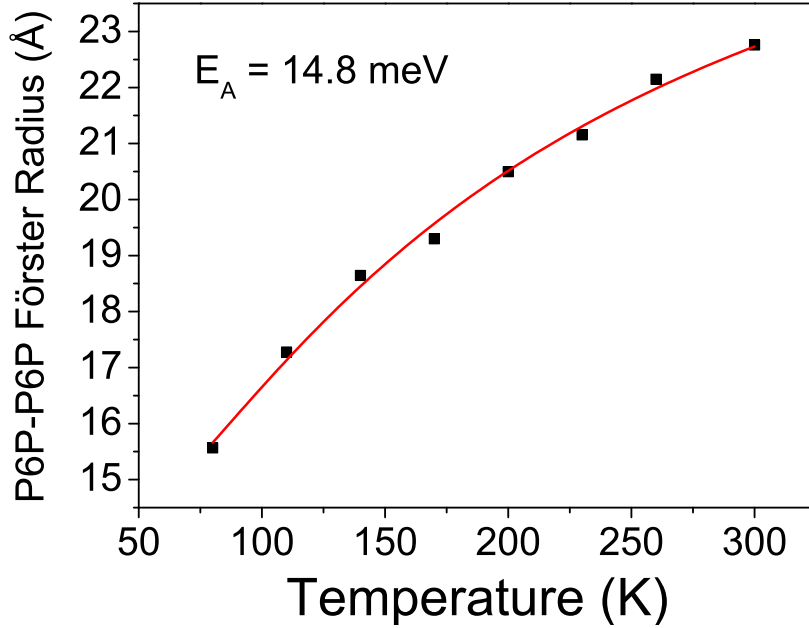
Figure 3.9: Temperature dependence of the Förster radius for exciton transfers in P6P. Line shows an exponential fit of the data with an activation energy of 14.8 meV. Reproduced from reference [3].

Combining the estimates of intermolecular distances in P6P with its d/R_F ratio, we obtain the actual values of the Förster radius for transfers in P6P. Its temperature dependence can be modeled by

$$R_F(T) = R_0 + R_1 \exp\left(-\frac{E_A}{kT}\right), \tag{3.8}$$

with $R_0 = 13.8$ Å, $R_1 = 15.8$ Å and $E_A = 14.8$ meV. The constant R_0 is the Förster radius at 0 K, and $R_0 + R_1$ the radius in the limit of infinite temperature. We attribute to the constant E_A the role of an activation energy for Förster transfers in P6P. The value found for this activation energy was 14.8 meV, which is close to the experimentally obtained value of 19 meV[2]. This behavior of Förster radius with temperature may be interpreted as including two effects: an initial downhill exciton migration that is independent of temperature associated with a temperature activated behavior that is dominant for higher temperatures. Such behavior has been observed in polymers, for instance[46].

The Usefulness of the Method

All the results shown above demonstrate that the combination of Kinetic Monte Carlo simulations with a genetic algorithm constitutes a powerful tool for the analysis of experimental data. At the same time, we are able to paint the entire physical picture and to understand the temperature dependence of the system under study by mapping a microscopic model of exciton dynamics to its experimental consequences.

It is quite clear that the same methodology may be applied to a vast array of experimental setups, providing physical insight on the mechanisms at play and on system parameters that would otherwise be very difficult to measure. The details concerning this method and the results regarding exciton dynamics in multilayered organic nanofibers were published[3] and chosen as an Editor's Pick. The paper is presented in section 6.

The information we were able to gather from this theoretical/experimental scheme was so rich that it presented lots of opportunities for further studies. One of these is a study focusing on exciton diffusion in P6P and 6T. Let us turn to it.

CHAPTER 4

SIMULATING EXCITON DIFFUSION

Investigating Exciton Diffusion

As mentioned in the last chapter, exciton diffusion is one of the main processes behind the working of organic photovoltaic devices. The capacity of an exciton to reach a donor-acceptor interface is one of the key aspects governing the efficiency of such devices.

Three intertwined properties are of particular importance in singlet exciton diffusion: exciton lifetime, its Förster radius and intermolecular distances. Having obtained values for these parameters from the analysis of experimental data presented in the last chapter, it is now possible to investigate further the process of exciton diffusion. In particular, since the above mentioned parameters are affected by factors such as temperature, morphology and dimensionality, the opportunity presents itself to understand how changes in these factors translate into exciton diffusion.

In the experiments involving P6P and 6T, it was observed that the temperature dependence of Förster transfers in each material were completely different. In addition, the multilayered morphology included confinement effects and some of the layers were 4 Å thick, which amounts in practice to a one-dimensional structure for excitons to diffuse.

In this sense, we employ the Kinetic Monte Carlo model to investigate the effects of temperature and dimensionality on singlet exciton diffusion in both P6P and 6T. Building on the previous results - experimental radiative lifetimes[2], equation 3.9 for the temperature dependence of Förster radius in P6P and average intermolecular distances[3] -, simulations of exciton diffusion are run in one and two dimensional lattices.

Improving the KMC Model

To better understand exciton diffusion, the Kinetic Monte Carlo program had to be improved. Instead of only reproducing TRPL experiments by registering the amount of excitons that recombine radiatively at each time, the program now would register as well the position of each exciton. Furthermore, the way by which the morphology of the system was generated was changed to produce one and two dimensional square lattices with intersite distances being calculated for each neighboring site instead of using a single distance as before. These lattices simulate exciton transfers between nanofibers in a single layer and in the bulk. For the one-dimensional system, 1000 sites were used. In the two-dimensional case, a 100×100 grid was employed. These lattice sizes were chosen so as to prevent border effects.

Simulations were run twice. First with 100,000 excitons, registering their total displacement and lifetimes. These simulations ended only after all excitons had recombined. Then, to analyze the process of exciton diffusion as it unravels in time, it was also necessary to be able to save the displacement of each exciton at every step of the simulation. So the second round of simulations was run with 30,000 excitons, registering their positions at each moment in time up to 2000 ps. A temperature range from 80 K to 300 K was considered and exciton-exciton interactions were disregarded, as often under experimental conditions exciton concentrations are low.

The Role of Temperature and Dimensionality

Using the simulations that register exciton displacement at each time, we may calculate the time evolution of the variance of these displacements. This allows us to follow the spread of excitons in the lattice. Figure 4.1 shows these results for the x coordinate of excitons in P6P and 6T in one and two dimensional lattices for all temperatures considered. It can be seen that the variances increase linearly with time. This is the hallmark of a normal diffusion process[47].

The angular coefficient of these straight lines is known as the diffusion constant or diffusion coefficient. In Figure 4.2, the diffusion constant for each material and dimensionality is shown as a function of temperature along with average exciton lifetimes. It can be seen that this feature shows temperature dependence on both materials, much more so in P6P. Importantly, the diffusion constants found are within typical values for organic materials[40].

The observed temperature dependence can be mapped to the corresponding decreases in exciton lifetimes associated with the behavior of the Förster radius, which either increases - as observed in P6P - or remains constant - as is the case in 6T. This behavior may be interpreted as resulting from increases in spectral overlap produced by spectral shifts toward lower energies that are made possible with the larger energetic disorder found at higher temperatures. Such effect makes Förster transfers more efficient, compensating or outweighing the observed drops in exciton lifetimes.

Considering the dimensionality effects, it is noticeable that the detachment between diffusion
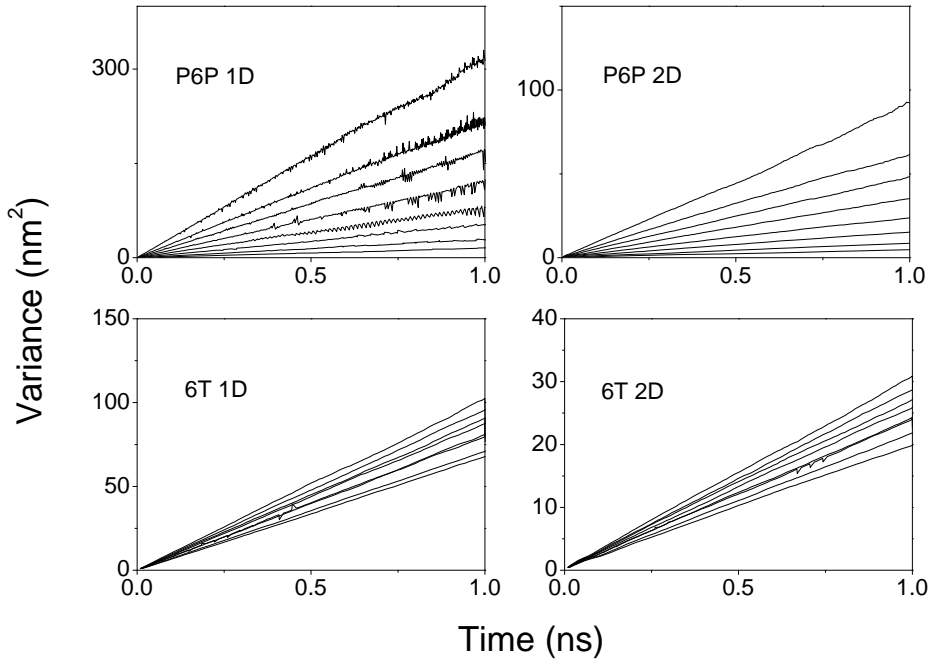
Figure 4.1: Variance of exciton displacements as a function of time for P6P and 6T in one and two-dimensional lattices. Each curve corresponds to a different temperature ranging from 80 K to 300 K. Curves become more inclined as temperature increases. Reproduced from reference [5].

constants in both morphologies becomes larger with temperature. It is expected that diffusion constants for one direction obtained in 2D simulations be smaller than the ones obtained in a 1D morphology, more exactly, smaller by a factor of two. Nevertheless, the observed difference is larger, pointing to an important role played by dimensionality.

The most important measure of efficiency in exciton diffusion is the diffusion length. This parameter is defined as the standard deviation of the squares of displacements. Its relation to the diffusion constant is known as Fick's law[40]

$$L_D = \sqrt{ZD\tau}. \tag{4.1}$$

In this expression[1], $Z = 1, 2, 3$ is the dimensionality of the process, D is the diffusion constant and τ the average exciton lifetime. Exciton diffusion lengths in P6P and 6T are shown in Figure 4.3, for both one and two-dimensional morphologies. As expected from the different temperature dependence of the Förster radius in the two materials, diffusion lengths in P6P increase significantly with temperature whereas it remains constant in 6T. This is all in line with experimental results[45, 2].

Interestingly, diffusion lengths calculated in the different morphologies show considerable differences, being larger in one-dimensional settings even though the simulations employ the same

---

[1]The original expression for diffusion length includes a factor of 2 inside the square root, but it is commonly found in the literature without this factor as well, see reference [40]
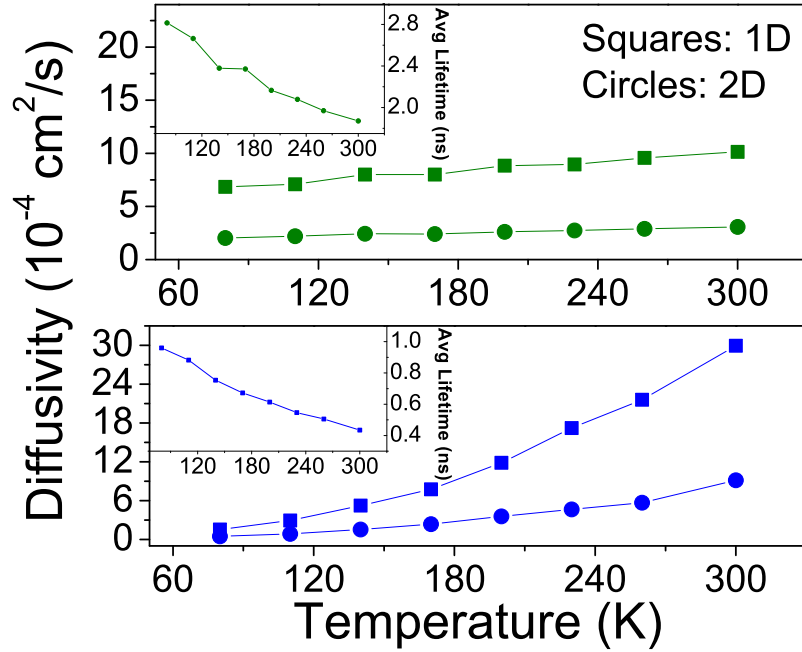
Figure 4.2: One-dimensional exciton diffusion coefficients in 6T (top, green) and P6P (bottom, blue) in the 1D (squares) and 2D (circles) morphologies as a function of temperature. Inset shows the average exciton lifetime for each temperature. Reproduced from reference [5].

Förster radii, exciton lifetimes and intersite spacing. What actually produces the difference in results is that simulations in the two-dimensional lattice include neighboring sites with different distances. In the one-dimensional case, an exciton may hop only to two sites that are 10 Å apart. In the two-dimensional case, there are 8 first neighbors, half of which are 10 Å away (those in the vertical and horizontal directions). The other 4 diagonal neighbors are 14.1 Å away. Since the Förster transfer presents an inverse sixth power dependence on intersite distance, the 41% increase in distance produces an 8 fold reduction in the transfer rate. This makes hops towards these farther sites less likely to occur, but not unlikely enough to prevent it from happening at all. These transfers take longer time to be performed and show larger probability of resulting in exciton recombination in comparison to hops to closer sites. In other words, these extra sites may serve as traps, attracting excitons to transfers they are unlikely to survive.

Comparison with Experiments

Several techniques for measuring exciton diffusion length exist. One of the most often employed is the fluorescence quenching in bilayers[40], which measures one-dimensional diffusion lengths, meaning the 1D projection of the diffusion length in a given direction. For instance, in the case of the 2D simulations, such 1D projection remains constant at 7.6 nm in 6T and ranges from 2.2 nm to 6.4 nm in P6P. These values are considerably lower than the ones found for the 1D morphology.

Experimental estimates of this one-dimensional diffusion length have been published for both
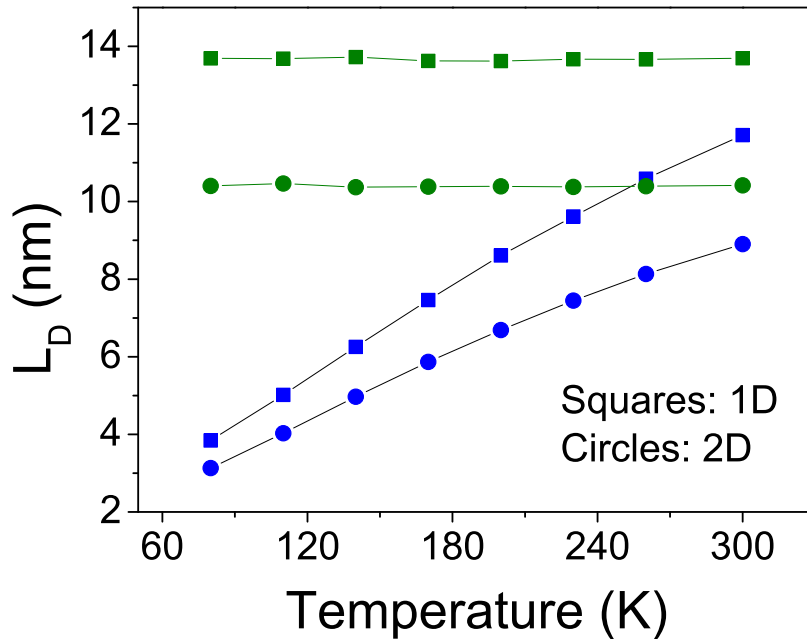
Figure 4.3: Exciton diffusion lengths in P6P (blue) and 6T (green) for one and two-dimensional morphologies. Reproduced from reference [5].

molecules using the above mentioned technique[45, 48]. These works estimate exciton diffusion length to be around 60 nm in 6T and 30 nm in P6P. These values are much larger than the ones obtained from the simulations, even when considering the largest ones, that is, those for one-dimensional morphologies.

The large disagreement between experimental reports and simulations require further investigation. A relevant information, in this sense, is the distribution of one-dimensional absolute displacements for excitons in both materials. These are shown in Figure 4.4 for the 300 K simulations. Exciton displacements of 60 nm or more in 6T are verified only for 3% and 0.1% of excitons in the 1D and 2D morphologies, respectively. In P6P, only 0.2% and 0.002% of excitons recombine at distances of at least 30 nm in 1D and 2D simulations, respectively. These numbers actually underestimate the amount of excitons that at any point reach such distances, since some of them may cross this mark and diffuse back, which would not be possible in a fluorescence quenching experiment. This is not enough, however, to account for the differences between experiment and simulations. A plausible explanation may be that the experiments overestimate exciton diffusion in these two materials, measuring instead, the tails of the displacement distributions. In other words, it is as if the experiments measured the distance traveled by a small fraction of the excitons and take this value as representative of exciton behavior in the whole system.
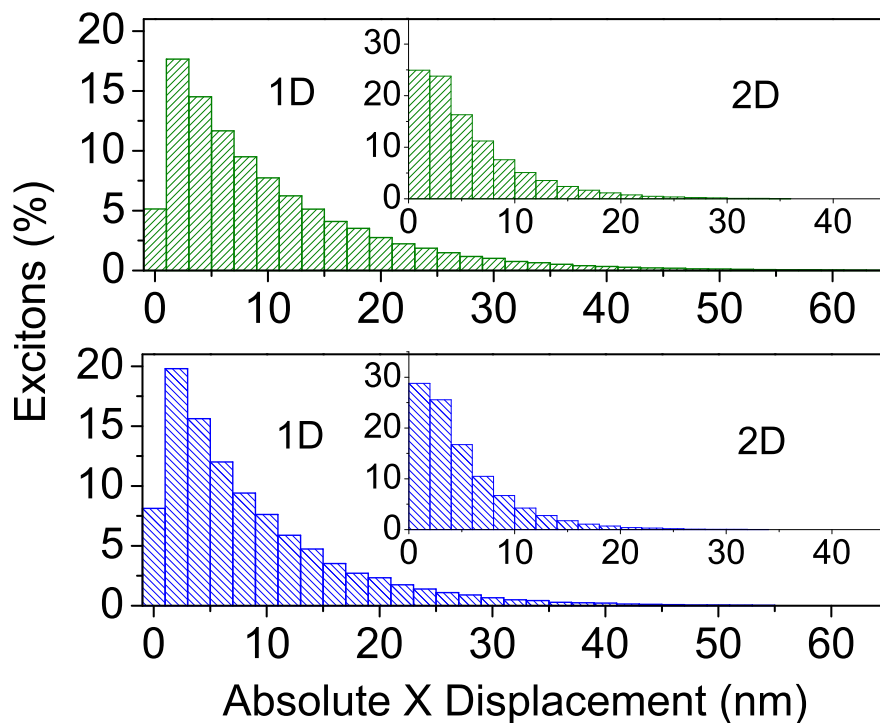
Figure 4.4: Distribution of absolute one-dimensional displacements for excitons in 1D and 2D morphologies in 6T (top) and P6P (bottom). Results correspond to simulations run at 300 K. Reproduced from reference [5].
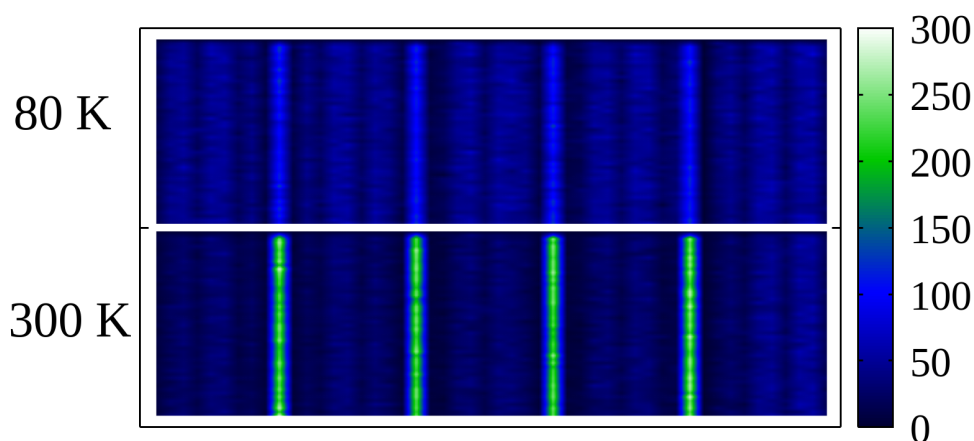
Figure 4.5: Simulated emission map for excitons in a multilayered P6P-6T morphology. Reproduced from reference [5].

Revisiting the Multilayered Morphology

The improved KMC program allows us also to obtain further insight into the dynamics of excitons in the multilayered morphology that was the subject of our attention in the last chapter. As explained previously, Förster transfers from 6T to P6P are not allowed for lack of spectral overlap. The reverse transfer, on the other hand, is allowed and presents an experimentally estimated Förster radius of 36 Å[48]. By running simulations in this multilayered morphology and registering the positions where exciton recombination takes place, it is possible to visualize the optical consequences of exciton diffusion in this system in the form of an emission map. Figure 4.5 shows the simulated emission maps for the 80 K and 300 K cases. At the lower temperature, the 6T layers can barely be distinguished as only excitons that were generated near these layers migrate and recombine there. As such, most of the excitons recombine in the P6P material, emitting blue light. The darker regions at the vicinity of the P6P-6T interfaces show this exciton draining effect which results from the large Förster radius for the P6P to 6T transfer. At higher temperatures, exciton migration from one material to the other becomes very significant. Larger portions of the P6P layers are drained from excitons, as the Förster radius in this material increases. This, in turn, translates into a larger number of excitons that manage to reach the interface. Now, as these excitons become trapped in the 6T layers, they all recombine there, changing the optical properties of the device, which now emits mostly green light.
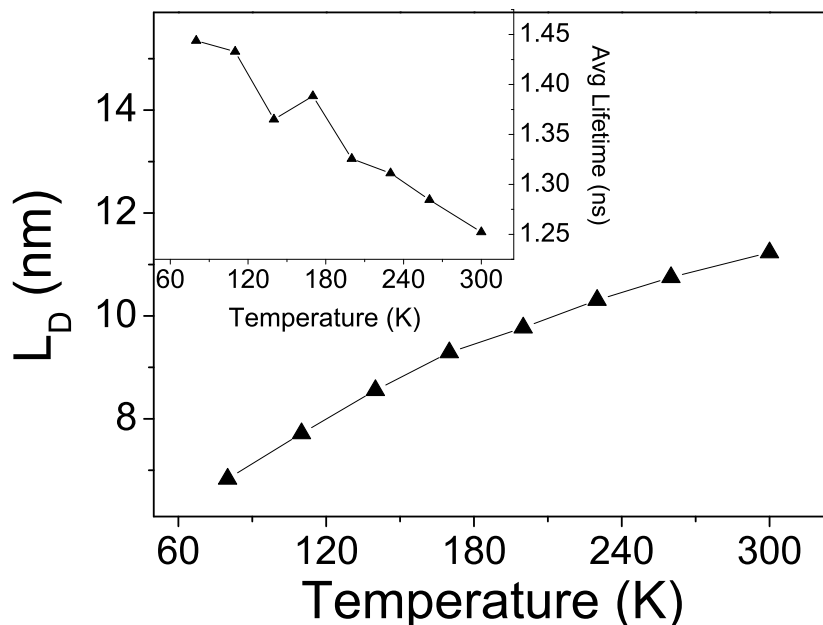
Figure 4.6: Exciton diffusion lengths and average lifetimes for the multilayered P6P-6T morphology. Reproduced from reference [5].

Furthermore, we may also investigate the effects in exciton diffusion length of combining these two materials in the multilayered morphology. This is particularly interesting, as this morphology combines the practically one-dimensional 6T layers with the larger two-dimensional P6P layers.

In addition, it mixes the different temperature dependences of Förster transfers present in both materials. Figure 4.6 shows exciton diffusion lengths and lifetimes as a function of temperature for this morphology. Lifetimes go from 1.4 ns to 1.3 ns in the temperature range considered, thus changing only mildly, a behavior that is more characteristic of excitons in 6T. The diffusion length, in its turn, varies from 6.8 nm to 11.2 nm, showing the profile of a temperature activated process, similar to the one observed in pure P6P.

The results shown thus far were published[5] and the paper is presented in section 6.

Towards Ab Initio Estimates of Exciton Diffusion Length

During the review process of the article that presented the previous results, one of the referees pointed out quite correctly that in situations regarding morphologies composed of single materials, the use of KMC simulations could be dispensable as analytical treatments would be possible. This would be the case since temperature dependences are built in parametrically in the model. Indeed, once Förster radii and intersite distances are set, the situation becomes quite simple. The point is that, in order for us to obtain such parameters, a whole process involving comparisons between KMC simulations and experiments was required. In addition, the consideration of more complex morphologies and exciton transfers between different materials made the use of simulations invaluable.

This observation, however, presents an interesting possibility. If one is able to obtain reliable estimates of Förster radii and intersite distances for different materials, it would be possible to provide estimates of exciton diffusion length without the need to resort to KMC simulations. Fortunately, I had exactly the tools to do so.

As mentioned previously, among the uses found for the simulation of absorption and emission spectra was precisely the calculation of Förster radii. The radii by themselves were not particularly interesting. However, if an analytical model for exciton diffusion could be developed, one would be able to obtain estimates of exciton diffusion length by means of ab initio calculations only. This would give greater significance to the capacity to calculate Förster radii.

An Analytical Model for Exciton Diffusion

The concept of Förster radii is useful as it allows for the expression of the Förster rate in simpler terms, as

$$k_F = \frac{1}{\tau_{emi}} \left(\frac{R_F}{r} \right)^6 . \tag{4.2}$$

Typical intermolecular distances in molecular crystals can be estimated to be around 5 Å, give

or take. For such small distances, equation 4.2 actually overestimates considerably the rate of exciton transfer[49]. It is worth noting that the genetic algorithm employed in the last chapter estimated these distances to be of 10 Å in P6P. This somewhat larger value for intermolecular distances points already to its interpretation as more of an effective distance for Förster transfers rather than actual physical distance. As a matter of fact, this shortcoming of Förster theory was addressed by means of a change in the expression of equation 4.2. This new expression for the Förster radius is then set as[50]

$$k_F = \frac{1}{\tau_{emi}} \left(\frac{R_F}{l+r} \right)^6 , \tag{4.3}$$

where l corresponds to an estimate of the molecule's conjugation length.

A second study employed this expression to calculate the maximum diffusion length possibly achieved by singlet excitons[24]. In this study, the parameter l was taken as proportional to the molecule's transition dipole moment μ, that is, $l = \alpha\mu$. By testing this expression for different molecules, the α constant was found to be approximately $1.15\ e^{-1}$, where e is the charge of the electron. This correction should be then taken into consideration in the analytical model.

Having taken care of the issue regarding intermolecular distances, we turn to morphology. Morphology is known as a key factor affecting exciton diffusion[51]. Results shown thus far in this chapter have demonstrated the effect the presence of extra potential acceptor sites produce in exciton diffusion. Sites that are farther are less likely to receive an exciton transfers and present higher probabilities for recombination, but sometimes such transfers are attempted. In addition, as the dimensionality of the process increases from 1 to 3, the number of such neighboring sites increases as well. So, to take these observations into account, we resort to the calculation of a weighted average hopping distance for four scenarios: one, two and three-dimensional crystalline lattices and also a 3D amorphous morphology. As such, we are able to evaluate the role played by both dimensionality and order.

In the case of crystalline lattices, we take the cubic lattice as representative of an ordered morphology. In this case, site positions are given by $\vec{r} = r_{min}(n_x, n_y, n_z)$, where n_x, n_y and n_z are integers. Crystalline arrangements differ from molecule to molecule, but for the purposes of calculating an average hopping distance, the cubic lattice should be enough to capture the effects of an ordered morphology in exciton diffusion. The one and two-dimensional cases can be treated by setting one or two of the integers as zero. These lower dimensional cases are relevant because, depending on molecular arrangement, exciton diffusion may be restricted to a plane or even a single direction, as it possesses a dependence on the relative orientation between donor and acceptor. For these crystalline morphologies, the average hopping distance is calculated as

$$\bar{r} = \frac{\sum\limits_{n_x, n_y, n_z} |\vec{r}| k_F(|\vec{r}|)}{\sum\limits_{n_x, n_y, n_z} k_F(|\vec{r}|)} , \tag{4.4}$$

with the summation being run for 100 neighboring sites in each direction.

To treat the case of an amorphous morphology, we observe that the main difference resides in the fact that neighboring sites may be present at all distances. Considering diffusion to be isotropic, with acceptor sites equally and continuously distributed in all directions, we substitute the summation in equation 4.4 with integrals over all space. The calculation may then be performed analytically and reads

$$\bar{r} = \frac{\int_{r_{min}}^{\infty} r k_F(r) dr}{\int_{r_{min}}^{\infty} k_F(r) dr} = \frac{l + 5r_{min}}{4}. \tag{4.5}$$

The distance r_{min} that is present in equations 4.4 and 4.5 corresponds to a minimum intermolecular distance for which orbital overlap may be considered negligible. This requirement is justified by the fact that for shorter distances, the dominant mechanism for exciton transfer becomes the Dexter transfer[8]. This distance that marks the boundary at which the Förster mechanism becomes dominant has been estimated to be about 5 Å in a study[52]. Thus, we assign this value of 5 Å to the minimum distance r_{min}.
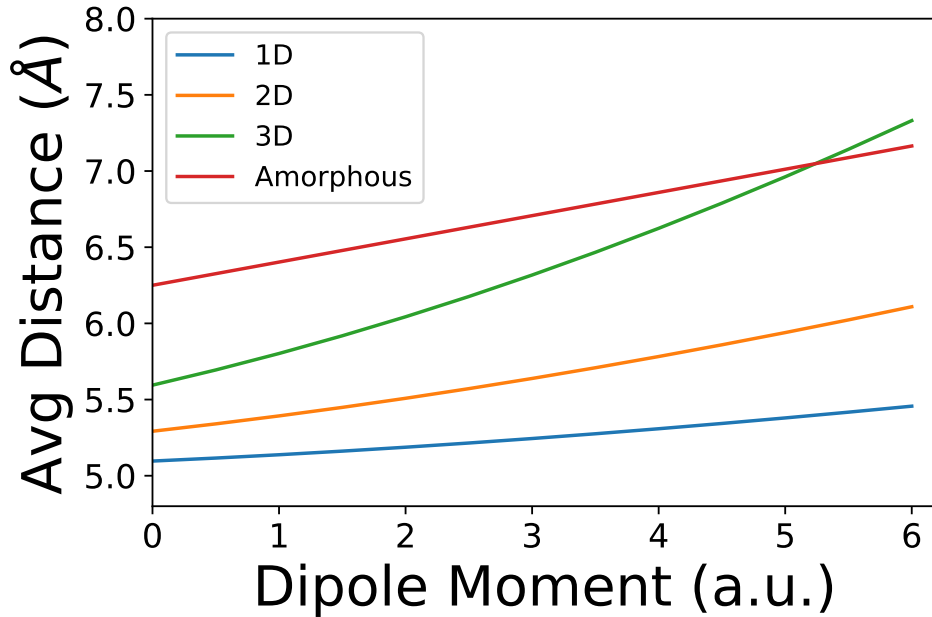
Figure 4.7: Average hopping distances as a function of transition dipole moment for the different morphologies considered.

Because of the modification made to the Förster rate equation, the average hopping distances present a dependence on the transition dipole moments. These are shown in Figure 4.7. It can be seen that increases in dipole moment produce increases in the average hopping distances, more so in the case of three-dimensional morphologies. In addition, morphologies with higher dimensionality present larger average hopping distances, with the largest values found for the amorphous case. These differences will affect exciton diffusion lengths considerably.

The connection between these average hopping distances and exciton diffusion length is made by treating exciton diffusion as a random walk, which is appropriate to treat a normal diffusion process. This is in line with studies that have verified normal diffusion in the context of exciton

diffusion[53, 54, 55, 56]. In a random walk, the variance of the walker's displacements - which defines the square of the diffusion length - equals the average hopping distance squared times the number of hops ($L_D^2 = \bar{r}^2 n_{hops}$). The number of hops can be calculated as the exciton average lifetime divided by the average time it takes for a hop to occur. This, in turn, can be estimated as the inverse of the average Förster rate. Combining these ideas with our modified Förster rate yields

$$L_D = \bar{r} \left(\frac{R_F}{\alpha\mu + \bar{r}} \right)^3 . \tag{4.6}$$

Finally, remember the discussion regarding the experimental techniques that usually measure one-dimensional projections of the exciton diffusion length. To adjust for this fact, calculated diffusion lengths in 3D and 2D are divided by $\sqrt{3}$ and $\sqrt{2}$, respectively. This is justified if we consider exciton diffusion as isotropic.

Developing a Computational Protocol
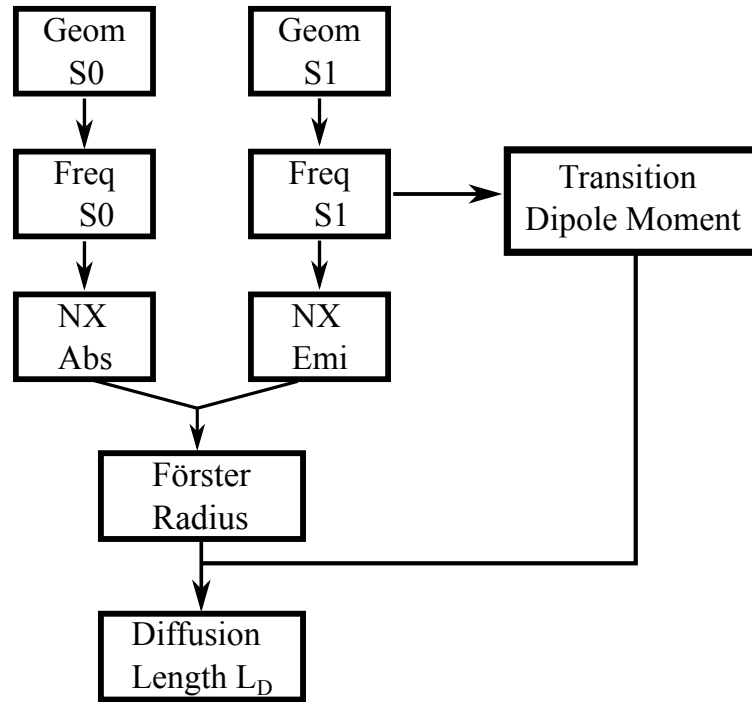
Figure 4.8: Schematics of the computational protocol employed to calculate singlet exciton diffusion lengths from ab initio calculations.

The combination of spectrum simulations with the analytical treatment shown above results in a computational protocol that allows for the calculation of singlet exciton diffusion length for a variety of materials. Figure 4.8 shows the schematics that describe this protocol.

The first step comprises quantum chemical calculations for geometry optimization at both the S_0 and S_1 states, which are followed by normal mode analysis. Normal mode analysis in S_1

also provide transition dipole moments, which we need in equation 4.6. These quantum chemical calculations are used as input to absorption and emission spectrum simulations.

Once the spectra are ready, they are used in concert to obtain the Förster radius for this particular molecule. Since our treatment assumes isotropic diffusion, the orientation factor was taken as $\kappa^2 = 2/3$, which is the average value for randomly oriented molecules. Finally, the Förster radius is combined with the transition dipole moment and the average hopping distances using equation 4.6 to produce estimates of singlet exciton diffusion length.

To test the computational protocol, a set of molecules of interest in the field of organic electronics was chosen. Quantum chemical calculations were performed using density functional theory (DFT) and time-dependent density functional theory (TD-DFT) with the Gaussian 16 program suite[57]. The 6-31G(d,p) basis set was used in all cases. The M062X functional was chosen for calculations with P6P and 6T, following previous studies[2, 3]. For the remaining molecules, the B3LYP functional was used, as it has been shown to to well reproduce experimental spectra[1, 58].

For these spectrum simulations, we use the nuclear ensemble method[13] as implemented in the Newton-X software[12]. All spectra simulations were performed by sampling 500 geometries and using Gaussian spectral line shapes with a broadening factor of 0.05 eV.

Testing the Method

Table 4.1 presents the list of molecules chosen for testing the computation protocol. They are shown along with their calculated Förster radius. The listed molecules possess Förster radii ranging from 15.8 Å to 43.7 Å, covering a quite large interval that includes molecules with different amounts of potential as favorable materials for exciton diffusion.

Molecule	Förster Radius (Å)
Naphthalene	21.8
Anthracene	29.0
Tetracene	35.2
Pentacene	41.6
Para-hexaphenyl (P6P)	32.4
α-sexithiophene (6T)	40.6
tris(8-hydroxyquinoline) aluminum (AlQ3)	18.9
Diindenoperylene (DIP)	43.7
1,4-Dibromonaphtalane	25.0
N,N0-dicarbazolyl-3,5-benzene (mCP)	15.8
Pyrene	34.5

Table 4.1: Molecules for which the protocol was tested along with their corresponding Förster radii calculated from spectrum simulations.

Following the calculation of Förster radii, we turn to the average hopping distances for each morphology. Results are shown in table 4.2. The effects of larger dimensionality and transition

dipole moments in the increase of the average hopping distance is observed. It can also be seen that the averaging procedure produces very significant changes in hopping distance in comparison with the original minimum hopping distance $r_{min} = 5$ Å. One particular case calls attention, the case of P6P. With the values for its transition dipole and average hopping distances, we may evaluate the effective interaction distance $(\alpha\mu + \bar{r})$, obtaining values of around 10 Å. This is remarkable because it reproduces the intersite distance found in completely independent fashion with the aid of the genetic algorithm[3], as shown in the last chapter.

Molecule	Dipole Moment (a.u.)	Crystal (Å) 1D	2D	3D	Amorphous (Å)
Naphthalene	0.9	5.1	5.4	5.8	6.4
Anthracene	0.9	5.1	5.4	5.8	6.4
Tetracene	1.0	5.1	5.4	5.8	6.4
Pentacene	1.0	5.1	5.4	5.8	6.4
P6P	5.7	5.4	6.1	7.2	7.1
6T	5.9	5.4	6.1	7.3	7.2
AlQ3	0.0	5.1	5.3	5.6	6.3
DIP	1.3	5.2	5.4	5.9	6.5
Dibromonaphtalane	1.3	5.2	5.4	5.9	6.5
mCP	1.3	5.2	5.4	5.9	6.5
Pyrene	1.9	5.2	5.5	6.0	6.5

Table 4.2: Transition dipole moments and average hopping distances for each molecule for the four morphologies considered.

Molecule	Exciton Diffusion Lengths (nm) 1D	2D	3D	Amorphous	Experimental
Naphthalene	29	19	14	12	23[59]
Anthracene	68	44	32	27	40-60[60, 61]
Tetracene	120	78	57	48	60[62]
Pentacene	198	129	93	78	65[63]
P6P	26	17	12	12	30[48]
6T	49	32	22	22	60[45]
AlQ3	26	17	12	10	10-30[64, 65, 66]
DIP	203	132	95	81	100[67]
Dibromonaphtalane	38	25	18	15	-
mCP	10	6	4	4	-
Pyrene	83	54	38	34	-

Table 4.3: Estimated exciton diffusion lengths for one, two and three dimensional crystal lattices and amorphous morphology. Experimental results are also provided.

With the results from tables 4.1 and 4.2 and using equation 4.6, singlet exciton diffusion lengths are estimated for the different morphologies. Results are presented in table 4.3. The obtained values for diffusion length range from 4 nm to 200 nm, which goes to show the large variability in exciton diffusion properties in organic materials. Increases of dimensionality and

disorder result in lower values for diffusion length. This is expected, since equation 4.6 presents a roughly inversely proportional relationship with respect to the hopping distance squared.

The estimates shown here for diffusion length can be compared to experimental results. These comparisons are made somewhat more difficult by the considerable variability of reported results. This state of affairs results from differences in methodology and sample conditions. As seen in table 4.3, experimental values of diffusion length are found to be between the minimum and maximum estimates, that is, between the results obtained for amorphous and 1D crystalline morphologies. The exceptions can be seen to be pentacene, P6P and 6T. As to pentacene, the methodology overestimates diffusion lengths because of the phenomenon of singlet fission, which produces triplet excitons and effectively reduces singlet exciton lifetime in this material. This process has been shown to reduce exciton diffusion length to 12 nm at room temperature[63], much lower than our predicted values. This effect could be accounted for by considering a lower exciton lifetime in pentacene. This change should correct the corresponding Förster radius and diffusion length accordingly. A different situation is found when it comes to P6P and 6T. As we have already discussed, there is evidence pointing to the conclusion that experimental reports seem to be overestimating exciton diffusion length in these two materials, which, as demonstrated in this chapter, were estimated to be around 12 and 14 nm, respectively[5]. The ab initio calculations, however, put diffusion lengths in these materials at 12 nm and 22 nm in amorphous morphologies, respectively. It can be seen that the estimates for P6P are similar, but the ab initio method predicts larger diffusion lengths in 6T.

Comparison between the estimates for the various molecules show that diffusion lengths are affected differently by increases in morphological order. When changing morphology from 3D amorphous to 1D crystal, total exciton diffusion lengths, i.e., those obtained before dividing by $\sqrt{3}$, are found to increase, on average, 41%. Two extreme cases are worth noting, however: AlQ3 shows a 50% increase, whereas, in contrast, for 6T this increase is just 25%. The factor responsible for this difference is the transition dipole moment. There is an inverse correlation between dipole moments and increases in exciton diffusion length. This indicates that investments in morphological order should be less effective at increasing exciton diffusion length in molecules with large transition dipole moments.

Treating Heterodimers

The above results concern exciton transfers among homodimers, but it is also possible to calculate Förster radii for heterodimers. Figure 4.9 shows the Förster radii for all combinations of donors and acceptors possible from the molecules studied here. For some pairings of molecules, Förster transfers are only allowed in one direction, as is the case of P6P and 6T, which we have already analyzed in detail. On the other hand, for a DIP/Tetracene heterodimer, Förster transfers are allowed on both directions.
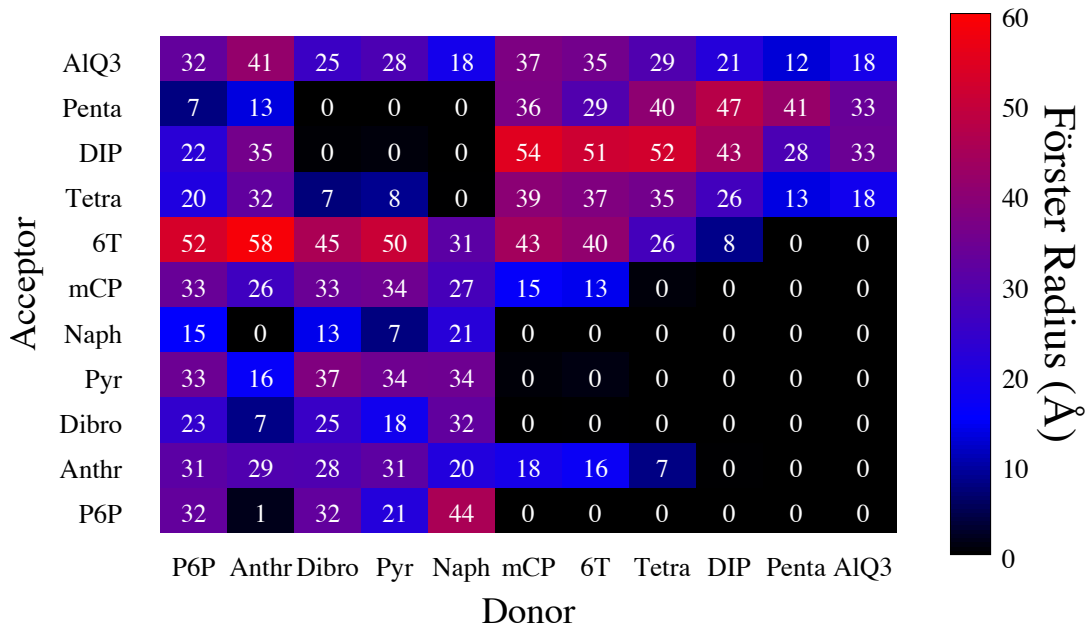
Figure 4.9: Table showing the Förster radii for all possible combinations of donors and acceptors.

Exciton transfer between heterodimers are relevant for different reasons. First, as we have seen, devices composed of two or more different materials may possess interesting optical properties derived from exciton migration and confinement. Second, large Förster radii at donor-acceptor interfaces may turn Förster transfers into a competing factor against exciton dissociation[68, 69]. This may become a limiting factor to the efficiency of organic photovoltaic devices, for instance.

Taking for example the case of the mCP/DIP pair, we may evaluate the rate of Förster transfer from the first to the latter at $1.3 \times 10^{12}\ s^{-1}$, given its radius of 54 Å. The transfer in the opposite direction is not allowed, which shows the possibility of exciton confinement again. The allowed transition, however, shows a large value - comparable to estimates of charge transfer rate[70] - which demonstrate the need to take this possibility into account when analyzing and designing optoelectronic devices. The findings presented here, as well as the computational protocol itself - which is straightforward to employ -, may prove valuable for the rational design of devices.

CHAPTER 5

CONCLUSIONS AND PERSPECTIVES

The story behind this thesis may be summarized as the quest to find some use to two simulated absorption and emission spectra. The need for these spectra was the starting point of the work, which went on to compare the results produced by two different methodologies, the Franck-Condon approximation and the nuclear ensemble method. It was shown that the latter provides reliable results and is not affected by the issues concerning the changes in geometry observed particularly in the case of flexible molecules. This new method became a useful tool for analyzing the electronic properties of organic materials of interest.

With the spectra for P6P and 6T on hands and no paper to which I could contribute these results, I studied in details the experiments concerning exciton dynamics in multilayered P6P-6T systems. The first result obtained was the calculation of Förster radii by using the simulated spectra. With these Förster radii, it eventually became clear that the process of exciton diffusion could be simulated and experimental results could be reproduced in order to gain physical insight for this process. Inspired by the work done with colleagues at the University of Linköping, I developed my own Kinetic Monte Carlo code for simulating time-resolved photoluminescence spectra.

The actual reproduction of experimental data proved more complicated than it seemed at first. A genetic algorithm was required to obtain, by means of hundreds of comparisons between simulation and experiment, the best values for the parameters that controlled the simulation. This process showed the need to consider exciton-exciton interactions, in particular the presence of the biexciton cascade emissions. This was the first physical insight of interest derived from the model I had built.

In addition, the optimal parameters found by the genetic algorithm were able to reveal details on the temperature dependence of the exciton diffusion process in both materials. It showed how exciton transport in P6P is a temperature activated process whereas in 6T it shows no significant temperature dependence. Furthermore, it provided estimates for the effective interaction distance

for Förster transfers from P6P and 6T.

These results opened the door for various studies. Having obtained the parameters that controlled exciton diffusion in both P6P and 6T, it became possible to investigate in details the factors that may affect this process and to obtain values for two features that are key to quantifying the ease with which exciton diffusion takes place: diffusion constants and diffusion lengths. Two interesting results were obtained. First, the realization that dimensionality may actually be an important factor to exciton diffusion even when morphologies are highly ordered. Second, the suspicion that previous experimental works had greatly overestimated diffusion lengths in these two materials.

At this point, it became clear that once the important parameters governing Förster transfers were known, simulations performed in simple morphologies could be dispensed with as the problem became amenable to analytical considerations. A correction to the expression for the Förster rate allowed for the elimination of overestimating errors that were known to happen for short intermolecular distances. Combined with that, a random walk model was able to calculate exciton diffusion lengths with a measure of hopping distance and a value for the Förster radius of the transfer. The effects of morphology and dimensionality were included by means of a weighed averaging procedure applied to hopping distances. In concert, these measures proved possible to estimate singlet exciton diffusion lengths, making for a straightforward ab initio procedure that starts by simulating absorption and emission spectra. Here the work comes full circle.

The ensemble of techniques shown here have proved valuable in the two main objectives of simulations: providing explanations for observed results and making predictions concerning measurable phenomena. In the realm of organic electronics, the insights produced by these methods may hopefully translate into strategies for the rational design of devices. If not, then let it at least provide some clarity to a complex field of study in which many different factors play important roles in phenomena such as exciton diffusion and dissociation and charge transfer and recombination.

The versatility of the Kinetic Monte Carlo method is perfect for application in this field. Apart from the results presented in this thesis, extensions for the KMC model have already been developed. These extensions allow for the simulation of charge separation in donor-acceptor interfaces and are currently being employed in a study with Professor Gjergji Sini of the University of Cergy-Pontoise, which I had the pleasure of visiting twice during my PhD work. As a next step, a combination between the models for exciton diffusion and charge transport is under development and may prove useful to studying the effects of Förster transfers at donor-acceptor interfaces in the efficiency of exciton dissociation.

As the amount of ideas for applications have fortunately surpassed my capacity to tackle them alone, the models shown here have been adopted by students and are now part of their scientific projects. Three such projects stand out, the study of exciton-exciton interactions in detail, the role of energetic disorder in exciton diffusion and the extension to polymers of the computational protocol devised for estimating exciton diffusion lengths. Hopefully, interesting results should start to appear in the coming months.

Some improvements to the KMC model have already been implemented and are now patiently waiting to be employed. These include the treatment of more complex morphologies such as bulk heterojunctions and the consideration of positional disorder. Furthermore, several changes and extensions can be thought of. For instance, the model may be adapted to treat triplet excitons as well by including the equations for Dexter transfer. This would allow also for the study of the phenomena of singlet fission and triplet fusion responsible for delayed fluorescence. The effects of dynamic disorder and lattice dynamics may also be subjects of interesting studies in the near future.

In summary, there is plenty still to be done.

CHAPTER 6

ARTICLES PUBLISHED DURING THIS THESIS

Article 1

Modeling the Emission Spectra of Organic Molecules: A Competition between Franck–Condon and Nuclear Ensemble Methods

Leonardo Evaristo de Sousa, Luiz Antonio Ribeiro Junior, Antonio Luciano de Almeida Fonseca, and Demétrio Antonio da Silva Filho*

Institute of Physics, University of Brasília, 70.919-970 Brasília, Brazil

ABSTRACT: The emission spectra of flexible and rigid organic molecules are theoretically investigated in the framework of the Franck–Condon (FC) and nuclear ensemble (NE) approaches, both of which rely on results from density functional theory but differ in the way vibrational contributions are taken into account. Our findings show that the emission spectra obtained using the NE approach are in better agreement with experiment than the ones produced by FC calculations considering both rigid and flexible molecules. Surprisingly, the description of a suitable balance between the vibronic progression and the emission spectra envelope shows dependency on the initial sampling for the NE calculations which must be judiciously selected. Our results intend to provide guidance for a better theoretical description of light emission properties of organic molecules with applications in organic electronic devices.
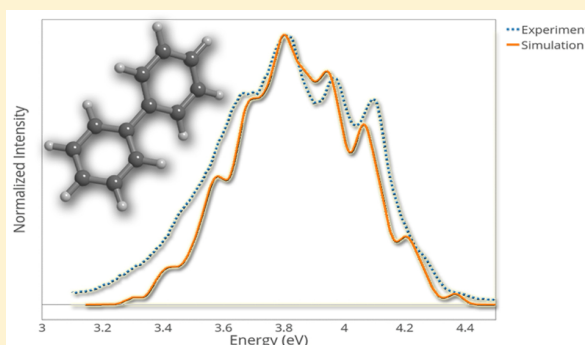
INTRODUCTION

Organic semiconductors have been the main subject of a very active research field which aims at developing more efficient carbon-based optoelectronic devices, mostly for green energy applications.[1,2] Particularly, there is great interest in designing new materials to be used in these devices.[3,4] Among several technological applications developed so far, organic light-emitting diodes (OLEDs) have proven to be of great economic importance, being part of most display technologies which have already hit the market.[5,6] Albeit the synthesis of organic compounds for fabrication of optoelectronic devices is usually cheaper than for their inorganic counterparts, finding possible channels to characterize the physical properties of materials before synthesis may be essential to reduce costs and increase the efficiency of the whole process.[7,8] When it comes to OLEDs, an especially important property is the emission spectra of the molecule that is a candidate to be used as active material in these devices.[9,10] Therefore, the development of methodologies that can accurately predict the emission spectra of organic semiconductors is of major interest.

The simulation of emission spectra requires some level of approximation to be performed, the most common being the Franck–Condon (FC) approximation. The FC approximation considers the electronic dipole moment to be constant, which makes the transition probability proportional to the square of the overlap integral between the vibrational wave functions of the ground and excited electronic states.[11] In the core of this method lies the assumption that during a transition between vibronic states, the positions of the nuclei remain almost unchanged. Recently, a study about the selection of functionals and other parameters in FC simulations was carried out

considering several organic molecules.[12] In this study, one of the molecules (biphenyl) had its analysis compromised due to the fact that it changed conformation from planar to twisted during emission. It is well-known that the FC approximation fails to describe the spectra of molecules whose geometry changes significantly from the ground to the excited state.[13,14] This is particularly true for molecules that go from nonplanar to planar geometry when excited. In these cases, the overlap integrals calculated nearly vanish and the spectrum simulation loses its reliability. Because organic molecules have intrinsically the property of changing its conformation upon excitation or modification in the charge state, it becomes essential to figure out other methodologies that can address properly this issue. Importantly, the alternative approach should present a suitable balance between computational cost, accuracy and useful information. It is precisely the aim of the present study to investigate an alternative method to calculate the emission spectra of flexible and rigid organic compounds that can address both types of molecules with higher accuracy than the FC method.

In this paper, we investigate the emission spectra of some rigid and flexible organic molecules based on phenyl or thiophene moieties. Particularly, the emission spectra for the bithiophene, biphenyl, and naphthalene molecules are studied for quantitative and qualitative comparisons with experiments

using both the FC and the nuclear ensemble[15−17] (NE) approximations. The first two molecules are flexible whereas naphthalene is rigid. In the Results, the spectrum progression of eight molecules are first presented, followed by the emission spectra calculations and a discussion regarding the performance of the different approaches. A correlation between the emission spectra and the changes in geometry between the ground and excited states is also drawn. The outcomes of measurements and simulation results are finally discussed to identify promising strategies to study light-emission properties of organic semiconductors.

■ METHODOLOGY

We begin our discussion by setting up the notation to be adopted in this section. In the Born−Oppenheimer approximation, the wave function for a system of n electrons and M nuclei is given by

$$\Psi_n(\vec{r},\vec{R}) = \psi_k(\vec{r},\vec{R})\, \phi_{kl}(\vec{R}) \tag{1}$$

where $\vec{r}$ denotes the set of position vectors for the electrons and $\vec{R}$ is the set of position vectors for the nuclei. The function $\psi_k(\vec{r},\vec{R})$ is the electronic wave function, depending parametrically on the positions of the nuclei. It is an eigenfunction of the electronic Hamiltonian $H_e = T_r + V(\vec{r},\vec{R})$, T_r being the kinetic energy operator for electrons,

$$H_e \psi_k(\vec{r},\vec{R}) = \varepsilon_k(\vec{R})\, \psi_k(\vec{r},\vec{R}) \tag{2}$$

and $\phi_{kl}(\vec{R})$ is the nuclear wave function, obeying

$$H_v \phi_{kl}(\vec{R}) = E_{kl} \phi_{kl}(\vec{R}) \tag{3}$$

where $H_v = T_R + \varepsilon_k(\vec{R})$ is the nuclear Hamiltonian with v standing for vibrational, as we will work in the harmonic approximation. With this notation in mind, we can now turn to the particularities of the FC and NE approximations.

Franck−Condon Approximation. We apply the Franck−Condon approximation to the expression for spontaneous emission rate obtained from quantum mechanics by means of time dependent perturbation theory.[18] This spontaneous emission rate is given by

$$\sigma_{\rm em} = \frac{4\omega^3}{3c^3\hbar} \sum_{i,m,f,n} P_{im}(T)|\langle\phi_{fn}|M_{fi}|\phi_{im}\rangle|^2 \delta(E_{fn} - E_{im} + \hbar\omega) \tag{4}$$

where the indices i and f refer to the initial and final electronic states whereas m and n refer respectively to the initial and final vibrational states.[19] $P_{im}(T)$ is the Boltzmann distribution at temperature T, M_{fi} is the electronic dipole operator, ω is the angular frequency, c is the speed of light, and δ is the Dirac delta function.

In the Franck−Condon approximation the electronic dipole is considered to be a constant, which allows us to remove it from inside the bracket, giving

$$\sigma_{\rm em} = \frac{4\omega^3}{3c^3\hbar} \sum_{i,m,f,n} M_{fi}^{\,2} P_{im}(T)|\langle\phi_{fn}|\phi_{im}\rangle|^2 \delta(E_{fn} - E_{im} + \hbar\omega) \tag{5}$$

The term $\langle\phi_{fn}|\phi_{im}\rangle$ is the so-called Franck−Condon factor. Now, restricting the calculation for emissions from the first electronic excited state ($i = 1$) to the electronic ground state ($f = 0$), we obtain

$$\sigma_{\rm em} = \frac{4\omega^3}{3c^3\hbar} \sum_{m,n} M_{01}^{\,2} P_{1m}(T)|\langle\phi_{0n}|\phi_{1m}\rangle|^2 \delta(E_{0n} - E_{1m} + \hbar\omega) \tag{6}$$

For zero temperature, the only vibrational level populated in the initial state is the ground state. Finally, we must also substitute the delta function with a Gaussian function to take into account the broadening of the lines. The result is

$$\sigma_{\rm em} = \frac{4\omega^3}{3c^3\hbar} \sum_{n} M_{01}^{\,2} |\langle\phi_{0n}|\phi_{10}\rangle|^2 G(E_{0n} - E_{10} + \hbar\omega, \delta) \tag{7}$$

where now δ refers to the broadening factor. The FC simulations use results obtained by means of density functional theory (DFT) and time dependent density functional theory (TD-DFT) calculations performed on the equilibrium geometries of the ground and first excited states. Next, we turn to the features of the NE method, which is based on a semiclassical approach.

Nuclear Ensemble Method. To derive the nuclear ensemble method we start again with eq 5 and write the Dirac delta function in its Fourier representation, yielding

$$\sigma_{\rm em} = \frac{2\omega^3}{3\pi c^3\hbar^2} \int \sum_{i,m,f,n} P_{im}(T)|\langle\phi_{fn}|M_{fi}|\phi_{im}\rangle|^2$$
$$\times \exp\left[\frac{i}{\hbar}(E_{fn} - E_{im} + \hbar\omega)t\right] dt \tag{8}$$

We may write the squared term as the product of the expectation value of M_{fi} and its complex conjugate and write part of the exponential in operator form as follows

$$\sigma_{\rm em} = \frac{2\omega^3}{3\pi c^3\hbar^2} \int \sum_{i,m,f,n} P_{im}(T)\langle\phi_{im}|M_{fi}|\phi_{fn}\rangle$$
$$\times \langle\phi_{fn}|e^{H_f t/\hbar}M_{fi}e^{-H_i t/\hbar}|\phi_{im}\rangle \exp[i\omega t]\, dt \tag{9}$$

with H_f and H_i denoting the final and initial vibrational Hamiltonian, that is, the vibrational Hamiltonian for a given initial and final electronic configuration. Defining[20]

$$M_{if}(t) = e^{H_f t/\hbar}M_{fi}e^{-H_i t/\hbar} \tag{10}$$

and performing the summation over n by taking advantage of the closure condition yields

$$\sigma_{\rm em} = \frac{2\omega^3}{3\pi c^3\hbar^2} \int \sum_{i,m,f} P_{im}(T)\langle\phi_{im}|M_{fi}M_{fi}(t)|\phi_{fn}\rangle \times \exp[i\omega t]\, dt \tag{11}$$

We now resort to the semiclassical time-dependent dipole moment approximation,[21] which treats the nuclei as fixed, restricting the time dependence of the dipole moment to

$$M_{fi}(t) = M_{fi} \exp[i\omega_{fi}(\vec{R})t] \tag{12}$$

with

$$\omega_{fi}(\vec{R}) = \frac{1}{\hbar}[\varepsilon_f(\vec{R}) - \varepsilon_i(\vec{R})] \tag{13}$$

The term in square brackets in the last equation is the so-called vertical excitation energy. Plugging this approximation in our expression for the emission rate and abandoning the Dirac notation, we obtain

$$\sigma_{em} = \frac{2\omega^3}{3\pi c^3 \hbar^2} \int \sum_{i,m,f} P_{im}(T)|\phi_{im}(\vec{R})|^2 M_{fi}^2(\vec{R})$$

$$\times \exp\left[\frac{i}{\hbar}(\hbar\omega_{fi}(\vec{R}) + \hbar\omega)t\right] dt \, d\vec{R} \tag{14}$$

Now we define $\Delta E_{fi} = \hbar\omega_{fi}$. Because we are analyzing an emission process, $\Delta E_{fi} < 0$, we may write $\Delta E_{if} = -\Delta E_{fi} = -\hbar\omega_{fi}$. By making this substitution and integrating with respect to t, we recover the delta function,

$$\sigma_{em} = \frac{4\omega^3}{3c^3\hbar} \int \sum_{i,m,f} P_{im}(T)|\phi_{im}(\vec{R})|^2 M_{fi}^2(\vec{R}) \, \delta(\hbar\omega - \Delta E_{if}(\vec{R})) \, d\vec{R} \tag{15}$$

Due to the delta function, we may insert the ω^3 factor in the integral as $\Delta E_{if}^3(\vec{R})/\hbar$. We may also change the sign of the argument of the delta function, yielding

$$\sigma_{em} = \frac{4\omega^3}{3c^3\hbar^4} \int \sum_{i,m,f} P_{im}(T)|\phi_{im}(\vec{R})|^2 \Delta E_{if}^3(\vec{R}) \, M_{fi}^2(\vec{R})$$

$$\times \delta(\Delta E_{if}(\vec{R}_j) - \hbar\omega) \, d\vec{R} \tag{16}$$

This result may be written in terms of oscillator strengths f_{fi}, which are obtained using quantum chemical calculations. Oscillator strengths are related to the dipole moment as[16]

$$M_{fi}^2 = \frac{3\hbar^2 e^2}{2m\Delta E_{if}} f_{fi} \tag{17}$$

where e and m are the charge and mass of the electron, respectively. So the emission rate reads

$$\sigma_{em} = \frac{2e^2}{mc^3\hbar^2} \int \sum_{i,m,f} P_{im}(T)|\phi_{im}(\vec{R})|^2 \Delta E_{if}^2(\vec{R}) f_{fi}(\vec{R})$$

$$\times \delta(\Delta E_{if}(\vec{R}_j) - \hbar\omega) \, d\vec{R} \tag{18}$$

Now, to account for the broadening of the spectral lines, we replace the delta function with a normalized Gaussian or Lorentzian function, denoted by G, with a broadening factor δ, resulting in

$$\sigma_{em} = \frac{2e^2}{mc^3\hbar^2} \int \sum_{i,m,f} P_{im}(T)|\phi_{im}(\vec{R})|^2 \Delta E_{if}^2(\vec{R}) f_{fi}(\vec{R})$$

$$\times G(\Delta E_{if}(\vec{R}_j) - \hbar\omega, \delta) \, d\vec{R} \tag{19}$$

Restricting again the calculation for emissions from the first electronic excited state ($i = 1$) to the electronic ground state ($f = 0$), we obtain

$$\sigma_{em} = \frac{2e^2}{mc^3\hbar^2} \int \sum_m P_{1m}(T)|\phi_{1m}(\vec{R})|^2 \Delta E_{10}^2(\vec{R}) f_{01}(\vec{R})$$

$$\times G(\Delta E_{10}(\vec{R}_j) - \hbar\omega, \delta) \, d\vec{R} \tag{20}$$

This last expression may be interpreted as the average value of $\Delta E_{10}^2 f_{01} G$ with probability density given by $\sum_m P_{1m}(T)|\phi_{1m}(\vec{R})|^2$. To perform this calculation, we may resort to an average over an ensemble. Therefore,

$$\sigma_{em} = \frac{2e^2}{mc^3\hbar^2}\left[\frac{1}{N}\sum_{j=1}^{N} \Delta E_{10}^2(\vec{R}_j) f_{01}(\vec{R}_j) \, G(\Delta E_{10}(\vec{R}_j) - \hbar\omega, \delta)\right] \tag{21}$$

with N random $\vec{R}_j$ points sampled from the $\sum_m P_{1m}(T)|\phi_{1m}(\vec{R})|^2$ distribution, which, because we are working in the harmonic approximation, is the probability density for a set of harmonic oscillators at temperature T[22]

$$\sum_m P_{1m}(T)|\phi_{1m}(\vec{R})|^2$$

$$= \prod_{j=1}^{3n-6} \sqrt{\frac{m_j\omega_j}{2\pi\hbar \sinh\left(\frac{\hbar\omega_j}{kT}\right)}} \exp\left[-\frac{m_j\omega_j}{\hbar} x_j^2 \tanh\left(\frac{\hbar\omega_j}{2kT}\right)\right] \tag{22}$$

The product extends to all normal modes of the molecule in the first electronic excited state, with k being the Boltzmann constant and x_j the normal coordinates, which can be converted back to Cartesian coordinates to evaluate the emission rate.

Having been made an introduction about the FC and NE methodologies, now we can discuss the computational strategies adopted in our calculations.

Computational Details. For the FC simulations we have used the Gaussian 09[23] program suite. To perform the emission spectra calculations using this software, it is necessary to provide first the normal mode (NM) analysis for the ground and excited states which, in turn, has to be preceded by full geometry optimizations. All these calculations were performed by means of density functional theory (DFT) and time-dependent density functional theory (TD-DFT) with the B3LYP, M062X, and ωB97XD functionals without symmetry constraints. These functionals were chosen because, in this analysis, equilibrium geometries, in particular dihedral angles, are an important factor that vary somewhat with each functional. Therefore, we chose functionals of three different types: the standard B3LYP, the long-range corrected ωB97XD and the meta-hybrid M062X. The basis set chosen was 6-31G*. It is worth mention here that the 6-31G* basis set is considered a medium size basis set in the modeling of excited state properties. Our goal here, though, is to investigate the effect of functional choice in FC and NE simulations as well as of the number of geometries sampled in NE simulations, which ranged from 50 to 5000. Due to this large quantity of geometries, we limited our investigation to the 6-31G* basis set to decrease the time consumed in each calculation. Nonetheless, larger basis set could be used to obtain a better description of the excited state properties.

The NE simulation was carried out using the software Newton-X,[24,25] which requires as input the optimized geometry of the initial state as well as its normal mode analysis. A number N of nonequilibrium geometries are produced and, for each geometry, a single point calculation is performed with TD-DFT to obtain the parameters used in eq 21. Here, Newton-X simulations are performed with $N = 50$, 500, and 5000 using the B3LYP, M062X, and ωB97XD functionals.

For both methods, the same parameters were chosen to isolate the effects of the method itself when comparisons were made. The temperature was set to zero and the refractive index was set to 1. Gaussian line shapes were used in all simulations with a phenomenological broadening of $\delta = 0.05$ eV. With respect to the computational time, the step that is most time-consuming is the optimization and frequency calculations of the excited state. Once optimizations and NM analyses are done for both states, the calculation of the spectrum is fast under the FC approximation, whereas in the NE method, the Newton-X software still requires N single point calculations to be

performed to complete the simulation of the emission spectrum. However, this inconvenience is mitigated by the fact that these calculations may be done in parallel, which expedites the procedure. Furthermore, it is worth mentioning here that the FC and NE calculations were performed using the set of rigid and flexible molecules represented in Figure 1.
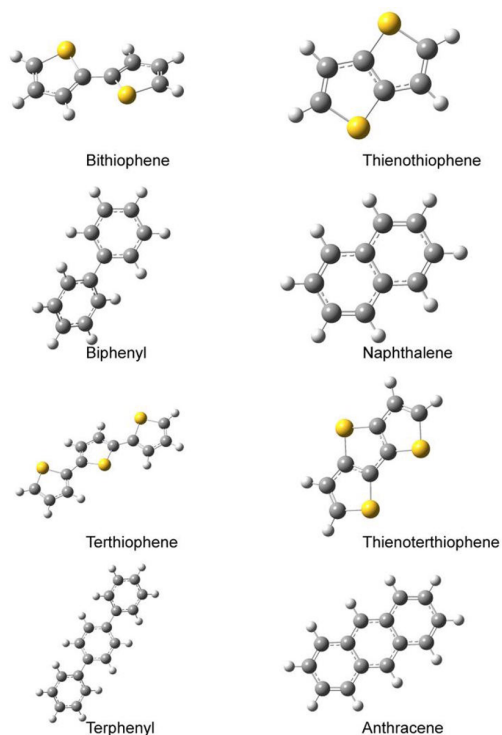
Figure 1. Flexible and rigid organic molecules used in the FC and NE simulations. In the color scheme, the carbon atoms are represented in gray, hydrogens in white, and sulfur atoms in yellow.

■ RESULTS AND DISCUSSIONS

As mentioned above, there is a negative relationship between changes in molecular geometry from the ground to excited state and the reliability of the FC results. Therefore, it becomes essential to identify a parameter that may provide a measurement for the quality of the simulated spectrum. This parameter is termed the spectrum progression and it is defined as

$$S = \sum_n |\langle \phi_{0n} | \phi_{10} \rangle|^2 \tag{23}$$

To verify the above-mentioned relationship, several FC simulations were performed for the molecules presented in Figure 1 to provide a fairly general physical picture. The S parameter, which in principle has infinite terms, can be calculated analytically, resulting in $S = 1$. Therefore, the closer the spectrum progression gets to 100%, the more reliable the simulation becomes. It means that, even though there are infinite vibrational states, if the simulation has taken into account a sufficient number of them, S will be close to 1.

In this way, Figure 2 presents the spectrum progression for the cases considering the molecules depicted in Figure 1 as a function of the parameter (D), which measures the molecular planarity. This parameter is defined as

$$D = \sum_k \theta_k \tag{24}$$

where θ_k is the angle between two rings. The summation extends to all pairwise combinations of rings. The choice of this parameter is justified due to the fact that the most relevant change in the molecular geometry is its planarity. From Figure 2 it is clear that molecules whose geometry does not change substantially from the ground to excited state (small ΔD) present spectrum progressions close to 100%. In other words, rigid molecules present spectrum progressions higher than the flexible ones. Besides, our results also point to the fact that the B3LYP (B) functional produces less variation in geometry and higher spectrum progression followed by M062X (M) and ωB97XD (W). The exceptions are the molecules composed of fused thiophene rings, which become less planar when going from the ground to the excited state. The most notable case is the one of thienothiophene (Figure 2). From these observations, it is possible to conclude that the number of rings is not a determinant factor in predicting spectrum progression because, for instance, terthiophene shows higher progression than bithiophene. Moreover, we can draw another general conclusion based on the results presented in Figure 2. For ΔD values higher than 20, it is possible to note that the spectrum progression presents a linear decaying for the functionals in the following order B-M-W (note that the greater ΔD is, the lower S is). It is also clear that B3LYP can produce small variations in the molecular geometry going from the ground to the excited structure in comparison with the other remaining functionals.

Because the FC approximation is not accurate enough to provide a reasonable description of the emission spectra for flexible molecules, the study of an alternate approach which can handle this problem properly is absolutely desirable. In this way, we now turn our discussions to the results obtained using the alternative strategy studied here. As mentioned before, the NE method relies on an average over a set of nuclear geometries. Therefore, we need to ascertain the dependence of the simulation with respect to the number of geometries sampled, i.e., the number N in eq 21. We chose to perform NE simulations only for the biphenyl, naphthalene, and bithiophene moieties. The reasons are their small size, which allows us to use a larger factor N than normally used, and the availability of experimental data, to perform comparisons.

Having explained the reasons for the particular choice of molecules used in our study, we can now present the effects of increasing the factor N in a NE simulation. In this way, Figure 3 shows a comparison of the emission spectra of NE simulations and experiment for the above-mentioned molecules. It is worth mentioning here that, at first, for $N = 50$, many peaks can be observed in the emission spectra for the set of molecules investigated here (Figure 1). These peaks tend to disappear as N increases and the spectrum approaches convergence. The NE method is capable of reproducing the envelope of the spectrum, but not vibronic progressions, with any visible structure usually being regarded as noise related to the stochastic nature of the method. It means that the greater the value of N is, the better the envelope description will be. In the cases studied here, we noticed, however, that the simulations performed with $N = 500$ may provide a better agreement with experiment, as shown in Figure 3. Nonetheless, when normalized, the simulations carried out using $N = 500$ and $N = 5000$ present a very similar agreement with the experimental data. Besides, for the
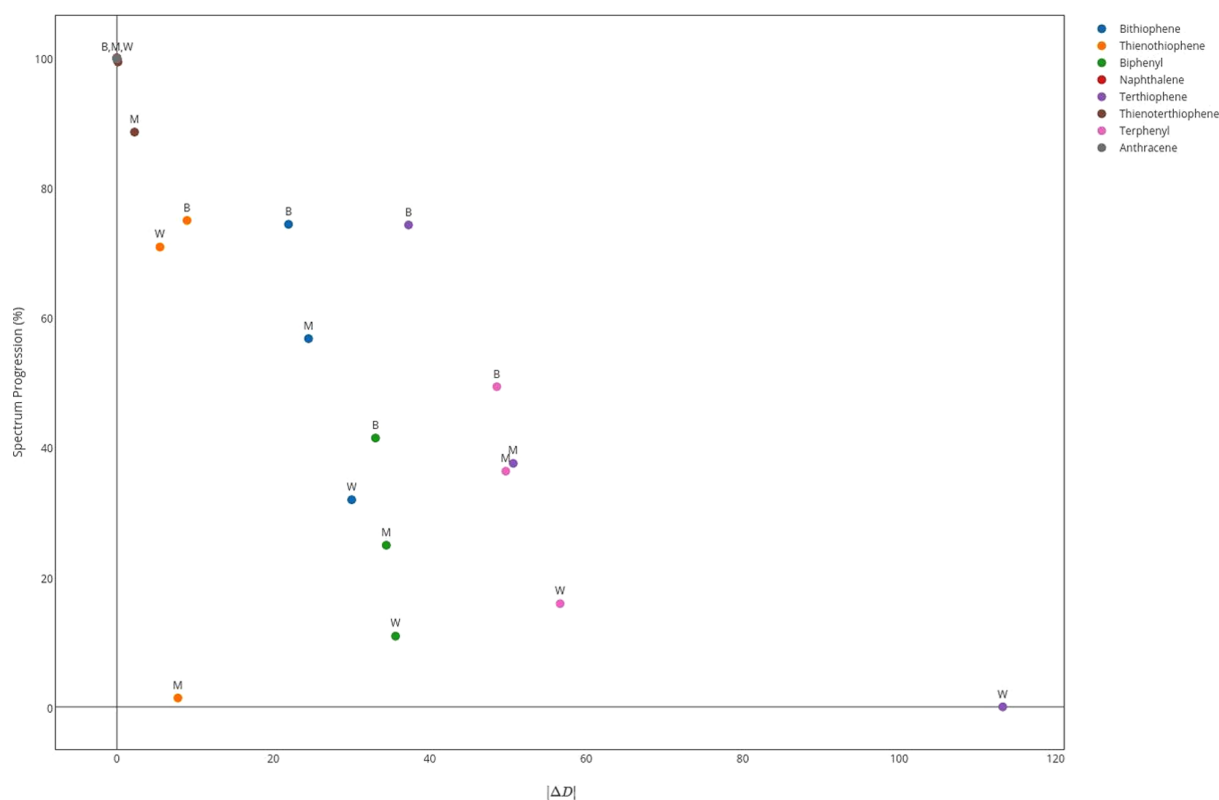
Figure 2. Spectrum progression for the set of rigid and flexible molecules depicted in Figure 1. (B), (M), and (W) represent the progressions computed using the B3LYP, M062X, and ωB97XD functionals, respectively.
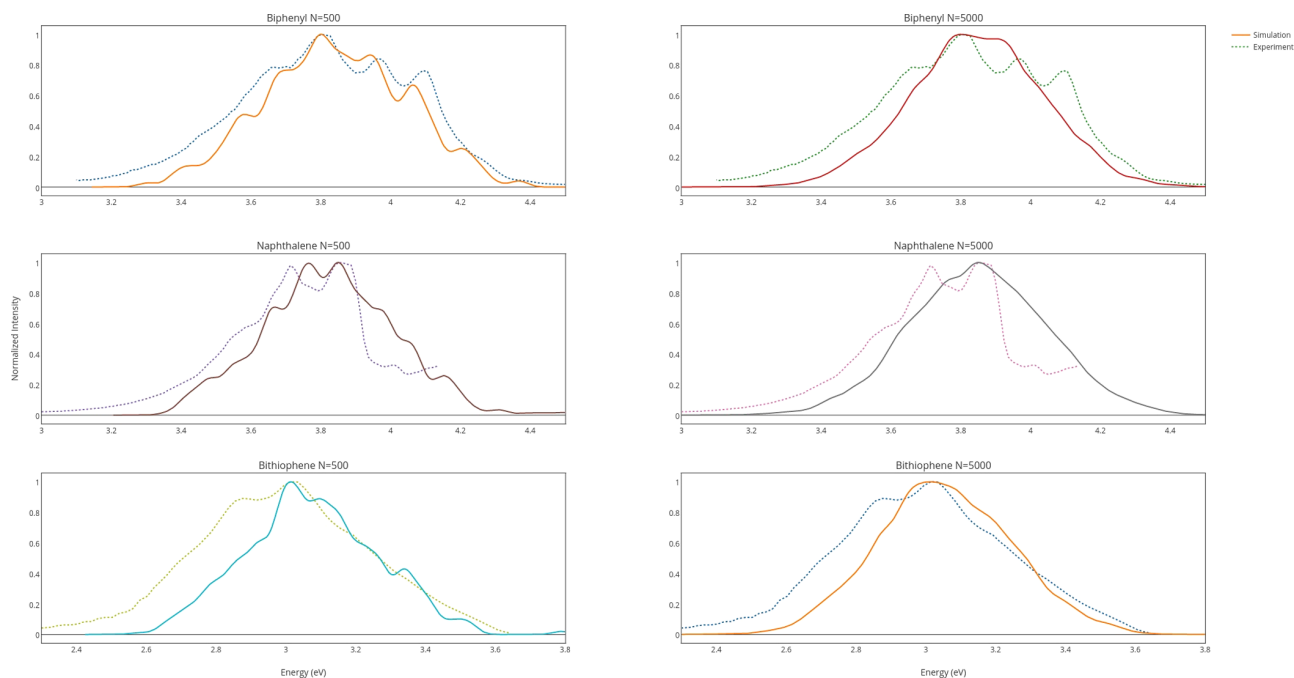
Figure 3. Comparison between the emission spectra of NE simulations done with B3LYP and experiment. Spectra were normalized and shifted so their maxima would match. From top to bottom: biphenyl, naphthalene, and bithiophene. On the left, NE simulations with $N = 500$ and on the right $N = 5000$. Experimental data are shown as dotted lines.

molecules investigated here, the spectrum envelopes for $N = 500$ and $N = 5000$ almost overlap, the difference being the peak structure that can be seem for $N = 500$ and which is absent for

$N = 5000$. Some of the peaks observed when using $N = 500$ cannot be mapped to those that appear in experiment, being indeed noise. This fact suggests that there may be an optimal
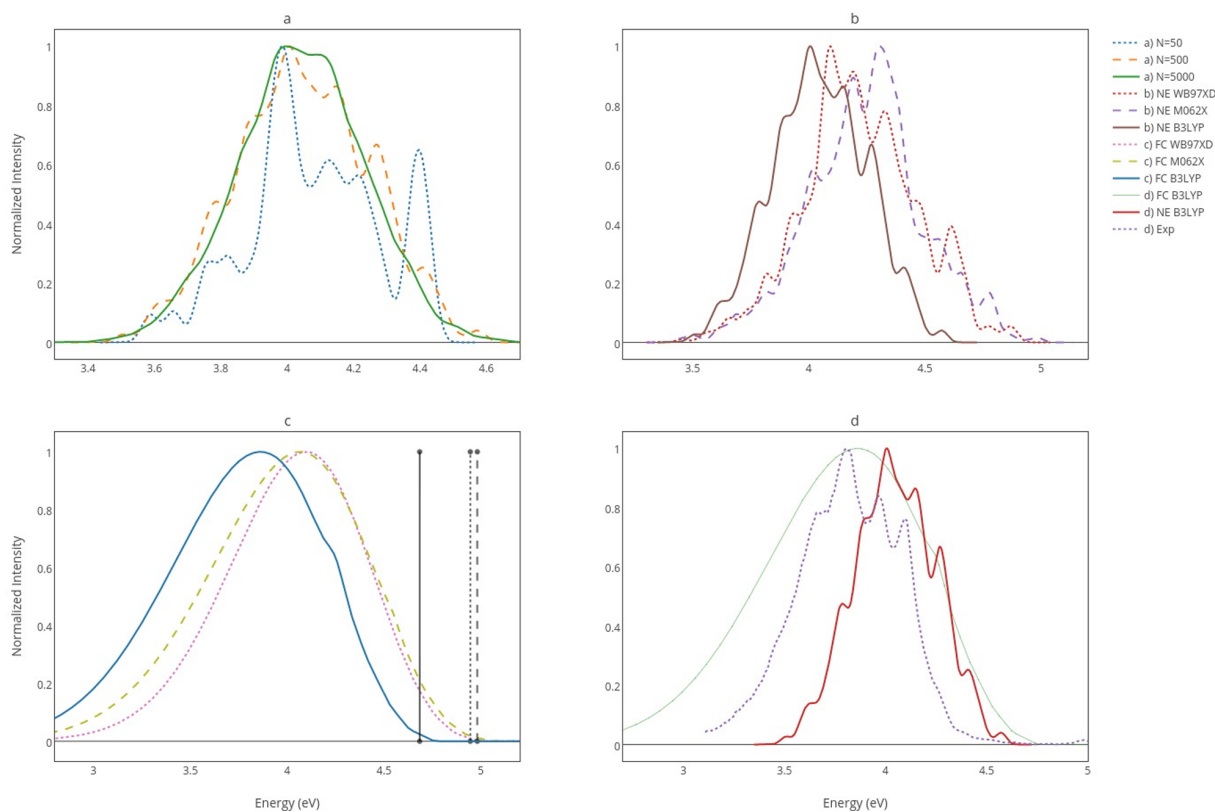
Figure 4. Biphenyl: (a) NE simulations for $N = 50$, 500, and 5000 done with B3LYP. (b) NE simulations with $N = 500$ using the B3LYP, M062X, and ωB97XD functionals. (c) FC simulations with B3LYP, M062X, and ωB97XD functionals. Vertical lines mark the 0−0 transitions. (d) Comparison between FC, NE, and experiments.

factor N that provides a good compromise between noise and information, allowing for a better theoretical description of the experimental results. However, even if this optimal point exists, one could argue that it would only be useful if one had an experimental spectrum beforehand with which to compare; i.e., it would be useless for making predictions, because one cannot tell information from noise only by analyzing the peaks of the simulated spectrum.

Now we analyze the emission spectra of each molecule presented in Figure 3 in detail. To do so, Figures 4, 5, and 6 show the results obtained from the FC and NE simulations along with the experimental data.[26,27] The simulated spectra of biphenyl is presented in Figure 4. The NE simulation using $N = 50$, presented in Figure 4a, clearly cannot describe accurately the spectrum. As the value of N increases, the fluctuations related to noise are reduced and the description of the envelope improves continuously as the spectrum centers around a single peak. In Figure 4b, we notice that the NE simulations performed with the B3LYP and ωB97XD functionals produce very similar shapes, the latter being slightly blue-shifted with respect to the former as the peaks are located respectively at 4.01 and 4.09 eV. The simulation carried out with M062X is even more blue-shifted, with the peak located at 4.31 eV. Moving on to Figure 4c, it is possible to note that the functionals M062X and ωB97XD produce very similar results using the FC approximation. The B3LYP simulation is red-shifted with respect to the M062X and ωB97XD ones, with the maximum located at 3.86, 4.07, and 4.10 eV, respectively. The vertical lines that state the energy of the 0−0 transition are substantially shifted to the right of the simulated spectra,

showing that the main contributions to the spectrum come from much higher modes. It is interesting also to analyze the comparison of NE and FC simulations to experiment, as shown in Figure 4d. In this figure it is shown the simulations that present better agreement with the experimental spectrum, both carried out with the B3LYP functional. The FC approximation managed to reproduce well the position of the experimental maximum (3.80 eV) but predicted a much broader spectrum. On the contrary, the NE simulation is blue-shifted with respect to experiment, but it is more accurate when it comes to the width of the spectrum as well as the structure of the peaks. Figure 5, in its turn, shows the simulations for naphthalene. For Figure 5a we can draw conclusions similar to those presented for Figure 4a. For this system, in particular, the shape of the envelope for $N = 50$ is almost similar to the ones obtained when higher N are taken into account. From Figure 5b it can be seen that NE simulations performed with M062X and ωB97XD functionals are fairly similar, with peaks at 4.37 and 4.21 eV, respectively. The spectra obtained with B3LYP simulation is red-shifted with respect to the other two, with a peak located at 3.84 eV. In Figure 5c we compare the results obtained in the scope of FC simulations. Once more, the M062X and ωB97XD spectra are blue-shifted with respect to B3LYP, with the maximum located at 4.76, 4.72, and 4.11 eV, respectively. We also note that both M062X and ωB97XD show only one peak in the spectrum, which is identified with the 0−0 transition, whereas B3LYP shows a two-peak structure that can also be observed in the experimental spectrum. The 0−0 transition is more relevant to naphthalene as it is a rigid molecule. The comparison with experiment is shown in Figure 5d. Here we
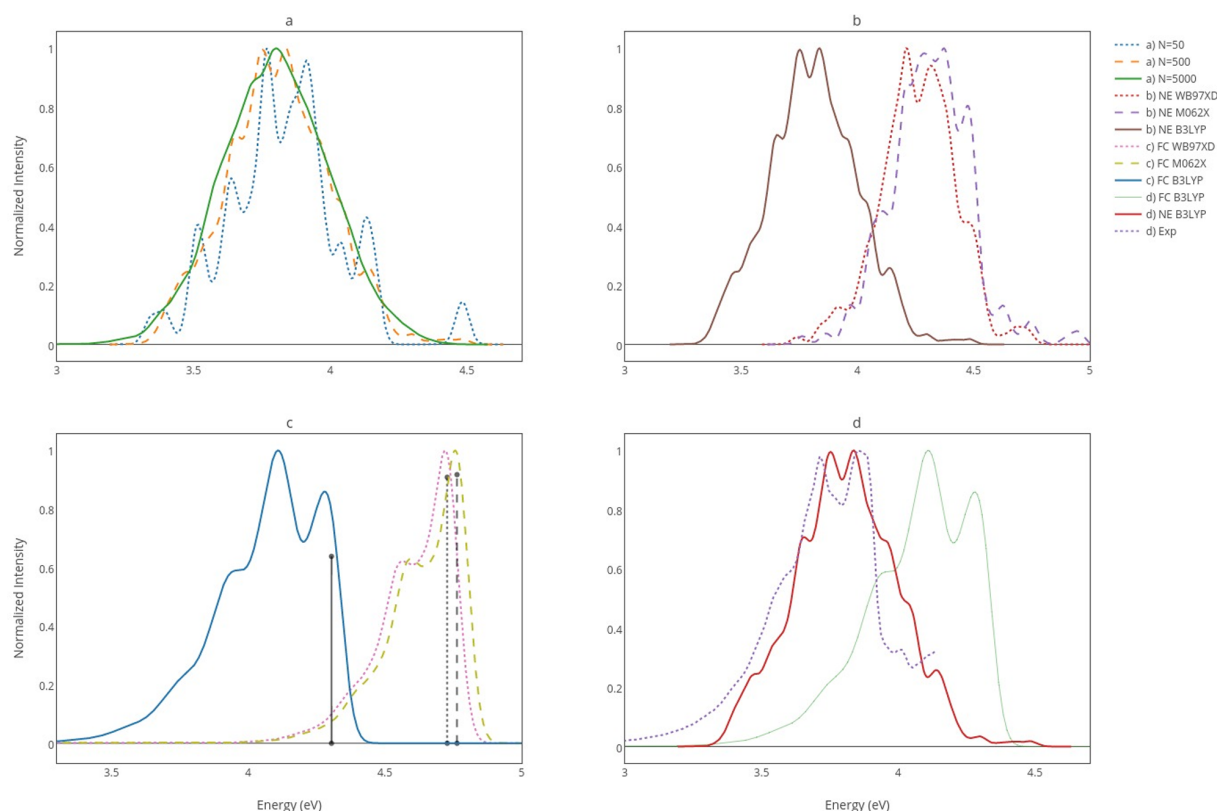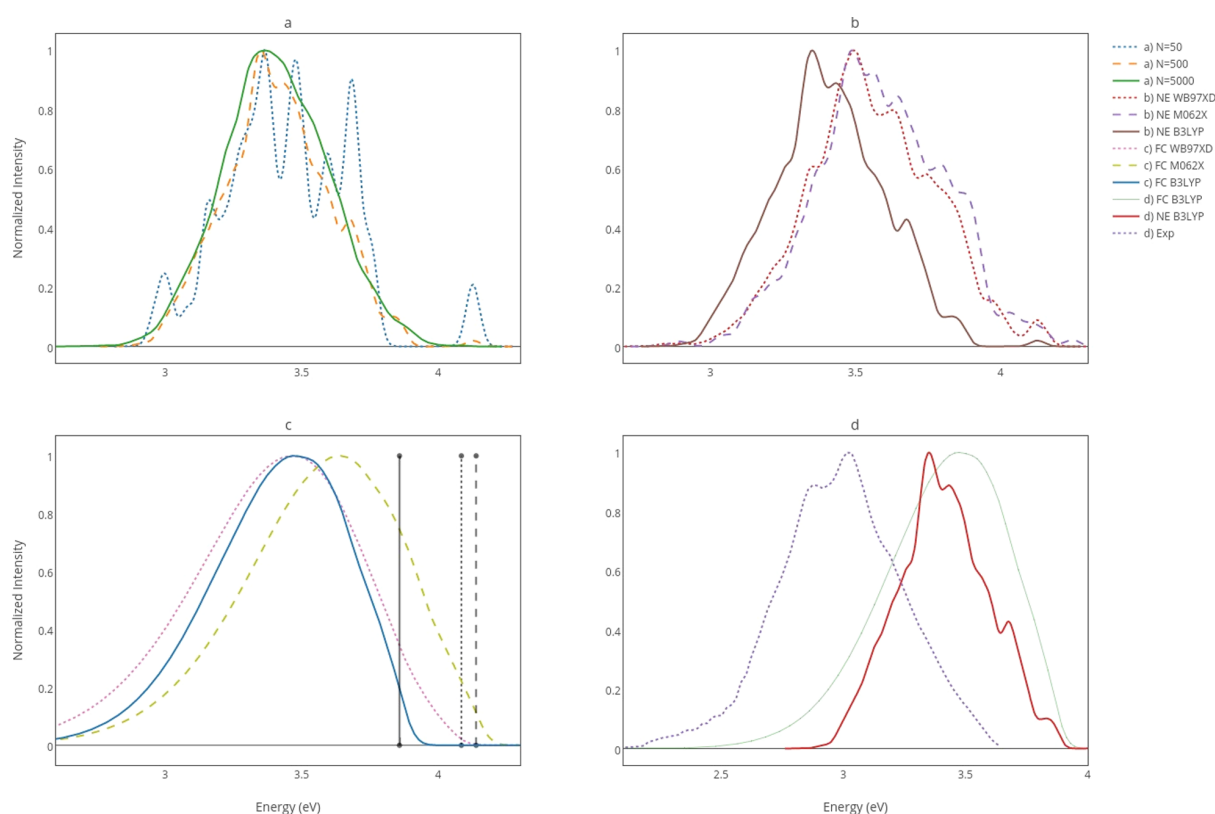
Figure 5. Naphthalene: (a) NE simulations for N = 50, 500, and 5000 done with B3LYP. (b) NE simulations with N = 500 using the B3LYP, M062X, and ωB97XD functionals. (c) FC simulations with B3LYP, M062X, and ωB97XD functionals. Vertical lines mark the 0−0 transitions. (d) Comparison between FC and NX methods with the experiment.

observe that the NE simulation is in good agreement with experiment but fails to reproduce the steepness in the high energy part of the spectrum. The FC simulation is blue-shifted and is also in good agreement with experiment, apart from the relative intensity of the second peak.

Finally, we discuss the results obtained for the emission spectra considering the bithiophene molecule presented in Figure 6. The results presented in Figure 6a can be understood as discussed above for the cases presented in Figures 4a and 5a. In Figure 6b, NE simulations performed with M062X and ωB97XD almost overlap completely, with peaks at 3.49 and 3.50 eV, respectively. The B3LYP simulation is red-shifted with respect to the others, but presenting a very similar shape. When it comes to the FC simulations (Figure 6c), B3LYP and ωB97XD functionals produce similar results, with the M062X simulation slightly blue-shifted with respect to the others. Peaks are located at 3.47, 3.47 and 3.64 eV, respectively. The flexible character of bithiophene results in peaks situated substantially to the left of the 0−0 transitions, again showing that transitions to higher vibrational states contribute the most to the spectrum. Lastly, from Figure 6d, it is possible to conclude that both simulations are blue-shifted with respect to experiment, which shows a peak at 3.01 eV. The FC simulation predicts a broader spectrum than the experimental one. In that regard we may conclude that the NE simulation better reproduces the experimental data.

CONCLUSIONS AND FINAL REMARKS

In summary, the emission spectra of small rigid and flexible organic molecules was theoretically investigated in the scope of Franck−Condon and nuclear ensemble methods, which treat vibrational contributions differently. The first uses vibrational wave functions to calculate overlap integrals, whereas the latter resorts to an average over an ensemble of nuclear geometries. Three molecules were selected to carry out this study: naphthalene, biphenyl, and bithiophene. They are all molecules of interest to applications in organic electronics, the first presenting a planar structure and the later two a twisted structure in the ground state. Our results show how the spectrum progression diminishes the more the geometry of the molecule changes from the ground to excited state. This fact leads to unreliable spectral simulations obtained using the Franck−Condon approximation. In this way, the results for the emission spectra obtained using the NE approach are more accurate as this methodology does not rely on the underlying assumption of no change in geometry between the two states. Indeed, we observed here that the simulations using the NE approach are in better agreement with experiment than the ones produced by FC calculations. Importantly, we have concluded that the description of a suitable balance between the vibronic progression and emission spectra envelope is substantially dependent on the initial sampling for the NE calculations. Analyzing the simulations for each molecule individually, we draw a fairly general conclusion that states that the nuclear ensemble simulations are more accurate than Franck−Condon counterparts in predicting the spectral

Figure 6. Bithiophene: (a) NE simulations for N = 50, 500, and 5000 done with B3LYP. (b) NE simulations with N = 500 using B3LYP, M062X, and ωB97XD functionals. (c) FC simulations with B3LYP, M062X and ωB97XD functionals. Vertical lines mark the 0−0 transitions. (d) Comparison between FC and NE simulations with experiment.

envelope. The Franck−Condon simulations produce only very broad spectra, except for naphthalene (particularly due to its rigidity), in which case it reproduces fairly well the experimental spectrum. Moreover, among the functionals used in the simulations presented here, the B3LYP better reproduced the experimental emission spectra.

■ **AUTHOR INFORMATION**

Corresponding Author

*D. A. da Silva Filho. E-mail: dasf@unb.br.

Notes

The authors declare no competing financial interest.

■ **REFERENCES**

(1) Kawashima, K.; Tamai, Y.; Ohkita, H.; Osaka, I.; Takimiya, K. High-Efficiency Polymer Solar Cells With Small Photon Energy Loss. *Nat. Commun.* **2015**, *6*, 10085.

(2) Kim, T.; Kim, J.-H.; Kang, T. E.; Lee, C.; Kang, H.; Shin, M.; Wang, C.; Ma, B.; Jeong, U.; Kim, T.-S.; et al. Flexible, Highly Efficient All-Polymer Solar Cells. *Nat. Commun.* **2015**, *6*, 8547.

(3) Liu, S.; Jiang, R.; You, P.; Zhu, X.; Wang, J.; Yan, F. Au/Ag Core-Shell Nanocuboids For High-Efficiency Organic Solar Cells With Broadband Plasmonic Enhancement. *Energy Environ. Sci.* **2016**, *9*, 898.

(4) Cui, C.; He, Z.; Wu, Y.; Cheng, X.; Wu, H.; Li, Y.; Cao, Y.; Wong, W.-Y. High-Performance Polymer Solar Cells Based On A 2D-Conjugated Polymer With An Alkylthio Side-Chain. *Energy Environ. Sci.* **2016**, *9*, 885.

(5) Jurow, M. J.; Mayr, C.; Schmidt, T. D.; Lampe, T.; Djurovich, P. I.; Brütting, W.; Thompson, M. E. Understanding And Predicting The Orientation Of Heteroleptic Phosphors In Organic Light-Emitting Materials. *Nat. Mater.* **2016**, *15*, 85−91.

(6) Lee, J.; Chen, H.-F.; Batagoda, T.; Coburn, C.; Djurovich, P. I.; Thompson, M. E.; Forrest, S. R. Deep Blue Phosphorescent Organic Light-Emitting Diodes With Very High Brightness And Efficiency. *Nat. Mater.* **2016**, *15*, 92−98.

(7) Thompson, B. C.; Fréceht, J. M. J. Polymer-Fullerene Composite Solar Cells. *Angew. Chem., Int. Ed.* **2008**, *47*, 58−77.

(8) Coropceanu, V.; Cornil, J.; da Silva Filho, D. A.; Olivier, Y.; Silbey, R.; Brédas, J.-L. Charge Transport In Organic Semiconductors. *Chem. Rev. (Washington, DC, U. S.)* **2007**, *107*, 926−952.

(9) Möller, S.; Forrest, S. R. Improved Light Out-Coupling In Organic Light Emitting Diodes Employing Ordered Microlens Arrays. *J. Appl. Phys. (Melville, NY, U. S.)* **2002**, *91*, 3324−3327.

(10) Jacquemin, D.; Perpete, E. A.; Ciofini, I.; Adamo, C. Accurate Simulation Of Optical Properties In Dyes. *Acc. Chem. Res.* **2009**, *42*, 326−334.

(11) Bernardi, F.; Olivucci, M.; Robb, M. A. Potential Energy Surface Crossings In Organic Photochemistry. *Chem. Soc. Rev.* **1996**, *25*, 321−328.

(12) Charaf-Eddin, A.; Planchat, A.; Mennucci, B.; Adamo, C.; Jacquemin, D. Choosing A Functional For Computing Absorption And Fluorescence Band Shapes With TD-DFT. *J. Chem. Theory Comput.* **2013**, *9*, 2749−2760.

(13) Cerezo, J.; Ferrer, F. J. A.; Prampolini, G.; Santoro, F. Modeling Solvent Broadening On The Vibronic Spectra Of A Series Of Coumarin Dyes. From Implicit To Explicit Solvent Models. *J. Chem. Theory Comput.* **2015**, *11*, 5810−5825.

(14) Jacquemin, D.; Duchemin, I.; Blase, X. 0−0 Energies Using Hybrid Schemes: Benchmarks Of TD-DFT, CIS(D), ADC(2), CC2, And BSE/GW Formalisms For 80 Real-Life Compounds. *J. Chem. Theory Comput.* **2015**, *11*, 5340−5359.

(15) Lumpi, D.; Horkel, E.; Plasser, F.; Lischka, H.; Frohlich, J. Synthesis, Spectroscopy, And Computational Analysis Of Photo-luminescent Bis(Aminophenyl)-Substituted Thiophene Derivatives. *ChemPhysChem* **2013**, *14*, 1016−1024.

(16) Barbatti, M.; Aquino, A. J. A.; Lischka, H. The UV Absorption Of Nucleobases: Semi-Classical Ab Initio Spectra Simulations. *Phys. Chem. Chem. Phys.* **2010**, *12*, 4959−4967.

(17) Crespo-Otero, R.; Barbatti, M. Spectrum Simulation And Decomposition With Nuclear Ensemble: Formal Derivation And Application To Benzene, Furan And 2-Phenylfuran. *Theor. Chem. Acc.* **2012**, *131*, 2−14.

(18) Barone, V.; Bloino, J.; Biczysko, M.; Santoro, F. Fully Integrated Approach To Compute Vibrationally Resolved Optical Spectra: From Small Molecules To Macrosystems. *J. Chem. Theory Comput.* **2009**, *5*, 540−554.

(19) Niu, Y.; Peng, Q.; Deng, C.; Shuai, X. G. Z. Theory Of Excited State Decays And Optical Spectra: Application To Polyatomic Molecules. *J. Phys. Chem. A* **2010**, *114*, 7817−7831.

(20) Heller, E. J. Quantum Corrections To Classical Photo-dissociation Models. *J. Chem. Phys.* **1978**, *68*, 2066−2075.

(21) Bergsma, J. P.; Berens, P. H.; Wilson, K. R.; Fredkin, D. R.; Heller, E. J. Electronic Spectra From Molecular Dynamics: A Simple Approach. *J. Phys. Chem.* **1984**, *88*, 612−619.

(22) Feynman, R. *Statistical Mechanics: A Set Of Lectures*; Advanced Books Classics Series: Westview Press: Boulder, CO, 1998.

(23) Frisch, M. J.; Trucks, G. W.; Schlegel, H. B.; Scuseria, G. E.; Robb, M. A.; Cheeseman, J. R.; Scalmani, G.; Barone, V.; Mennucci, B.; Petersson, G. A.; et al. *Gaussian 09* Revision B.01; Gaussian Inc.: Wallingford, CT, 2009.

(24) Barbatti, M.; Ruckenbauer, M.; Plasser, F.; Pittner, J.; Granucci, G.; Persico, M.; Lischka, H. ewton-X: A Surface-Hopping Program For Nonadiabatic Molecular Dynamics. *Wiley Interdiscip. Rev.: Comput. Mol. Sci.* **2014**, *4*, 26−33.

(25) Barbatti, M.; Ruckenbauer, M.; Plasser, F.; Pittner, J.; Granucci, G.; Persico, M.; Lischka, H. The On-The-Fly Surface-Hopping Program System Newton-X: Application To Ab Initio Simulation Of The Nonadiabatic Photodynamics Of Benchmark Systems. *J. Photochem. Photobiol., A* **2007**, *190*, 228−240.

(26) Gombojav, B.; Namsrai, N.; Yoshinari, T.; Nagasaka, S.-i.; Itoh, H.; Koyama, K. Fluorescence Spectra Of Bithiophene And Terthiophene Single Crystals And Of Their Isolated Molecules In Cyclodextrin. *J. Solid State Chem.* **2004**, *177*, 2827−2832.

(27) Du, H.; Fuh, R. A.; Li, J.; Corkan, A.; Lindsey, J. S. PhotochemCAD: A Computer-Aided Design And Research Tool In Photochemistry. *Photochem. Photobiol.* **1998**, *68*, 141−142.

Article 2

CrossMark

ORIGINAL PAPER

A joint theoretical and experimental characterization of two acene-thiophene derivatives

Leonardo Evaristo de Sousa[1] · Arthur Akira Mamiya[1] · Jakob Kjelstrup-Hansen[2] ·
Demétrio Antônio da Silva Filho[1]

Abstract Acene-thiophenes compounds have been used successfully as active materials in thin-film transistors and photodetectors. This work aims at obtaining an adequate theoretical framework to accurately characterize the optical and electronic properties of two such compounds: NaT2 and NaT3. This is done by comparing the results of simulations with experimental absorption spectra. Basis size effects are investigated as well as the role of intramolecular vibrations in the simulated spectra. It is shown that the most important feature of a DFT calculation is the appropriate selection of long-range corrected functionals, which allows for the accurate description of the first absorption band of these molecules.

Keywords TD-DFT · DFT · UV–Vis spectrum simulations · Acene-thiophenes

Introduction

Oligoacenes and oligothiophenes are two of the most studied classes of compounds for applications in organic

---

This paper belongs to Topical Collection VI Symposium on Electronic Structure and Molecular Dynamics – VI SeedMol

✉ Demétrio Antônio da Silva Filho
dasf@unb.br

1 Institute of Physics, University of Brasília, 70.919-970, Brasília, Brazil

2 NanoSYD, Mads Clausen Institute, University of Southern Denmark, Sønderborg, Denmark

electronics, both theoretically [1–4] and also experimentally [5–8]. However, these two classes of molecules have shortfalls that hinder their successful use in commercial applications. Pentacene, for example, reacts with oxygen in the presence of light, directly impacting the device's performance [9].

In the search for new organic molecules that can both lead to high device performance and high environmental stability, oligoacenes have been combined with oligothiophenes originating a new class of organic semiconductors. This new class of molecules displays interesting properties such as high thermal stability and high melting point, allowing the resulting molecules to be sublimed to form high-quality films to be used as thin-film transistors (TFTs) [10] or highly sensitive photodetectors [11].

Motivated by these interesting experimental results, we show here a comprehensive theoretical study for two of these molecules, 5,5′-bis(naphth-2-yl)- 2,2′-bithiophene and 5,5″-bis(naphth-2-yl)-2,2′:5′,2″-terthiophene, hereafter termed simply NaT2 and NaT3, respectively. These two molecules are shown in Fig. 1. They were first reported by Tian et al. [12]. In this work, density functional theory (DFT) and time-dependent density functional theory (TD-DFT) were used to characterize both the electronic structure and the spectroscopic properties—absorption in the UV–Vis—of these two molecules. Three functionals with different characteristics were employed in the calculations and the effect of diffusion functions in the basis set was studied as well as the impact of using the Tamm–Dancoff approximation (TDA) in place of regular TD-DFT. The nuclear ensemble method (NE) was also used to produce absorption spectra that take contributions from vibrations into account. Theoretical results were compared to experimental data in order to identify the best way to perform a characterization of this class of molecules.
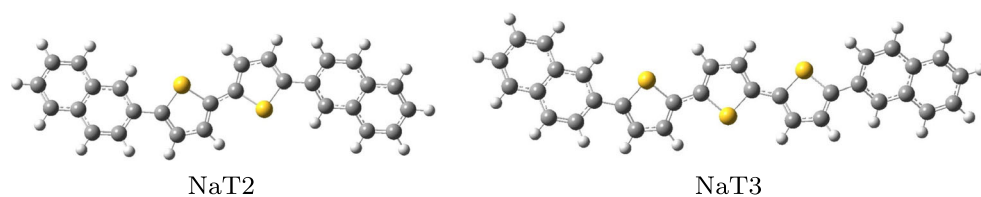
Fig. 1 Acene-thiophene
compounds studied in this work

NaT2   NaT3

Methods

Experimental details

Thin films of NaT2 [13] and NaT3 [14], respectively, were
prepared by vacuum sublimation onto BK7 glass substrates.
The film thicknesses for NaT2 [NaT3] were 152 nm [46
nm]. The absorption spectra for NaT2 [NaT3] was mea-
sured with a Shimadzu UV-2700 [PerkinElmer Lambda
900] spectrophotometer.

Computational details

Full geometry optimizations were performed for both
molecules with DFT. These were followed by frequency
calculations done to confirm that the optimized structures
corresponded indeed to minima of the potential energy sur-
faces. After that, TD-DFT calculations for several excited
states were performed in order to obtain transition energies
as well as the oscillator strengths, which provide infor-
mation about the relevant electronic transitions and the
absorption spectra. Finally, the role of intramolecular vibra-
tions in the absorption spectra was also taken into account
by means of the nuclear ensemble (NE) method [15].

For all the aforementioned calculations, the functionals
chosen were B3LYP [16], CAM-B3LYP [17] and ωB97XD
[18]. For most cases, the 6-31G(d,p) basis set was used,
however, the 6-31++G(d,p) basis set with diffuse functions
was also tested. The Tamm–Dancoff approximation was
tested as well to ascertain its performance in comparison
to regular TD-DFT calculations. These calculations were
performed with the Gaussian 09 [19] program suite.

The spectrum simulations done with the NE method
were performed with the Newton-X [20] software using ten
excited states for NaT2 and eight for NaT3. This relatively
small number is the result of a compromise between com-
putational cost and accuracy. The number of geometries
sampled was set to 500 in all cases. A broadening factor of
0.05 eV was applied throughout.

Results and discussions

NaT2

Figure 2 presents simulations performed under several
conditions. First, Fig. 2a shows results of TD-DFT cal-
culations done with 30 excited states with the 6-31G(d,p)

Fig. 2 Simulated absorption
spectrum of NaT2. From *top to
bottom*: **a** TD-DFT spectra
performed with B3LYP,
CAM-B3LYP, and ωB97XD
functionals. **b** Comparison
between ωB97XD spectra
calculated with and without
diffuse functions and TD/TDA.
c Comparison between
experimental spectrum,
ωB97XD TD-DFT simulation,
and ωB97XD NE simulation
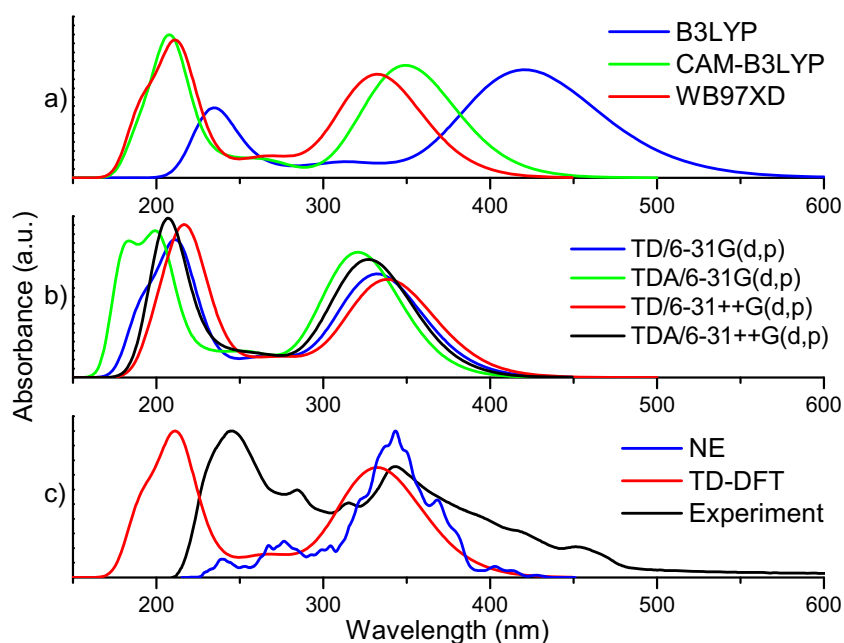
Table 1 NaT2 transition energies and oscillator strengths calculated with B3LYP, CAM-B3LYP, and ωB97XD for the first five excited states

Excited state	Transition energies and oscillator strengths					
	B3LYP		CAM-B3LYP		ωB97XD	
1	421 nm	1.4885	349 nm	1.5490	333 nm	1.4208
2	359 nm	0.0000	286 nm	0.0017	281 nm	0.0615
3	340 nm	0.0120	283 nm	0.0026	278 nm	0.0052
4	333 nm	0.0033	281 nm	0.0019	277 nm	0.0323
5	317 nm	0.1840	265 nm	0.2218	263 nm	0.2163

basis set and three different functionals. B3LYP predicts a severely red-shifted spectrum with respect to experiment. While experimentally we find a peak at 245 nm with a broad shoulder around 343 nm, this latter excitation is placed by B3LYP at around 420 nm. Such a poor result indicates the inadequacy of B3LYP in describing the NaT2 molecule. To attempt an improvement in the description, two other functionals were considered, first including long-range corrections—with CAM-B3LYP—and then including both long-range corrections and dispersion—with ωB97XD. It can be noticed that the inclusion of long-range corrections improves the results considerably. CAM-B3LYP predicts a peak in the spectrum around 350 nm, a shift of 70 nm in comparison to its non-corrected counterpart. Inclusion of dispersion does not produce significant changes. The ωB97XD functional shows a spectrum with a peak near 330 nm, slightly blue-shifted with respect to the CAM-B3LYP result. Both long-range corrected functionals show a higher energy peak on the 210-nm mark, a 15-nm blue shift with respect to experiment.

Table 1 summarizes the results obtained from these calculations for the first five excited states for each functional. The first excited state is predicted to be the most relevant transition in all cases followed by the fifth. Very similar oscillator strengths are predicted by each functional, but the transition energies differ significantly, as was observed in the spectra. This difference is a reflection of how each functional characterizes the first excited state. For B3LYP, it is mainly a HOMO to LUMO transition, whereas CAM-B3LYP also includes contributions from the HOMO-1 to LUMO+1 and ωB97XD includes HOMO-1 to LUMO+1 and HOMO to LUMO+2. These orbitals are shown in Fig. 3, from which we can determine that this transition is mainly $\pi - \pi*$. The additional excitations composing this transition show a small charge displacement from the thiophene fragment towards the acene fragments.

Given the results above, in order to attempt an increase in accuracy, the calculations were repeated using ωB97XD along with a larger basis set including diffuse functions, namely 6-31G++(d,p). The TDA approximation was also tested. Figure 2b shows the results.

It can be seen that the inclusion of diffusion functions slightly red shifts the spectrum both when regular TD-DFT is used and when TDA is applied. The fact that the choice of a larger basis set produces no relevant change in the results goes to show that the 6-31G(d,p) basis set is already enough for the purposes of describing the NaT2 system.

Comparison between the spectra obtained with regular TD-DFT and TDA shows that the latter are blue shifted with respect to the former regardless of the basis set

Fig. 3 NaT2 frontier orbitals calculated with wB97XD functional. Calculations with B3LYP and CAM-B3LYP wield similar orbitals

HOMO-1

HOMO

LUMO

LUMO+1

LUMO+2
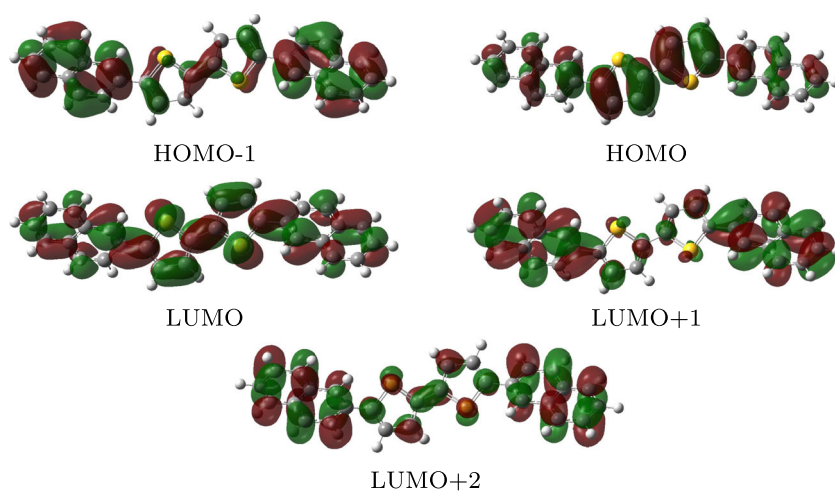
Fig. 4 Simulated absorption spectrum of NaT3. From *top to bottom*: **a** TD-DFT spectra performed with B3LYP, CAM-B3LYP and ωB97XD functionals. **b** Comparison between ωB97XD spectra calculated with and without diffuse functions and TD/TDA. **c** Comparison between experimental spectrum, ωB97XD TD-DFT simulation and ωB97XD NE simulation
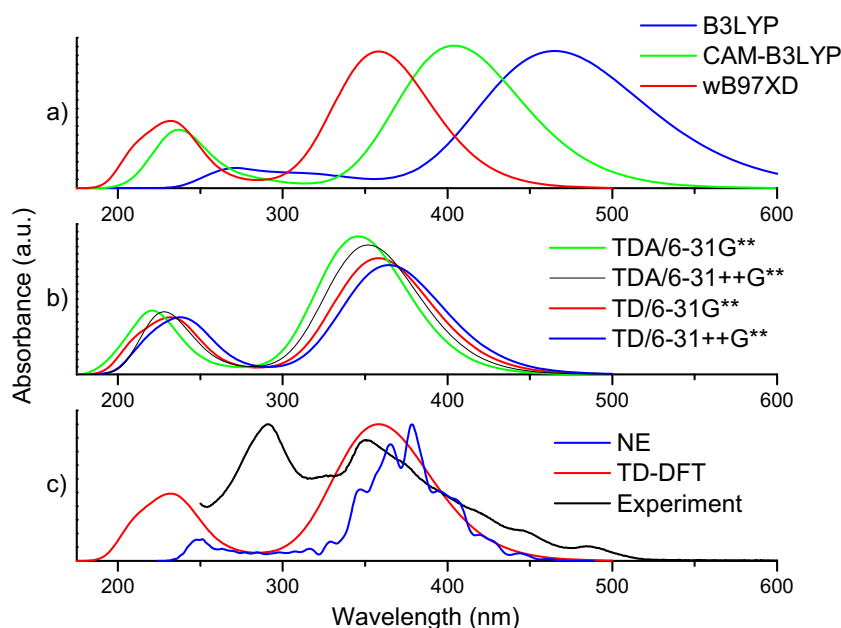
employed. They also show slightly higher values of the oscillator strength for the first electronic transition. Curiously, the TDA/ωB97XD/6-31G(d,P) combination shows a double peak in the blue region of the spectrum, a feature that is absent in all other calculations and in the experimental data.

So far, our theoretical spectra have been generated by broadening the theoretical stick transitions with Gaussian functions with half-width at half height equal to 0.33 eV. Our previous simulations of UV–Vis spectra of acenes and thiophenes show that further improvement of the theoretical description can be made by taking into account the intramolecular vibrations [21]. We then carried out the simulation of absorption spectra by using the nuclear ensemble method as implemented in the Newton-X program suite [20].

Figure 2c presents the comparison between experiment, the TD-DFT, and the NE method simulations. These were performed with ωB97XD/6-31G(d,p). Since the NE simulation took into account only ten excited states, it managed to describe well only the first absorption band. For this first band, both simulations show similar results. The NE method predicts an absorption peak at 343 nm, exactly the experimental value. This method takes an average over the contributions from hundreds of different molecular conformations, resulting in a slightly red-shifted spectrum with respect to the TD-DFT calculation performed in the optimized structure. This allows for a more realistic simulation, but is computationally more expensive. The single-point TD-DFT calculation fails to predict correctly the position of the more energetic band, but the relative intensities between peaks is in perfect agreement with the experiment.

Fig. 5 NaT3 frontier orbitals calculated with wB97XD functional. Calculations with B3LYP and CAM-B3LYP wield similar orbitals

HOMO-1   HOMO

LUMO   LUMO+1

LUMO+2
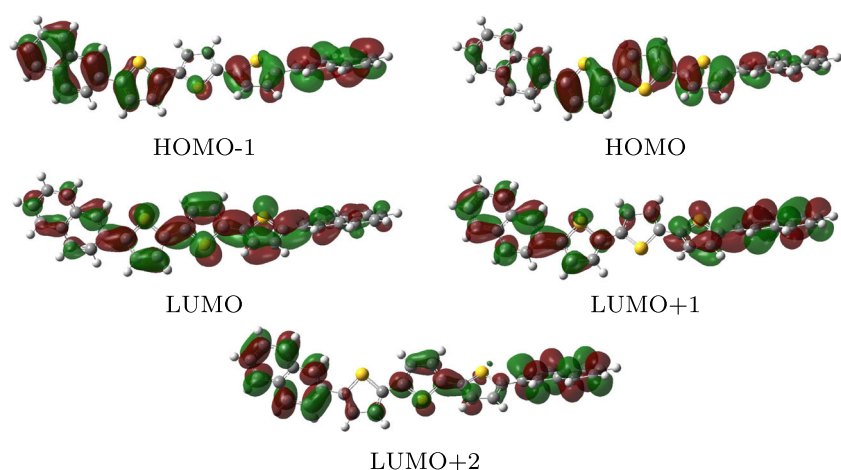
Table 2 NaT3 transition energies and oscillator strengths calculated with B3LYP, CAM-B3LYP, and ωB97XD for eight excited states

Excited state	Transition energies and oscillator strengths					
	B3LYP		CAM-B3LYP		ωB97XD	
1	465 nm	1.9135	404 nm	1.9896	358 nm	1.9068
2	387 nm	0.0011	314 nm	0.0198	296 nm	0.0548
3	358 nm	0.0049	292 nm	0.0018	280 nm	0.0013
4	355 nm	0.0215	291 nm	0.0035	279 nm	0.0018
5	337 nm	0.0067	281 nm	0.0974	272 nm	0.0340
6	333 nm	0.0665	277 nm	0.0008	259 nm	0.0522
7	313 nm	0.0031	265 nm	0.0084	248 nm	0.0003
8	308 nm	0.0838	252 nm	0.2057	240 nm	0.4705

NaT3

Applying to the NaT3 molecule, the same procedure as outlined before, the results presented in Fig. 4 are obtained.

Looking at Fig. 4a, it can be seen that the same trend is again present in the results for the TD-DFT calculations of the NaT3 molecule, which took into consideration 20 excited states. By going from B3LYP to CAM-B3LYP to ωB97XD, the energy of the first excited state steadily increases, not only by the re-evaluation of the HOMO/LUMO energies but also as more transitions apart from HOMO to LUMO become relevant. CAM-B3LYP includes the HOMO-1 to LUMO+1 transition and ωB97XD includes both HOMO-1 to LUMO+1 and HOMO to LUMO+2. These orbitals can be seen in Fig. 5. The orbitals and transitions forming this state are analogous to those of NaT2.

Transition energies and oscillator strengths for the eight first excited states of NaT3 are shown in Table 2. This table reveals that oscillator strengths for the first excited state are very similar for all functionals. Apart from this first transition, the second most relevant one is by far the eighth. In this case, the oscillator strengths increases as long-range corrections and dispersion effects are taken into account.

By analyzing how the less energetic peak progresses as the functional changes, it can be noticed that, in comparison to the NaT2 results, there is a more significant difference between the spectra obtained from CAM-B3LYP and ωB97XD, indicating that dispersion effects are more relevant in this case. The same cannot be said about the most energetic peak, which is similarly predicted by both functionals but absent in the B3LYP calculations.

Moving on to Fig. 4b, the same behavior is observed when comparing to Fig. 2b. The inclusion of diffusion functions produces a slight red shift in the spectrum, whereas the application of TDA results in a small blue shift with respect to the spectra calculated with regular TD-DFT. These results

indicate again that basis set effects are not the determinant factor in the quality of these simulations.

Finally, Fig. 4c shows the comparison between the experimental data and the ωB97XD TD-DFT and NE simulations. In this case, the NE method was used considering eight excited states, so as to take into account the transitions most relevant to the first absorption band. The results show good agreement on the position of this band. The same cannot be said about the most energetic peak, which shows a very much-inferior relative intensity with respect to the other peak than shown in the experimental data. The NE method simulation is also red shifted with respect to the TD-DFT ωB97XD spectrum much in the same way as it was in the case of NaT2. Neither simulation was able to reproduce correctly nor the relative intensity between peaks nor their separation. The single-point TD-DFT calculation predicts an absorption band in the 232-nm mark, a blue shift of 58 nm with respect to experiment. It is clear, however, that at least when it comes to the first absorption band, the ωB97XD/6-31G(d,p) combination has proven to be adequate. The red most experimental peaks lies at 353 nm, whereas the TD-DFT simulation marks it at 358 nm and the NE method at 378 nm. These results show that the difficulty in describing the spectrum of this molecule does not arise from the consideration of a single optimized geometry.

Conclusions

This work was aimed at performing a theoretical description of optical and electronic properties of two acene-thiophene compounds, NaT2 and NaT3. Several levels of theory and approximations were tested, leading to the following conclusions. First, it was observed that the 6-31G(d,p) basis set is enough for a proper theoretical characterization of the molecules under study, rendering the inclusion of diffusion functions superfluous. When it comes to the choice of

functional, it became evident that the inclusion of long-range corrections was an important feature. The more energetic band that is present in the spectra of both molecules is consistently described with a large blue shift. Dispersion effects are more relevant in the case of NaT3, a larger molecule than NaT2. All in all, the ωB97XD seems to be the best choice of functional among the tested ones. Comparison between the TDA method and regular TD-DFT showed no significant difference and plays no major part in the description. On the other hand, the use of the NE method produced spectra that described very well the first absorption band of both molecules. The consideration of hundreds of molecular conformations produced spectra that were less broad and red shifted with respect to their single point TD-DFT counterparts. These results pave the way for more studies involving these compounds and their applications in organic electronics.

References

1. da Silva Filho DA, Coropceanu V, Fichou D, Gruhn NE, Bill TG, Gierschner J, Cornil J, Brédas JL (2007) Hole-vibronic coupling in oligothiophenes: impact of backbone torsional flexibility on relaxation energies. Philos Trans R Soc Lond A: Mathematical, Physical and Engineering Sciences 365(1855):1435–1452. The Royal Society

2. Brédas JL, Calbert JP, da Silva Filho DA, Cornil J (2002) Organic semiconductors: a theoretical characterization of the basic parameters governing charge transport. Proc Natl Acad Sci USA 99(9):5804–5809. doi:10.1073/pnas.092143399

3. Gruhn NE, Da Silva Filho DA, Bill TG, Malagoli M, Coropceanu V, Kahn A, Brédas JL (2002) The vibrational reorganization energy in pentacene: molecular influences on charge transport. J Am Chem Soc 124:7918–7919. doi:10.1021/ja0175892

4. Kang JH, Da Silva Filho D, Bredas JL, Zhu XY (2005) Shallow trap states in pentacene thin films from molecular sliding. Appl Phys Lett 86(15):1–3

5. Facchetti A, Mushrush M, Katz HE, Marks TJ (2003) *n*-type building blocks for organic electronics: a homologous family of fluorocarbon-substituted thiophene oligomers with high carrier mobility. Adv Mater 15(1):33–38. doi:10.1002/adma.200390003

6. Hong XM, Katz HE, Lovinger AJ, Wang BC, Raghavachari K (2001) Thiophene-phenylene and thiophene-thiazole oligomeric semiconductors with high field-effect transistor on/off ratios. Chem Mater 13(12):4686–4691. doi:10.1021/cm010496z

7. Katz HE (1997) Organic molecular solids as thin film transistor semiconductors. J Mater Chem 7(3):369–376. doi:10.1039/a605274f

8. Katz HE, Bao Z, Gilat SL (2001) Synthetic chemistry for ultra-pure, processable, and high-mobility organic transistor semiconductors. Acc Chem Res 34(5):359–369

9. Maliakal A, Raghavachari K, Katz H, Chandross E, Siegrist T (2004) Photochemical stability of pentacene and a substituted pentacene in solution and in thin films. Chem Mater 16(24):4980–4986. ACS Publications

10. Merlo JA, Newman CR, Gerlach CP, Kelley TW, Muyres DV, Fritz SE, Toney MF, Frisbie CD (2005) P-channel organic semiconductors based on hybrid acene-thiophene molecules for thin-film transistor applications. J Am Chem Soc 127(11):3997–4009. doi:10.1021/ja044078h

11. Liu X, Tavares L, Osadnik A, Lausen JL, Kongsted J, Lützen A, Rubahn HG, Kjelstrup-Hansen J (2014) Low-voltage organic phototransistors based on naphthyl end-capped oligothiophene nanofibers. Org Electron 15(6):1273–1281

12. Tian H, Shi J, He B, Hu N, Dong S, Yan D, Zhang J, Geng Y, Wang F (2007) Naphthyl and thionaphthyl end-capped oligothiophenes as organic semiconductors: effect of chain length and end-capping groups. Adv Funct Mater 17(12):1940–1951

13. Liu X, Wallmann I, Boudinov H, Kjelstrup-Hansen J, Schiek M, Lützen A, Rubahn HG (2010) Ac-biased organic light-emitting field-effect transistors from naphthyl end-capped oligothiophenes. Org Electron 11(6):1096–1102

14. Balzer F, Schiek M, Osadnik A, Wallmann I, Parisi J, Rubahn HG, Lützen A (2014) Substrate steered crystallization of naphthyl end-capped oligothiophenes into nanofibers: the influence of methoxy-functionalization. Phys Chem Chem Phys 16(12):5747–5754

15. Crespo-Otero R, Barbatti M (2012) Spectrum simulation and decomposition with nuclear ensemble: formal derivation and application to benzene, furan and 2-phenylfuran. Theor Chem Accounts 131(6):1–14

16. Becke AD (1993) Density-functional thermochemistry. III. The role of exact exchange. J Chem Phys 98(7):5648–5652

17. Yanai T, Tew DP, Handy NC (2004) A new hybrid exchange–correlation functional using the coulomb-attenuating method (cam-b3lyp). Chem Phys Lett 393(1):51–57

18. Chai JD, Head-Gordon M (2008) Long-range corrected hybrid density functionals with damped atom–atom dispersion corrections. Phys Chem Chem Phys 10(44):6615–6620

19. Frisch MJ, Trucks GW, Schlegel HB, Scuseria GE, Robb MA, Cheeseman JR, Scalmani G, Barone V, Mennucci B, et al. (2010) G.A.P.: Gaussian 09 revision d.01. Gaussian, Inc., Wallingford CT

20. Barbatti M, Ruckenbauer M, Plasser F, Pittner J, Granucci G, Persico M, Lischka H (2014) Newton-x: a surface-hopping program for nonadiabatic molecular dynamics. Wiley Interdiscip Rev Comput Mol Sci 4(1):26–33

21. de Sousa LE, Ribeiro LA, Fonseca ALdA, da Silva Filho DA (2016) Modeling the Emission Spectra of Organic Molecules: A Competition between Franck–Condon and Nuclear Ensemble Methods. J Phys Chem A 120(27):5380–5388. ACS Publications

Article 3

Research paper

Mobility field and mobility temperature dependence in $PC_{61}BM$: A kinetic Monte-Carlo study

Leonardo Sousa [a], Riccardo Volpi [b], Demétrio Antônio da Silva Filho [a], Mathieu Linares [b,c,*]

[a] *Institute of Physics, University of Brasília, 70.919-970 Brasília, Brazil*
[b] *Department of Physics, Chemistry and Biology (IFM), Linköping University, SE-581 83 Linköping, Sweden*
[c] *Swedish e-Science Research Centre (SeRC), Linköping University, SE-581 83 Linköping, Sweden*

ABSTRACT

A study of electron mobility in a PCBM system is performed by means of analytical considerations and Kinetic Monte Carlo simulations. Orbital energies are calculated at the ZINDO level of theory and successively corrected considering contributions from permanent charges and polarization interactions. The relative importance of these environmental effects is analyzed in details, furthermore the predicted mobilities are compared with experimental results and similar simulations performed in C60.

© 2017 Elsevier B.V. All rights reserved.

1. Introduction

Organic electronics is a field that is currently gaining a lot of attention, with promises of devices that could take advantage from characteristics of organic materials such as flexibility, the capacity of tuning optical properties and low cost [1–4]. These promises have been partly fulfilled as evidenced by the fact that nowadays organic light-emitting diodes (OLEDs) have already been integrated to commercial technology. However, in devices such as organic photovoltaics (OPVs), efficiency is still a limiting factor for successful applications [5]. OPV devices work as follows [6–11]: (i) photons are absorbed by the material in the active layer of the device forming excitons; (ii) these excitons diffuse randomly until they reach the donor-acceptor interface, where they may dissociate into a charge transfer state; (iii) At this point, two possibilities emerge: (a) charges either recombine or (b) charges separate completely, in which case they move towards the electrodes. The efficiency of this last process is intrinsically related to the mobility of the charge carriers in the active layers of the device. The disordered morphology of organics films, in contrast to the crystalline structure of inorganic semiconductors, hinders band conduction and favors a process of conduction by hopping, in which charge carriers are localized in sites and move by means of a sequence of transfers between molecules. The rate with which these transfers occur can be calculated by means of Marcus theory [12], which depends on the energy difference between sites, the reorganization energy involved in the hop, the electronic coupling and tempera-

ture. To be able to simulate such a process is, thus, an important step towards better understanding charge transport in these materials and also a way to predict charge carrier mobility for novel materials even before their synthesis. There are mainly two criticisms to the use of the Marcus rate for charge mobility simulations [13–16]. First, nuclear tunneling effects may be important particularly in obtaining the correct mobility magnitude. Second, this semiclassical approach may fail in the limits of very low temperatures and very large electric fields. In the intermediate region, however, the Marcus theory may provide important insights into the temperature and field mobility dependences.

This work presents a theoretical study of electron mobility in [6,6]-phenyl-C61-butyric acid methyl ester (PCBM), a molecule often used as electron acceptor in organic electronics applications. The study involves analytical considerations and Kinetic Monte Carlo (KMC) simulations. A box of PCBM molecules is obtained from molecular dynamics (MD) calculations. We consider three levels of increasing complexity in the way energy contributions are taken into account: first by only including molecular orbital energies, then adding Coulombic interactions, and finally bringing in polarization effects. The results of electric field and temperature dependence on mobility, calculated with these various levels of theory, are compared to experimental results and with similar simulations performed with C60 [17]. The combination of Quantum Mechanical calculations – for obtaining the parameters necessary for calculating Marcus rates – MD and Monte Carlo simulations employed in this work allows for a detailed atomistic treatment of this challenging problem.

In the last years, the validity of such hopping models when applied to organic materials has been called into question, particularly in the case of fullerene and fullerene derivatives in crys-

---

* Corresponding author at: Department of Physics, Chemistry and Biology (IFM), Linköping University, SE-581 83 Linköping, Sweden.
E-mail address: mathieu@ifm.liu.se (M. Linares).

talline morphologies [18–20]. However, a recent study [21] suggests that even though delocalized electronic states may play an important role in charge transport for C60, this is not the case for PCBM. Another recent study also models charge transport in PCBM by means of a polaronic picture [22]. Therefore, this is a question that is not yet settled and requires further investigation. We hope this work may also contribute to this discussion.

2. Methods

A realistic structure of the systems has been obtained by means of MD simulations. Using the morphology obtained by MD, we performed KMC simulations to simulate the charge transport. The hopping rates for the KMC simulation are based on the Marcus formula [12]

$$
\begin{aligned}
w_{NM} = \frac{2\pi}{h} |H_{NM}|^2 \sqrt{\frac{1}{4\pi k_B T \lambda_{NM}}} \\
\times \exp\left(-\frac{(-e\vec{E} \cdot \Delta\vec{r}_{NM} + \Delta E_{NM} + \lambda_{NM})^2}{4\lambda_{NM} k_B T}\right)
\end{aligned}
\tag{1}
$$

representing the rate for the hop from the molecular orbital m of molecule i, $M = (i, m)$, to another molecular orbital n of molecule j, $N = (j, n)$. H_{NM} is the transfer integral, the coupling between the two molecular orbitals M and N. $\Delta E_{NM} = u_N - u_M$ is the difference in energy after and before the jump. The single site energy u_M is composed of 3 contributions

$$
u_M = O + C + P,
\tag{2}
$$

O is the energy of the molecular orbital M if the molecule i is in the vacuum, C is the contribution of the permanent charges of the molecules around, and P is the energetic contribution of the polarization of the nearby molecules. To study the effect of these energy contributions, simulations were performed with systems that considered only the O contribution; O and C simultaneously; and O, C and P contributions at the same time. These systems are henceforth denoted O, OC and OCP, respectively.

The term $-e\vec{E} \cdot \Delta\vec{r}_{MN}$ in Eq. (1) represents the energetic contribution of the field. λ_{NM} is the reorganization energy, the energy needed for the structural rearrangement of the system after the hop. It has two main origins. The internal reorganization λ_{int} comes from the conformational changes of the internal degrees of freedom of the single molecules after the hop. The external reorganization energy λ_{out} is the reorganization of the environment after the hop, considered through the induced dipoles on the nearby molecules. The induced dipoles, needed both for the site energy and for the external reorganization, are calculated using the linear Thole model [23]. A more detailed description of the methodology used can be found in Refs. [17,24].

An efficiency diagram will help us determine at which fields to expect good conduction in PCBM. This diagram, shown in Fig. 1, has been introduced in Ref. [24] as one of the parts forming the CT state splitting diagram. This diagram simply represents the dependence of the Marcus rate on the electric field (from Eq. (1)). Average parameters are calculated depending on the particular system and thus a single gaussian can be obtained representing the global properties of the system. In particular the efficiency diagram for an electron in the bulk shows the average Marcus rate as a function of electric field and allows us to estimate the region in which the conduction is possible. This region is defined as the interval between the maximum of the Gaussian function plus or minus three standard deviations. The rate of conduction is maximum when the argument of the exponential function in Eq. (1) becomes zero. The region around this value ($\pm 3\sigma$) can be expressed, following the notation of our previous paper [24]
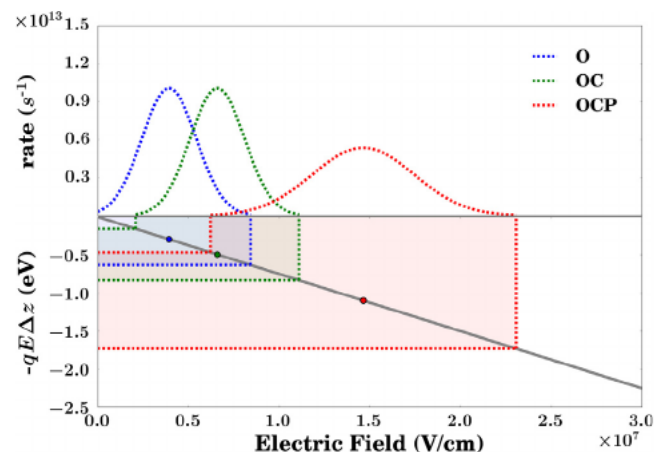

Fig. 1. Efficiency diagram for free electron in PCBM at $T = 300$ K for O, OC and OCP systems. The diagram shows the range of electric fields that favors conduction.

$$
-eE\Delta z_A \simeq -(\Delta E_{bulk}^e + \lambda_{bulk}^e)
\tag{3}
$$

where Δz_A is the average layer spacing in the direction of the field, ΔE_{bulk}^e and λ_{bulk}^e are the average difference in energy and reorganization energy in the bulk, respectively. The average parameters needed for Eq. (3) and thus Fig. 1 are calculated as detailed in Computational Details.

The efficiency diagram for $T = 300$ K in Fig. 1 shows how the correlation region moves according to the different energy contributions. In order to make meaningful comparisons between simulations performed with the three different systems, the electric fields considered here ranged from ca. 10^4 V/cm to 10^7 V/cm.

3. Computational details

3.1. Morphology

A box containing 1728 PCBM molecules was built using the Packmol program [25]. MD simulation in the NPT ensemble was performed with the Gromacs package [26–30] on this box using the Nosé-Hoover thermostat [31,32] (300 K) with a coupling constant of 0.2 ps and Parinello-Rhaman barostat [33,34] (1 atm) with a coupling constant of 0.2 ps. The cut-off distance applied for both electrostatic and van der Waals interactions is 1.5 nm. Total time of simulation was 10 ns. The density of the box converged to 1515.9 ± 0.2 kg m^{-3} (statistics for the last nanosecond of the dynamic). An energy minimization using the steepest descent method [35] was then performed before the KMC simulation to obtain a box in its average configuration and thus removing the dynamical disorder. Stopping an MD simulation at finite temperature often results in conformational parameters such as bond lengths and angles far from their equilibrium values (dynamical disorder). The final energy minimization step is performed to resolve this issue and obtain the average configuration over time (static disorder). The charge transport simulation is then performed on the final system without dynamical disorder, thus neglecting the instantaneous coupling between charge hopping and nuclear movements. The limitations of this approach have been studied by Poelking et al. in PBTTT systems [36] and briefly discussed in the context of our study in Ref. [17].

3.2. Molecular orbitals and transfer integrals

For every molecule in the bulk a quantum mechanical calculation at the ZINDO [37] level has been performed with the Gaussian

09 [38] software to obtain the LUMO orbital energies. Based on these calculations we also computed the LUMO-LUMO transfer integrals for all the molecules within a cutoff of 9 Å. These transfer integrals are calculated only once for the entire simulation, so possible influences resulting from polarization or electric fields in the distribution of transfer integrals are not taken into account. See Ref. [17] for details on the methods used.

3.3. Atomic charges and polarizabilities

Atomic charges have been calculated at the B3LYP/6-31+g(d) level of theory and can be found in SI. Atomic polarizabilities were taken from the paper of Wang et al. [39] as well as the screening factor for Linear Thole model. CL polarizabilities have been chosen in such paper and the chosen values can be also found in SI.

3.4. Reorganization energies

Internal reorganization energy was calculated with the B3LYP/6-31+g(d) level of theory yielding a value of 0.25 eV. This quantity was calculated only once and used for all calculations of Marcus rates.

External reorganization energy has been calculated as in Ref. [17] and using atomic charges and polarizabilities characterized in the previous section.

3.5. Efficiency diagram parameters calculation

To determine the different parameters necessary for the efficiency diagram five molecules are considered in the material and the results obtained are averaged. First we average all the transfer integrals in the opposite direction of the field (since we are considering the hoping of electrons). Willing to consider only the dominant paths, we neglect transfer integrals $|H_{NM}|$ with values lower than 7 meV. The distances and external reorganization energies are calculated with a weighted average, using as weights the square of the associated transfer integrals $|H_{NM}|^2$ (as in Marcus formula). Till this point calculation is very similar to what had been proposed in Ref. [24]. Regarding the average energy difference in the bulk ΔE^e_{bulk} (see Eq. (3)), a different estimation has to be made instead. In the present paper we are interested in the equilibrium mobility of the system, i.e. we are interested in the energy difference when the system is in the equilibrium of the Markov chain created by the KMC. This energy difference depends strongly on the correlation of the energetic landscape [40,41]. For the purposes of the present paper, being interested in some average estimation, a simpler model of independent Gaussians can be used [42]. In such a model, assuming to be at equilibrium means assuming that the charge carrier is in the lower tail of the DOS. The energy difference between two consecutive Gaussians can thus be taken as proportional to the DOS standard deviation and since we are interested in the orders of magnitude we will assume $\Delta E^e_{bulk} \sim \sigma_{DOS}$.

The obtained average transfer integral is $H_{NM} = 0.02$ eV, the interlayer distance is $\Delta z_A = 7.51$ Å. The sigma of the DOS for the three cases results: $\sigma_O = 0.05$ eV for O, $\sigma_{OC} = 0.25$ eV for OC and

$\sigma_{OCP} = 0.24$ eV for OCP (and can also be retrieved in Table 1). The internal reorganization energy as said in previous section is $\lambda_{int} = 0.25$ eV, while for the OCP case the averaged external reorganization energy is $\lambda_{NM} = 0.61$ eV.

3.6. Kinetic Monte Carlo

KMC simulations were performed considering 2000 hops in the case of the O systems and 6000 hops in the case of the OC and the OCP systems. Mobilities are obtained for each value of electric field and temperature as the average of several such simulations, more specifically 300 for the O systems and 600 for the OC and the OCP systems. Electric fields range from 6.3×10^4 V/cm to 1.1×10^7 V/cm and temperature varies from 220 K to 460 K. The suitable range of electric fields for the simulations have been found based on the efficiency diagram.
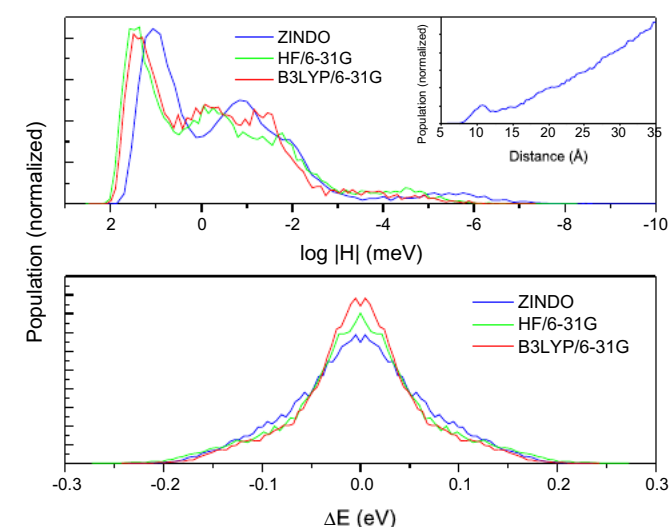
4. Results and discussion

4.1. System analysis

The radial distribution function of the PCBM system is shown in the inset of Fig. 2. The first shell is located at 11 Å, but beyond this point the position of the molecules are uncorrelated, which demonstrates the disordered state of the system.

Fig. 2 shows the distribution of transfer integrals (top) and site energy differences (bottom) calculated with three levels of theory, ZINDO, Hartree-Fock (HF) and DFT with the B3LYP functional. HF and DFT show almost overlapping transfer integrals distributions, slightly shifted to the left with respect to the ZINDO one, but with the same double-peak and shoulder structure. As to site energy differences (bottom of Fig. 2), these take into consideration only the orbital energy. All levels of theory predict a very symmetric distribution around 0 energy, but going from ZINDO to HF to B3LYP the distributions becomes sharper. All in all, the very similar results obtained in both cases indicate that the choice of ZINDO for the simulations is not only convenient, given the lower computational cost, but also adequate.

Taking a closer look at transfer integrals calculated with ZINDO, two main peaks are identified. The leftmost one is sharper and cor-

Table 1
Average, standard deviation and skewness of the density of states and of its individual components for the PCBM system.

	Average (eV)	SD (eV)	Skewness (eV)
O	−1.52	0.05	0.83
C	−0.04	0.24	−0.01
P	−1.04	0.15	−0.65
OC	−1.56	0.25	0.00
OCP	−2.60	0.24	−0.34

Fig. 2. (top) Distribution of the LUMO-LUMO transfer integrals calculated with three levels of theory for the PCBM box. Inset: Radial distribution of the PCBM molecules in the box. (bottom) Distribution of orbital energy difference between hopping sites in the PCBM system.

responds to the first neighbors shell. The second peak is broader and merges somewhat with the first as the system's disorder becomes prevalent, a result of the different orientations between molecules produced by the MD simulation.
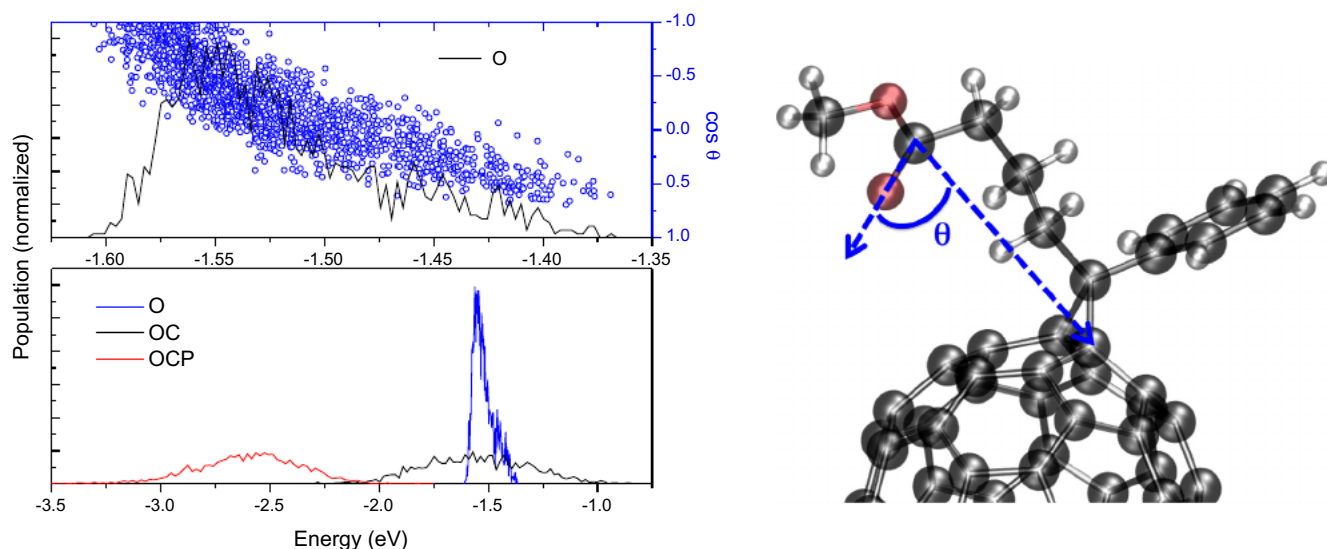
Fig. 3 shows the density of states (DOS) for the LUMO of the PCBM molecules in the system. When this is calculated taking into account only the contributions from the orbital energy (O), that is, leaving out Coulombic and polarization effects, the result is a rather asymmetric distribution that peaks around the -1.55 eV mark and shows a broad tail towards higher energies as seen in Fig. 3-a. This Figure also shows the correlation between the energy of the LUMO of each molecule and the cosine of the angle between two vectors, the one that connects the carbon to the oxygen in the carbonyl group and the one connecting this same carbon to the C60 cage (see Fig. 3 right). Higher values of this angle, which translate into larger distances between the carbonyl oxygen and the C60 cage, are correlated with lower energies. The molecules responsible for this asymmetry are mostly those with values of θ below $90°$. The inclusion of Coulombic and polarization effects produces some changes in the DOS, as seen in Fig. 3-b. These effects may be better understood by looking at Table 1, which shows the average, standard deviation (SD) and skewness of the distributions of each contribution to the total energy. As mentioned above, the orbital contribution (O) is asymmetric, as evidenced by a skewness of 0.83 eV, and narrow, with a standard deviation of 0.05 eV. On the other hand, the distribution of Coulombic energy (C) is much wider and symmetric, centered at nearly 0 eV, a result of the polarization between the positively charged C60 cage and the negatively charged tail. The combination of these two effects (OC) results in a wide symmetric distribution that remains centered around the -1.5 eV energy. The polarization (P) contribution is wider than the orbital one and is also asymmetric, though in the opposite direction, towards lower energies. Finally, when considering the three contributions (OCP), the shape of the distribution changes slightly, becoming more asymmetric with its center located at -2.6 eV.

A comparison between these results and similar simulations performed with a disordered C60 system [17] shows two main differences in the behavior of the DOS. First, the inclusion of Coulombic effects produces no change in the DOS of the C60 system, since the permanent charges in the molecules are all close to zero. Second, the inclusion of polarization produces a DOS with a standard deviation of 0.01, much narrower than the one obtained with the less symmetric PCBM. To summarize, the functionalization of C60 by polar group will provoke a broadening of the density of states.

4.2. Kinetic Monte Carlo simulations

In Fig. 4 the dependence of mobility on electric field is plotted for four different temperatures and for the O, OC and OCP PCBM systems. When only orbital energy is considered (O), the behavior of the mobility curve is characterized by remaining constant for a long range of fields before decreasing as it reaches the inverted Marcus region. The effect of adding Coulombic and polarization interactions is similar for all temperatures. First, it is noted that for low field values the mobility curve shows large lower error bars as the system is still in percolation region. For the sake of not polluting the plots, these error bars were removed and this region was marked by the rectangles in Fig. 4. The percolation region is that range of fields in which the drift of the charge carrier is negligible and the charge mainly moves through percolation in the energetic landscape of the material, giving a diffusive character to the conduction. This behavior can be visible in the mobility of the simulations both from the big error bars (that will not reduce with the ensemble size) and from the independence of the average mobility on the electric field (plateau). More information on the percolation region can be found in the early work by Bassler [42]. In the percolation region, even negative values of mobility appear at 220 K for the OCP system, which is why fewer data points are shown for OCP at this temperature. The range of these percolation regions diminishes with increasing temperature. The efficiency diagram of Fig. 1 (calculated for $T = 300$ K) allows to interpret the mobility results data (Fig. 4). In particular, the external reorganization associated with the polarization of the environment P contribution, widens the conduction Gaussian and thus creates a less steep dependence and shifts the deep inverse Marcus region to higher electric fields. From the efficiency diagrams we would expect the OC system to exit percolation region at about 2.5×10^6 V/cm ($\sqrt{F} \sim 1581$ (V/cm)$^{1/2}$) and the OCP at about 6×10^6 V/cm ($\sqrt{F} \sim 2449$ (V/cm)$^{1/2}$). It is noticeable that these values corre-

Fig. 3. Left: (a) Top: Density of states for the LUMO of the PCBM molecules in the box considering only orbital energy contributions. The blue circles show the correlation between LUMO energy and the cosine of the angle θ shown in the figure on the right. (b) Bottom: Comparison between the density of states for the LUMO of the PCBM molecules in the box calculated with the O, OC and OCP methods. (For interpretation of the references to color in this figure legend, the reader is referred to the web version of this article.)
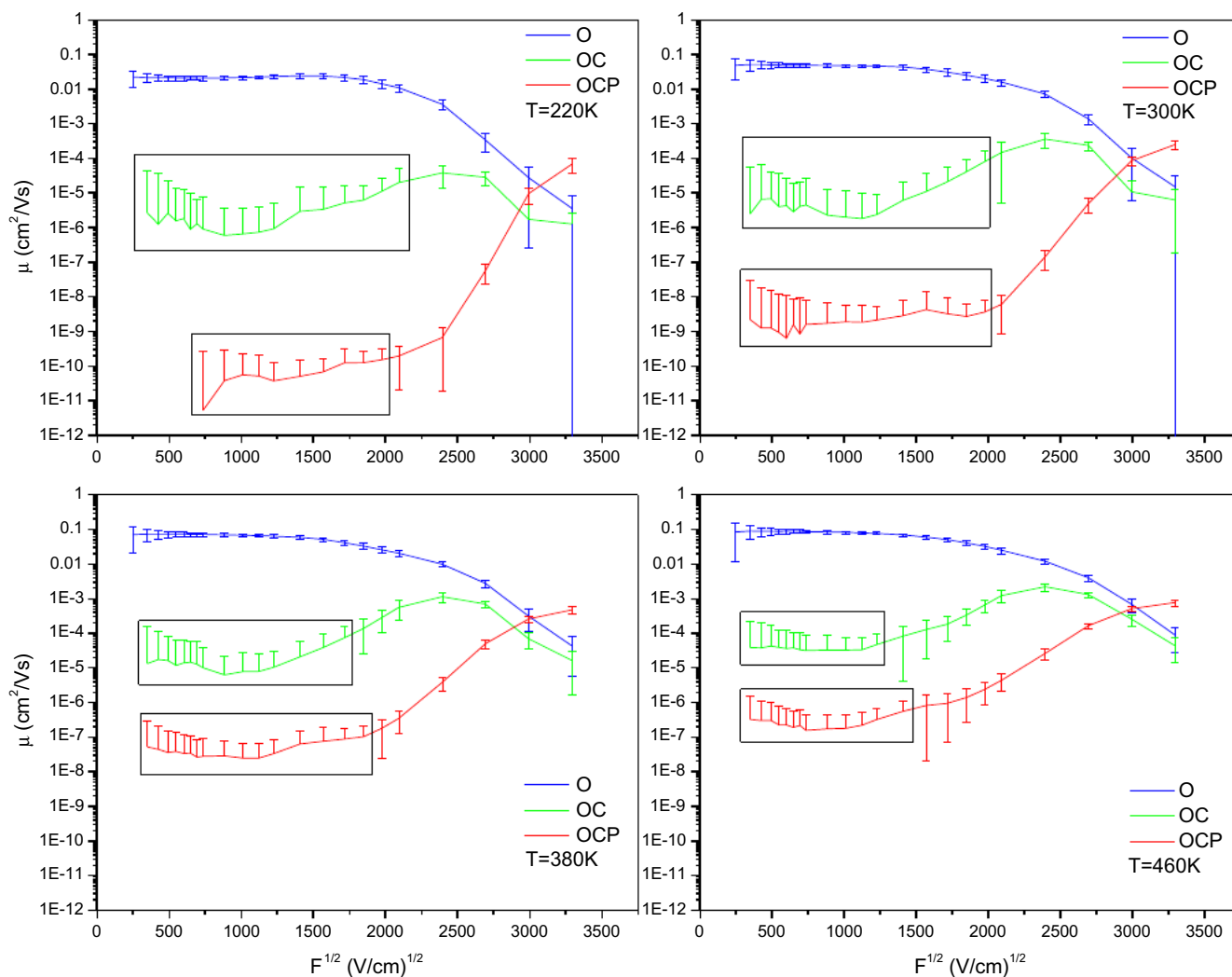
Fig. 4. Mobility dependence on electric field for four temperatures calculated with O, OC and OCP contributions to energy. Areas inside the rectangles correspond to the percolation region. These areas are characterized by large lower error bars that are here omitted for the sake of not polluting the plots.

spond roughly to the regions where the OC and OCP mobility curves in Fig. 4 for $T = 300$ K begin to rise as the field increases. There is no exact match because the efficiency diagram employs an independent Gaussians model (sec. Efficiency Diagram Parameters Calculation), which neglects the correlation of the energetic landscape. If willing to have more reliable efficiency diagrams, an estimation of the intrinsic energetic disorder of the system ζ is needed (as in Ref. [41]).

As to the OC systems, a large drop in mobility is observed in comparison to the O systems. Another important difference is the presence of a correlation region, where mobility increases with the electric field. This region is not large and the system reaches inverted Marcus regime for around the same field values as for the O system. The inclusion of polarization (the OCP system) produces more significant changes. After leaving the percolation range, correlation region is reached and mobility increases from two to six orders of magnitude, depending on temperature. As temperature increases, variations in mobility in this region become less intense. It is worth noting, however, that in spite of the differences in behavior in the OC and the OCP simulations, both of them predict similar maximum values of mobility. The remarkable difference in behavior seen in the simulations that include Coulomb and polarization effects, that is, the existence of a correlation region, can be attributed to the increase in the energetic disorder

that appears when these contributions are taken into account (see Fig. 3). The distribution of orbital energies in the system after the MD simulation is not enough to reproduce the energetic disorder of a real system.

The dependence of mobility on temperature is plotted in Fig. 5 for four values of electric field. For the O system, mobility remains practically constant. Moving to the OC and the OCP systems, they clearly become more sensitive to temperature changes. As field values increase and the mobility points move away from the percolation region, the behavior observed approaches an exponential decay with $1/T$, which is characteristic of hopping processes [43].

4.2.1. Comparison with experiments

Experimental data [44–46] (Available in SI) shows some quantitative differences with respect to the simulations, but also shows qualitative agreement. First, the range of electric fields of interest in the simulations is largely shifted towards higher fields, regardless of the contributions to energy taken into consideration (referred subsequently as field shift). For instance, the correlation regions predicted for the OCP and, to a lesser extent, for the OC systems are in qualitative agreement with experiment, even though they are in fact observed for much lower fields. This field shift is a shortcoming of the method that is not influenced neither by the level of theory used in the ab initio calculations nor by the con-
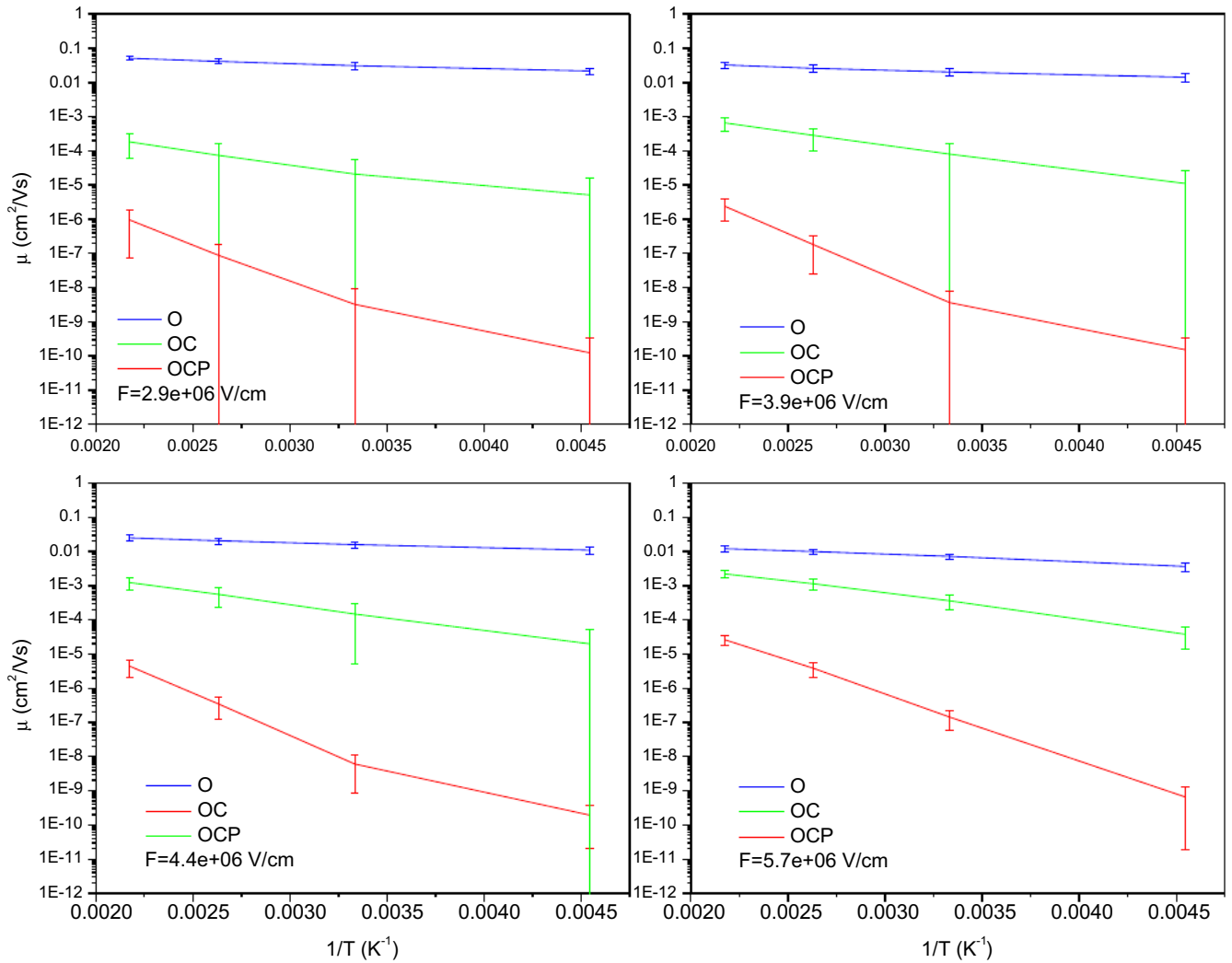
Fig. 5. Mobility dependence on temperature for four values of electric field calculated with O, OC and OCP contributions to energy.

tributions to energy that are considered. It is also present in the simulations performed with C60, so it also not system dependent. Further investigation is needed to address this issue.

Experiment also shows that the correlation region is softened as temperature increases, which can also be seen in our simulations. However, measurements indicate that already at 295 K, mobility becomes more field independent whereas simulations performed at 460 K still show mobility increasing with electric field. This milder dependence on the temperature, combined with the fact that the field shift cannot be solved with parameter fitting in Marcus theory [17], reinforces the conviction that a new model (like Marcus-Levich-Jortner) is needed to address these two points in particular. In this case, a different dependence on the temperature would also be expected due to the possibility of vibrational tunneling effects.

Another difference lies in the magnitude of the predicted mobilities (or magnitude shift). Experimental data point to a mobility in the order of 10^{-3} to 10^{-2} cm^2 V^{-1} s^{-1} for PCBM films. Simulated mobilities of this order are obtained as the maximum values for the OC and the OCP systems at temperatures of 380 K and higher. However, the O system manages to predict mobility in the experimental order of magnitude even if it fails at reproducing the mobility-field and mobility-temperature dependence. This is the case because the O system presents a much sharper DOS than

the OC and OCP systems. The mobility magnitude obtained from KMC simulations for PCBM in Ref. [47] at $T = 300$ K and $\sqrt{F} \sim 300$ (V/cm)$^{1/2}$ (3.1×10^{-2} cm^2 V^{-1} s^{-1}) is comparable to those predicted by the O system in the same conditions ($\sim 5.0 \times 10^{-2}$ cm^2 V^{-1} s^{-1}).

As to temperature dependence, experimental results indicate that mobility decays exponentially with $1/T$. This behavior is reproduced in the OC and the OCP simulations only for high field values. This relationship is customarily modeled by [43]

$$\mu = \mu_0 \exp\left(-\frac{\lambda}{4kT}\right), \qquad (4)$$

where λ is the reorganization energy. For a field of 5.7×10^6 V/cm, OC and OCP mobility-temperature curves present this exponential behavior more clearly, with λ equal to 0.58 eV and 1.54 eV, respectively. Experimental curves show a value of 0.64 eV, closer to the one obtained from OC simulations. This reinforces once again the conviction that the inclusion of external reorganization energy may be excessive, which stands to reason, as measurements are performed in organic solid films. Also external reorganization is calculated from a full repolarization of the nearby molecules and this might be true only partially, depending on the relative velocity of polarization, compared to charge hopping (see also discussion in Ref. [17]).

These results prompt the question of how the mobility simulations would change if external reorganization energy were to be disconsidered. The results are shown in Fig. 2, SI. It can be seen that without external reorganization energy, predicted mobilities for lower field values increase significantly, from 2 to 4 orders of magnitude depending on temperature. On the other hand, the maximum mobility does not change in comparison to the simulations performed with external reorganization energy, resulting in less steep mobility-field curves. Furthermore, these simulations still show the clear percolation character of the OCP system without λ_{out}, still extending to relatively high electric field. Finally, it can also be seen that the mobility curves reach inverted Marcus region for lower field values. In summary, an excessive reorganization energy may be responsible for low mobility values in the low field domain, but does not explain the field shift that is observed in the simulations.

4.2.2. Comparison with C60 simulations

In a previous study, mobility simulations like the one presented here were performed in a disordered C60 system [17]. Results showed that the OCP simulations provided better qualitative agreement with experiment. However, in that case, the OC simulations behaved much like the O simulations for PCBM, showing no correlation region whatsoever. Only with the inclusion of polarization effects, in particular because of the addition of external reorganization energy, the shape of the mobility curves changed, approaching their experimental counterparts. This difference in behavior between mobility curves in C60 and PCBM may be attributed to the fact that the standard deviation of the DOS of the OC C60 system is much lower than the one for the OC PCBM system, 250 times lower in fact.

In terms of magnitude, C60 simulations predicted maximum mobilities for OCP systems on the order 10^{-2} cm^2 V^{-1} s^{-1}. This is one order of magnitude larger than the values obtained for PCBM, which is fairly close to experimental data that indicates that mobility in PCBM is 40 times smaller than in C60 [44].

The comparison between PCBM and C60 simulations aims at understanding whether the factors that allowed for the correct qualitative behavior of the mobility field dependence in C60, namely the inclusion of polarization effects and external reorganization energy, play the same role for PCBM. This is indeed not the case. The OC simulations for PCBM resulted in the correct qualitative behavior with the advantage of also presenting higher mobilities than the OCP ones, closer to experimental values. The reason is that in the case of PCBM the Coulombic contribution to the DOS is the most important one, being the main factor of the DOS broadening (see Table 1). The inclusion of polarization does not change the broadness of the DOS significantly. The difference between the OC and OCP mobility curves for PCBM is thus given by the external reorganization energy. Its contribution is twofold: it pushes the inverted region towards higher fields in comparison to OC systems and reduces the predicted mobilities, as was observed in the case of C60. These findings demonstrate that the correct settings for a KMC mobility simulation are very much system dependent, and depend on the delicate interplay between DOS and external reorganization energy as can be also evinced a priori from the efficiency diagram (see sec. Methods).

5. Conclusions

The electron mobility in a PCBM system was calculated with a KMC method. The calculations of the DOS showed an asymmetric behavior that we were able to attribute to a specific conformation of the carbonyl group with respect to the C60 sphere. The calculated mobility field dependence displayed good qualitative agree-

ment with experiment when the effect of polarization was included. In particular, two effects are mainly affecting the mobility: (i) the correlation of the energetic landscape coming from the interaction of the charge carrier with the nearby molecules (permanent atomic charges and induced dipoles); and (ii) the external reorganization energy after each charge hopping. Mobility-temperature simulations indicate that for high values of electric field, mobility decays exponentially with $1/T$. Comparison with experimental data shows that this behavior was better reproduced when Coulombic interactions were included, but not polarization effects. This could be attributed to the fact that our model overestimates the external reorganization energies by assuming a full repolarization of the system. This results in a significant drop in mobility and in a stretching of the correlation region that pushes the inverted Marcus region towards higher electric fields. When simulations performed with C60 are compared to the ones for PCBM, it is noted how both the DOS and the external reorganization energy are affecting charge transport and need to be considered for a realistic description. How much of the reorganization energy has to be considered (till what extent the environment will repolarize between two consecutive hops) remain still matter of debate. The overall good qualitative agreement with experiments is satisfactory. The magnitude of mobility can be adjusted tuning the percentage of external reorganization considered, but the fields at which conduction is expected from the efficiency diagram (and subsequently observed in the KMC) are too high compared with the experiments. This field shift seems to suggest the need of including tunneling in our model. For instance, a Marcus-Levich-Jortner type of rate [48] could allow us to solve the field shift and reach a quantitative agreement with experiment. A more general hopping rate, which reduces – in the appropriate limits – to different more well known rates such as the Miller-Abrahams one, has also been proposed [49]. Investigating these possibilities will be the aim of future efforts.

Acknowledgments

References

[1] S.R. Forrest, Nature 428 (2004) 911–918.
[2] J.-H. Kim, M.J. Han, S. Seo, J. Polym. Sci., Part B: Polym. Phys. 53 (2015) 453–460.
[3] A. Facchetti, Chem. Mater. 23 (2010) 733–758.
[4] D.J. Gundlach, Nat. Mater. 6 (2007) 173–174.
[5] M.A. Green, K. Emery, Y. Hishikawa, W. Warta, E.D. Dunlop, Prog. Photovoltaics: Res. Appl. 23 (2015) 1–9.
[6] C.J. Brabec, J.A. Hauch, P. Schilinsky, C. Waldauf, MRS Bull. 30 (2005) 50–52.
[7] J.-L. Brédas, J.E. Norton, J. Cornil, V. Coropceanu, Acc. Chem. Res. 42 (2009) 1691–1699.
[8] E. von Hauff, Semiconduct. Semimet. 85 (2011) 231.
[9] K. Vandewal, K. Tvingstedt, O. Inganäs, Semiconduct. Semimet. 85 (2011) 261.
[10] C. Deibel, T. Strobel, V. Dyakonov, Adv. Mater. 22 (2010) 4097–4111.
[11] Y.-T. Fu, D.A. da Silva Filho, G. Sini, A.M. Asiri, S.G. Aziz, C. Risko, J.-L. Brédas, Adv. Funct. Mater. 24 (2014) 3790–3798.
[12] R.A. Marcus, J. Chem. Phys. 24 (1956) 966–978.
[13] N. Van Der Kaap, I. Katsouras, K. Asadi, P.W. Blom, L. Koster, D.M. de Leeuw, Phys. Rev. B 93 (2016) 140206.
[14] Y. Jiang, X. Zhong, W. Shi, Q. Peng, H. Geng, Y. Zhao, Z. Shuai, Nanoscale Horizons 1 (2016) 53–59.
[15] O. Ostroverkhova, Chem. Rev 116 (2016) 13279–13412.

[16] K. Asadi, A.J. Kronemeijer, T. Cramer, L.J.A. Koster, P.W. Blom, D.M. De Leeuw, Nat. Commun. 4 (2013) 1710.
[17] R. Volpi, S. Kottravel, M.S. Nørby, S. Stafstrom, M. Linares, J. Chem. Theory Comput. 12 (2016) 812–824.
[18] D.L. Cheung, A. Troisi, J. Phys. Chem. C 114 (2010) 20479–20488.
[19] H. Oberhofer, J. Blumberger, PCCP 14 (2012) 13846–13852.
[20] F. Gajdos, H. Oberhofer, M. Dupuis, J. Blumberger, J. Phys. Chem. Lett. 4 (2013) 1012–1017.
[21] G. D'Avino, Y. Olivier, L. Muccioli, D. Beljonne, J. Mater. Chem. C 4 (2016) 3747–3756.
[22] K. Pelzer, Á. Vázquez-Mayagoitia, L.E. Ratcliff, S. Tretiak, R. Bair, S. Gray, T. Van Voorhis, R. Larsen, S. Darling, Chem. Sci. (2017).
[23] B.T. Thole, Chem. Phys. 59 (1981) 341–350.
[24] R. Volpi, R. Nassau, M.S. Nørby, M. Linares, ACS Appl. Mater. Interfaces 8 (2016) 24722–24736.
[25] L. Martínez, R. Andrade, E.G. Birgin, J.M. Martínez, J. Comput. Chem. 30 (2009) 2157–2164.
[26] H.J. Berendsen, D. van der Spoel, R. van Drunen, Comput. Phys. Commun. 91 (1995) 43–56.
[27] E. Lindahl, B. Hess, D. Van Der Spoel, J. Mol. Model. 7 (2001) 306–317.
[28] D. Van Der Spoel, E. Lindahl, B. Hess, G. Groenhof, A.E. Mark, H.J. Berendsen, J. Comput. Chem. 26 (2005) 1701–1718.
[29] B. Hess, C. Kutzner, D. Van Der Spoel, E. Lindahl, J. Chem. Theory Comput. 4 (2008) 435–447.
[30] S. Pronk, S. Páll, R. Schulz, P. Larsson, P. Bjelkmar, R. Apostolov, M.R. Shirts, J.C. Smith, P.M. Kasson, D. van der Spoel, Bioinformatics (2013) btt055.
[31] S.U.I. Nosé, Mol. Phys. 100 (2002) 191–198.
[32] W.G. Hoover, Phys. Rev. A 31 (1985) 1695.
[33] M. Parrinello, A. Rahman, J. Appl. Phys. 52 (1981) 7182–7190.
[34] S. Nosé, M. Klein, Mol. Phys. 50 (1983) 1055–1076.
[35] M. Bixon, S. Lifson, Tetrahedron 23 (1967) 769–784.
[36] C. Poelking, E. Cho, A. Malafeev, V. Ivanov, K. Kremer, C. Risko, D. Andrienko, J. Phys. Chem. C 117 (2013) 1633–1640.
[37] M.C. Zerner, G.H. Loew, R.F. Kirchner, U.T. Mueller-Westerhoff, J. Am. Chem. Soc. 102 (1980) 589–599.
[38] M.J. Frisch, G.W. Trucks, H.B. Schlegel, G.E. Scuseria, M.A. Robb, J.R. Cheeseman, G. Scalmani, V. Barone, B. Mennucci, G.A. Petersson, H. Nakatsuji, M. Caricato, X. Li, H.P. Hratchian, A.F. Izmaylov, J. Bloino, G. Zheng, J.L. Sonnenberg, M. Hada, M. Ehara, K. Toyota, R. Fukuda, J. Hasegawa, M. Ishida, T. Nakajima, Y. Honda, O. Kitao, H. Nakai, T. Vreven, J.A. Montgomery, Jr., J.E. Peralta, F. Ogliaro, M. Bearpark, J.J. Heyd, E. Brothers, K.N. Kudin, V.N. Staroverov, R. Kobayashi, J. Normand, K. Raghavachari, A. Rendell, J.C. Burant, S.S. Iyengar, J. Tomasi, M. Cossi, N. Rega, J.M. Millam, M. Klene, J.E. Knox, J.B. Cross, V. Bakken, C. Adamo, J. Jaramillo, R. Gomperts, R.E. Stratmann, O. Yazyev, A.J. Austin, R. Cammi, C. Pomelli, J.W. Ochterski, R.L. Martin, K. Morokuma, V.G. Zakrzewski, G.A. Voth, P. Salvador, J.J. Dannenberg, S. Dapprich, A.D. Daniels, O. Farkas, J.B. Foresman, J.V. Ortiz, J. Cioslowski and D.J. Fox, Gaussian 09 Revision C.01, Gaussian Inc.
[39] J. Wang, P. Cieplak, J. Li, T. Hou, R. Luo, Y. Duan, J. Phys. Chem. B 115 (2011) 3091–3099.
[40] D.H. Dunlap, V.M. Kenkre, P.E. Parris, J. Imag. Sci. Technol. 43 (1999) 437.
[41] R. Volpi, S. Stafström, M. Linares, J. Chem. Phys. 142 (2015) 094503.
[42] H. Bässler, Phys. Status Solidi (b) 175 (1993) 15–56.
[43] A. Köhler, H. Bässler, Electronic Processes in Organic Semiconductors: An Introduction, John Wiley & Sons, 2015.
[44] V.D. Mihailetchi, J.K. van Duren, P.W. Blom, J.C. Hummelen, R.A. Janssen, J.M. Kroon, M.T. Rispens, W.J.H. Verhees, M.M. Wienk, Adv. Funct. Mater. 13 (2003) 43–46.
[45] E. von Hauff, V. Dyakonov, J. Parisi, Sol. Energy Mater. Sol. Cells 87 (2005) 149–156.
[46] C. Yang, J.Y. Kim, S. Cho, J.K. Lee, A.J. Heeger, F. Wudl, J. Am. Chem. Soc. 130 (2008) 6444–6450.
[47] I. Yavuz, S.A. Lopez, J.B. Lin, K. Houk, J. Mater. Chem. C 4 (2016) 11238–11243.
[48] J. Jortner, M. Bixon, J. Chem. Phys. 88 (1988) 167–170.
[49] R.P. Fornari, J. Aragó, A. Troisi, J. Chem. Phys. 142 (2015) 184105.

Article 4

Biexciton cascade emission in multilayered organic nanofibers

Leonardo Evaristo de Sousa, Wiliam Ferreira da Cunha,[a] Demétrio Antônio da Silva Filho, and Pedro Henrique de Oliveira Neto
Institute of Physics, University of Brasilia, Brasilia 70910-900, Brazil

The optical performance of multilayered organic nanofibers results from the dynamics of excited states in the system. Here, we show that the presence of biexcitons is crucial to correctly describe such dynamics. This may be the case even if the intensity of the light source is not high. The cascade emission mediated by biexcitons is mainly responsible for the behavior of the photoluminescence profile in the initial steps after light absorption. By using a combination of Kinetic Monte Carlo model and Genetic Algorithm, we simulate Time-Resolved Photoluminescence measurements of multilayered nanofibers. These simulations are compared with experimental results, thus revealing that the usual singlet exciton recombination is insufficient to reproduce the complete physical picture. Our results also include predictions for the behavior of the biexciton signal. These findings are observed to be valid for a wide temperature range, showing the importance of the biexciton cascade emission in several regimes for organic nanofibers in general. *Published by AIP Publishing.*
https://doi.org/10.1063/1.5023185

Organic nanofibers are of great scientific interest due to their potential applications in optoelectronic devices.[1,2] In particular, the combination of different molecular species to produce multilayered organic nanofiber structures allows for the tuning of the optical properties of such devices.[3] Many of the interesting properties these systems present result from their exciton dynamics. Understanding exciton behavior in this class of organic materials is, therefore, paramount to the rational design of optoelectronic devices. A particularly interesting question is how excitons interact with one another and whether such interactions impact the performance of the device.

Exciton dynamics can be studied both experimentally and theoretically. From the experimental standpoint, time-resolved photoluminescence (TRPL) measurements are important tools to access the behavior of excitons right after their creation.[4,5] Simulations, on the other hand, may be used to make connection between the observed results and the physical mechanisms involved in the exciton dynamics.[6] In this sense, a recent study[7] investigated exciton diffusion by performing TRPL measurements on a system composed of ten alternating layers of para-hexaphenyl (P6P) and α-sexithiophene (6T) nanofibers. The P6P layers were 163 Å thick, whereas the thickness of the 6T layers were of 3.7 Å. In the experimental setup, although only the P6P nanofibers absorbed light, photon emission from both materials was observed. Two mechanisms were used to explain the results: usual exciton recombination and exciton migration from the P6P to 6T layers by means of Förster resonance energy transfer. This exciton migration is possible for excitons moving from P6P to 6T but not the other way around. This is so because Förster transfer requires an overlap between the emission and absorption spectra of the donor and acceptor species, respectively. As a result, excitons that migrate to the 6T layers become confined.

When exciton concentration is large, exciton-exciton interactions may play a role in the experimental results with multiexciton states such as biexcitons being found. When it comes to the relaxation of biexcitons, a phenomenon of cascade emission has also been observed in different materials.[8,9] In this case, when two excitons move close to each other, they combine into a biexciton. The radiative decay of the biexciton takes place much faster than single exciton recombinations. It consists of a two-step process, in which two photons are emitted. The first possesses an energy corresponding to the difference between the biexciton and exciton energies. This emission subsequently stimulates the emission of a second photon. The last photon has an energy corresponding to the exciton energy—the same energy a photon would have had it been emitted after an usual exciton recombination. Alternatively, biexcitons may also recombine nonradiatively by means of an Auger process[10,11] in which the exciton energy is transferred as kinetic energy to electrons or holes.[11,12]

In this work, we demonstrate the existence of biexciton cascade emissions in organic nanofibers. Our results show that this mechanism is especially important when the exciton concentration is high, which corresponds to the initial moments after light absorption. We show this by employing a Kinetic Monte Carlo (KMC) model to simulate TRPL spectra. In order to investigate the importance of the exciton-exciton interaction in defining the PL spectra, we compare the performance of two versions of the model, with and without biexcitons, with the experimental curves. Furthermore, we present the predicted behavior of the photons emitted by the biexcitons as a function of time in both materials. Our results contribute to a better understanding of exciton dynamics in organic nanofibers by underlining the role played by biexcitons in forming the PL spectra.

The mechanism responsible for singlet exciton diffusion is the Förster energy transfer. The probability of an exciton performing a Förster transfer to a nearby molecule is given by[13]

[a]Electronic mail: wiliam@unb.br

$$\Phi(d) = \frac{1}{1 + \left(\dfrac{r}{R_F}\right)^6}, \qquad (1)$$

where r is the intermolecular distance and R_F is the Förster radius, the distance at which the efficiency of Förster transfer is 50%.

KMC simulations have been extensively used to study exciton diffusion in organic materials[14–19] as well as charge transport.[20–22] In our approach of using a KMC model to simulate exciton dynamics, two regimes were considered: one that neglects and another that accounts for exciton-exciton interactions in the form of a biexciton cascade emission process. In the non-interacting regime, at each time step, excitons either hop to their nearest neighbors or recombine. The program registers the time and the material in which the recombination takes place. This allows us to simulate TRPL measurements. When exciton-exciton interactions are included, excitons that hop to the same site may form biexcitons. These biexcitons promptly decay, emitting a low energy photon and stimulating the emission of a second higher energy photon, thus giving rise to a cascade emission process. Since biexciton lifetimes are much shorter than exciton lifetimes,[10,23] biexciton migration was not considered in the model. When cascade emissions are not taken into account, the model requires the r/R_F ratio in P6P (d_{P6P}) and 6T (d_{6T}) as inputs. These ratios control the efficiency of the Förster transfer in the two materials as shown in Eq. (1). The model also requires the number of monolayers (L) that compose the P6P portion of the device. This number affects the proportion of excitons generated near the interface and thus the amount of excitons that migrates from one material to the other. The 6T portion of the system, on its turn, is composed of a single layer. When exciton-exciton interactions are taken into account, exciton concentration (ρ) is also included, which controls the amount of biexcitons generated. To distinguish the efficiency with which such a process could happen in both materials, we also add a probability for mutual exciton-exciton annihilation in 6T ($1 - P_{XX}$, where P_{XX} is the probability of biexciton cascade emission). The inclusion of the last parameter accounts for the fact that biexciton cascade emissions may be suppressed by non-radiative Auger recombination.

In order to find the set of model parameters that best reproduce the experimental results, we make use of a Genetic Algorithm (GA). Even though parameters such as L are expected to remain constant for all temperatures, we do not enforce this condition, giving the GA more freedom to find the optimal values for each temperature. On the other hand, d_{P6P} and d_{6T} may vary more significantly since the efficiency of Förster transfer is expected to change with temperature. Experimental TRPL measurements for P6P and 6T were obtained by integrating over the 400–480 nm and the 510–650 nm intervals, respectively. All other experimental details are found in the original work, Ref. 7, which reports these results. Their experimental and our simulated TRPL curves for P6P and 6T were normalized by the sum of the areas for both curves, and so, they could be compared. This procedure amounts to equating the number of excitons that

recombine radiatively in both the experiment and the simulation, while keeping the correct proportion of photon emission from the two materials. The GA then searches for the set of parameters that minimized the root mean squared deviation from the experimental curves. To facilitate this comparison, a Savitzky-Golay filter[24] was applied to all curves to smooth the data.

It was previously reported in the literature[7] that the experimental P6P PL curve could be well fitted by a biexponential function, suggesting that two distinct mechanisms would be at work. The authors claim that the first mechanism would be the regular exciton recombination, dominant for longer times, and the second, relevant for initial times, was attributed to exciton migration from P6P to 6T. By following this path, we begin by analyzing the performance of the model that disregards exciton-exciton interactions in what could be described as the low exciton concentration limit. In this sense, Fig. 1 shows the comparison between experimental and simulated P6P and 6T (inset) TRPL. Because temperature is an important factor in Förster transfer, we investigate the behavior of the system under several temperature regimes between 80 K (top) and 300 K (bottom panel). The results relative to these two limiting temperatures are presented here. All the temperatures in this range followed a consistent trend indicated by these cases. The parameters for the 80 K simulation were $L = 25$, $d_{P6P} = 0.54$, and $d_{6T} = 0.41$, whereas for 300 K, they were $L = 16$, $d_{P6P} = 0.47$, and $d_{6T} = 0.44$. For P6P, one can note that the simulation manages to correctly describe the behavior of the curve at 80 K but is unable to reproduce the rapid decay that occurs in the first 0.25 ns at 300 K. At this temperature, agreement is obtained only for later times. This difference implies that the no exciton interaction model becomes less reliable as temperature increases, which correlates with an increase in Förster transfer efficiency. The modeled curves for 6T, shown in the insets of Fig. 1, on the other hand, show a major disagreement with regard to experimental TRLP spectra for both temperatures. The experimental curves show a rapid increase in emission followed by a steady decay. In the simulated curves, this increase corresponds to excitons migrating from P6P to 6T and starting to recombine. However, the increase in intensity
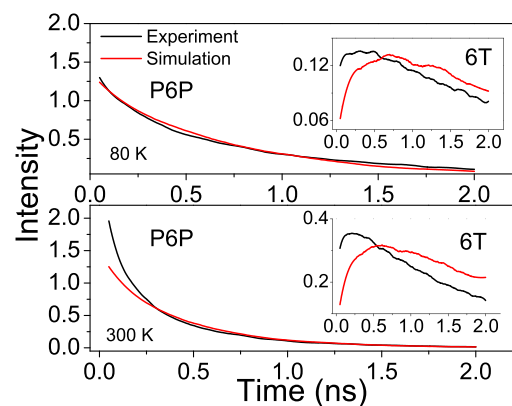

FIG. 1. Experimental[7] (black) and simulated (red) P6P and 6T (insets) TRPL at 80 K (top) and 300 K (bottom). Simulations were performed with no exciton-exciton interaction. Notice the disagreement between the curves for initial times, particularly for the higher temperature.

observed at the initial moments of the simulation is not sharp enough and not as intense to reproduce the experimental behavior. For later times, exciton migration is no longer dominant and the curves show a continuous decrease similar to the one found in the P6P curve. It is also clear that for later times, the simulation overestimates the emission in 6T. Again, one can see that as temperature increases, the disagreement between the simulated and the experimental curves increases accordingly.

It is important to mention that the simulated curves were obtained by means of a GA. The employed GA searched for the set of model parameters that minimized the difference between the curves. This means that the poor agreement between simulation and measurements does not result from the wrong parameter choice but from the incomplete physical picture described by the model. In searching for the optimal parameters of the no interaction model, the GA favors configurations that overestimate exciton migration in an effort to match the initial behavior of the 6T curve. This can be achieved by selecting lower numbers of monolayers (L) and d_{P6P}. However, regardless of the number of excitons that move from P6P to 6T, recombination does not occur fast enough to generate the sharp peak we see in the experimental curve. This overestimation of exciton migration results in a higher emission intensity in 6T than that experimentally observed for later times.

At this point, it is clear that the model, as is, is unable to correctly describe exciton dynamics under the experimental conditions in neither material. This is noticeable for the first moments after light absorption and particularly evident for higher temperatures. This suggests that another type of effect plays an important role in defining the early stages of the process. Since in these first moments, exciton concentration is at its highest values, it stands to reason that the source of the poor agreement between simulation and experiment is the neglect of exciton-exciton interactions of some sort. By analyzing the experimental results, we can immediately rule out non-radiative processes such as exciton-exciton annihilation as the source of error, because of the observed increase in emission in the initial moments after light absorption. Therefore, a different mechanism seems to be at play, one which leads to an increase in PL intensity right after photo-absorption: the arise of multiexciton species resulting from exciton-exciton interactions, namely, biexcitons.

In order to address the deficiency of the reported results, the improved version of the model allows for biexcitons to arise from exciton-exciton interactions. Now, in the simulation, when two excitons hop towards the same position, a cascade emission process is allowed to take place, meaning that two photons are emitted promptly. Similar to the previous discussion, Fig. 2 shows, for both P6P and 6T, the comparison between experiment and simulated TRPL measurements for 80 K (top) and 300 K (bottom). Parameters for the simulation at 80 K were $L = 16$, $d_{P6P} = 0.64$, $d_{6T} = 0.43$, $\rho = 0.006$ exciton per P6P site, and $P_{XX} = 0.43$. For 300 K, these were $L = 17$, $d_{P6P} = 0.44$, $d_{6T} = 0.46$, $\rho = 0.007$ exciton per P6P site, and $P_{XX} = 0.29$.

By including the possibility of cascade emission, one clearly sees that the simulation manages to correctly reproduce the behavior of both P6P and 6T curves for all time
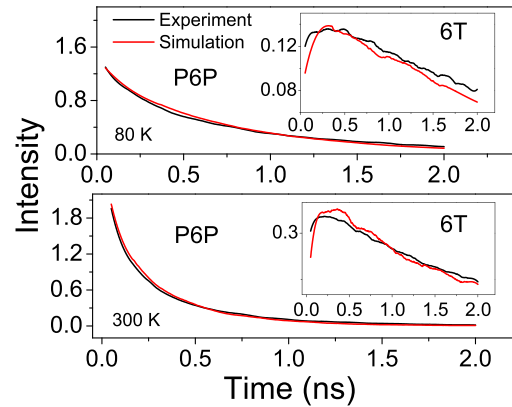

FIG. 2. Experimental[7] (black) and simulated (red) TRPL for P6P and 6T (insets) at 80 K (top) and 300 K (bottom). Here, biexciton cascade emissions were taken into account. A substantially improved agreement is obtained both for initial and later times even when considering higher thermal regimes.

periods. Note that good agreement between the experimental and the simulated spectra is obtained even for the high temperature regime. This is also true for all the temperatures (not shown here) in the considered range. The effect of cascade emission benefices from the high exciton concentration present in the initial moments and from the increase in the efficiency of the Förster transfer that is found to occur at higher temperatures. For later times, the usual exciton recombination mechanism is the dominant one. It is worth noting that in the experiment analyzed here,[7] it was reported that optical absorption in P6P was temperature-insensitive, and so, changes in the absorption cross-section with temperature play no role.

For the 6T curves, which presented a particularly poor agreement in the non-interacting version of our model, the inclusion of biexcitons managed to reproduce the sharp peak observed in the first 0.25–0.5 ns. This is done with no harm to the emission for later times, which is now also correctly described. We attribute the slight disagreement found around the zero time mark to the overestimation of the time it takes for an exciton to hop at the interface. This is a result of the approximation adopted in defining the time step of the simulation. Regardless of this fact, the overall improvement in the description obtained from the inclusion of biexciton cascade emission is remarkable.

In addition, the morphology of the system—in which very thin 6T layers are alternated with thicker P6P layers—combined with the fact that Förster transfers are allowed from P6P to 6T (but not the other way around) results in excitons being confined in the thin 6T portions of the material. In these regions, exciton concentration is bound to be large, provided that Förster transfer is efficient enough to allow for the migration of many excitons. Therefore, it is not unreasonable to consider the possibility of biexciton formation under these circumstances.

It is important to note that to make comparisons between experimental and simulated time-resolved photoluminescence spectra, we normalized both curves. This normalization must be performed by equating the sum of the areas of the P6P and 6T curves in both spectra. This amounts to considering that both curves share the same number of emitted

photons. A different normalization scheme, for instance, normalizing the curves by their maximum value, would result in comparing spectra produced in different conditions but that artificially share a similar starting point. Therefore, the curves obtained at different temperatures in Figs. 1 and 2 cannot be compared directly. However, the simulated spectra for P6P and 6T at a given temperature may be compared directly since they are normalized in the same way.

Furthermore, by fitting both P6P and 6T simulated TRPL spectra with biexponential functions, we obtain the characteristic times for the processes involved. At 80 K, the P6P slow and fast time components were found to be 768 ps and 123 ps, respectively, whereas for 6T, they were 2424 ps and 123 ps. At 300 K, the values for P6P were found to be 345 ps and 83 ps and those for 6T were determined to be 1515 ps and 99 ps. It is important to notice that, for both temperatures, the slow time components for both materials were very similar, as previously reported.[7] However, for simulations that do not include biexciton cascade emission, this behavior is not found. We attribute the similarity in the fast component to the fact that biexciton cascade emission takes place in our simulation at the same timescale in both materials. Therefore, this short time component provides us with an estimate for biexciton lifetimes, which range from 83 ps to 123 ps in the temperature range considered. These biexciton lifetimes are several times shorter than exciton lifetimes, as expected.[10]

Since the presence of biexcitons and the cascade emission process were shown to be important players in the dynamics of the system, a further analysis of this process is, itself, of physical importance. Figure 3 presents the predicted behavior of the biexciton signal in both P6P (top) and 6T (bottom) for several temperatures. For the 6T monolayers, the amount of biexcitons that recombine radiatively increases with temperature. This is so because temperature favors exciton migration from P6P to 6T since it increases the efficiency of Förster resonance energy transfer. Naturally, the more the excitons are confined in the 6T monolayers, the more the biexcitons are produced. In P6P, on the other hand, the effect of temperature on the generation of biexcitons is twofold, and hence, the crossing point is observed in the figure. Initially, the higher the temperature, the greater the intensity of biexciton emission, as can be observed

for roughly the first 0.5 ns after photoabsorption. This is also due to the increase in efficiency of the Förster transfer. Later on, the decay of the signal is observed to be faster for higher temperatures. This may be explained by the faster decrease in exciton population in P6P, as exciton migration becomes more intense. Simulations also indicate that biexciton generation is a more efficient process in P6P than it is in 6T. To obtain agreement between experiment and simulations for both the P6P and 6T TRPL curves simultaneously, it was necessary to include a probability for non-radiative Auger recombination. Our results show that the efficiency of biexciton cascade emission in 6T ranges from 30% to 60% of the one in P6P for the 80 K–300 K temperature interval. We attribute this fact to the monolayer morphology of 6T combined with the impossibility of Förster transfer from 6T to P6P, which confines excitons to a very limited space. The curves in Fig. 3 are expected to be found in TRPL measurements that focus on photons emitted with energies below the ones expected from emission from the first excited state of both molecules. This energy difference amounts to the biexciton binding energy which can, therefore, be experimentally determined by finding the energy range in which the signals shown in Fig. 3 are present.

In summary, we show that exciton migration by means of Förster resonance energy transfer alone is insufficient to explain the experimentally observed behavior of TRPL measurements performed in P6P-6T multilayered organic nanofibers. To correct the description, we introduce a model that includes the possibility of a biexciton cascade emission process to take place. This phenomenon is particularly important to reproduce exciton dynamics when exciton concentration and temperatures are high. This can be achieved not only by using high intensity light sources but also by means of the multilayered morphology employed in the experiments. By carefully choosing the materials used in the different layers, it is possible to create regions where excitons remain confined, such as the 6T monolayers of the system we analysed. In this case, biexciton formation may play an important role in the optical properties of the system. We were also able to predict the behavior of the biexciton signal for several temperatures in both materials. For the P6P-6T system, in particular, we accurately described the first 0.5 ns after photoabsorption, which the previous proposed model in the literature fails to do. Our main conclusion that the biexciton picture ought to be considered in organic nanofibers is general and must be taken into account in order to accurately describe the performance of this type of system.
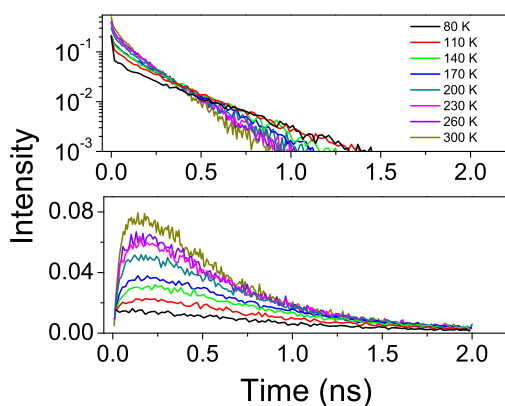

FIG. 3. Predicted time-resolved biexciton PL in P6P (top) and 6T (bottom) for eight temperatures. For P6P, the stimulating photons yield spectra with a different temperature dependence when compared to 6T because of the decrease in exciton population due to exciton migration.

[1]C. Zhang, Y. S. Zhao, and J. Yao, Phys. Chem. Chem. Phys. **13**, 9060 (2011).
[2]F. S. Kim, G. Ren, and S. A. Jenekhe, Chem. Mater. **23**, 682 (2011).

[3]C. Simbrunner, F. Quochi, G. Hernandez-Sosa, M. Oehzelt, R. Resel, G. Hesser, M. Arndt, M. Saba, A. Mura, and G. Bongiovanni, ACS Nano **4**, 6244 (2010).

[4]K. Kranthiraja, S. Kim, C. Lee, K. Gunasekar, V. G. Sree, B. Gautam, K. Gundogdu, S.-H. Jin, and B. J. Kim, Adv. Funct. Mater. **27**, 1701256 (2017).

[5]O. V. Kozlov, Y. N. Luponosov, A. N. Solodukhin, B. Flament, Y. Olivier, R. Lazzaroni, J. Cornil, S. A. Ponomarenko, and M. S. Pshenichnikov, Adv. Opt. Mater. **5**, 1700024 (2017).

[6]A. Serbenta, O. V. Kozlov, G. Portale, P. H. Van Loosdrecht, and M. S. Pshenichnikov, Sci. Rep. **6**, 36236 (2016).

[7]L. Tavares, M. Cadelano, F. Quochi, C. Simbrunner, G. Schwabegger, M. Saba, A. Mura, G. Bongiovanni, D. A. da Silva Filho, and W. F. da Cunha, J. Phys. Chem. C **119**, 15689 (2015).

[8]Y.-M. He, O. Iff, N. Lundt, V. Baumann, M. Davanco, K. Srinivasan, S. Höfling, and C. Schneider, Nat. Commun. **7**, 13409 (2016).

[9]T. Ihara, Phys. Rev. B **93**, 235442 (2016).

[10]X. Huang, Q. Xu, C. Zhang, X. Wang, and M. Xiao, Nano Lett. **16**, 2492 (2016).

[11]F. Pevere, I. Sychugov, F. Sangghaleh, A. Fucikova, and J. Linnros, J. Phys. Chem. C **119**, 7499 (2015).

[12]I. Pelant and J. Valenta, *Luminescence Spectroscopy of Semiconductors* (Oxford University Press, 2012).

[13]A. Köhler and H. Bässler, *Electronic Processes in Organic Semiconductors: An Introduction* (John Wiley & Sons, 2015).

[14]C. Madigan and V. Bulović, Phys. Rev. Lett. **96**, 046404 (2006).

[15]S. R. Yost, E. Hontz, S. Yeganeh, and T. Van Voorhis, J. Phys. Chem. C **116**, 17369 (2012).

[16]J. A. Bjorgaard and M. E. Köse, RSC Adv. **5**, 8432 (2015).

[17]O. V. Mikhnenko, P. W. Blom, and T.-Q. Nguyen, Energy Environ. Sci. **8**, 1867 (2015).

[18]S. M. Menke and R. J. Holmes, J. Mater. Chem. C **4**, 3437 (2016).

[19]E. Kawashima, M. Fujii, and K. Yamashita, Phys. Chem. Chem. Phys. **18**, 26456 (2016).

[20]R. Volpi, S. Kottravel, M. S. Nørby, S. Stafström, and M. Linares, J. Chem. Theory Comput. **12**, 812 (2016).

[21]R. Volpi, S. Stafström, and M. Linares, J. Chem. Phys. **142**, 094503 (2015).

[22]H. Li and J.-L. Brédas, J. Phys. Chem. Lett. **8**, 2507–2512 (2017).

[23]B. Fisher, J. M. Caruge, D. Zehnder, and M. Bawendi, Phys. Rev. Lett. **94**, 087403 (2005).

[24]A. Savitzky and M. J. E. Golay, Anal. Chem. **36**, 1627 (1964).

Article 5

Modeling temperature dependent singlet exciton dynamics in multilayered organic nanofibers

Leonardo Evaristo de Sousa,[1] Pedro Henrique de Oliveira Neto,[1] Jakob Kjelstrup-Hansen,[2] and Demétrio Antônio da Silva Filho[1,a)]

[1]*Institute of Physics, University of Brasilia, 70919-970 Brasilia, Brazil*
[2]*NanoSYD, Mads Clausen Institute, University of Southern Denmark, Sønderborg, Denmark*

Organic nanofibers have shown potential for application in optoelectronic devices because of the tunability of their optical properties. These properties are influenced by the electronic structure of the molecules that compose the nanofibers and also by the behavior of the excitons generated in the material. Exciton diffusion by means of Förster resonance energy transfer is responsible, for instance, for the change with temperature of colors in the light emitted by systems composed of different types of nanofibers. To study in detail this mechanism, we model temperature dependent singlet exciton dynamics in multilayered organic nanofibers. By simulating absorption and emission spectra, the possible Förster transitions are identified. Then, a kinetic Monte Carlo model is employed in combination with a genetic algorithm to theoretically reproduce time-resolved photoluminescence measurements for several temperatures. This procedure allows for the obtainment of different information regarding exciton diffusion in such a system, including temperature effects on the Förster transfer efficiency and the activation energy of the Förster mechanism. The method is general and may be employed for different systems where exciton diffusion plays a role. *Published by AIP Publishing.*
https://doi.org/10.1063/1.5024388

I. INTRODUCTION

The study of organic nanofibers has received attention for its potential applications in optoelectronic devices.[1,2] In particular, the combination of different molecular species to produce multilayered organic nanofiber structures allows for the tuning of the optical properties of such devices.[3] Among the molecules often employed in this kind of study, two stand out for their capacity of self-assembling into nanofibers: *para*-hexaphenyl (P6P) and α-sexithiophene (6T).[4–8]

In different materials, time-resolved photoluminescence (PL) measurements allow for the probing of exciton dynamics. In P6P/6T multilayered nanofibers, experimental results[4] show that exciton diffusion increases with temperature, changing the optical properties of the system significantly. This feature results from exciton migration from one material to the other. The understanding of this process is therefore fundamental to the rational design of such devices.

In organic materials, excitons are usually fairly localized,[9] which results in their diffusion occurring in a regime of incoherent energy transfer, that is, by means of hopping. For singlet excitons, the dominant mechanism of exciton migration is the Förster resonance energy transfer.[10–12] In this mechanism, excitation energy is transferred nonradiatively from molecule to molecule provided there is overlap between the emission and absorption spectra of the donor and acceptor species, respectively.

From a theoretical standpoint, exciton diffusion has been studied by means of Kinetic Monte Carlo (KMC) methods.[10,13–17] These methods require the probabilities of the Förster transfers as input.

As shown below, the efficiency of Förster transfer depends on different aspects such as the amount of overlap between the emission and absorption spectra of the molecules involved and also on intermolecular distances. Thermal effects also play an important role and may change drastically the diffusion process. However, temperature does not appear explicitly in the expression for Förster transfer. Thus, different strategies have been applied to take it into account, such as considering changes in interaction distances,[15,18] in the Förster radii,[16] in the absorption and emission spectra,[13] or including a Boltzmann factor in the expression for the transfer rate.[19] We rely on a different approach to understand these temperature effects.

In this work, we make use of quantum chemical calculations to identify the possible Förster transfers in and between P6P and 6T. With this information, we use a kinetic Monte Carlo method to simulate time-resolved PL measurements for different temperatures. These are, in turn, compared to the experimental results performed in a system composed of 10 alternating monolayers of 6T (~4 Å of thickness) and thicker (~160 Å) P6P layers.[4] To find the model parameters that better reproduce the physical picture and understand the effects of temperature in exciton diffusion, we use a genetic algorithm (GA)[20–24] that approximates simulated time-resolved PL curves to experimental ones.

---

a)Electronic mail: dasf@unb.br

The method used here allows for the understanding of how the relevant physical parameters change with temperature. Simulation results provide us, then, with information on several aspects of the exciton diffusion process. Here, from these time-resolved PL curves alone, we manage to calculate the temperature dependence of the Förster radius in P6P and the activation energy for the Förster mechanism. We also estimate the probability of non-radiative Auger recombination in 6T monolayers and the maximum distance traveled by excitons that migrate from P6P to 6T. Our results match experimental data, showing that the method is sound. This combination of experimental measurements and our method of computational analysis provides better understanding of the physical processes involved and can be applied to several other systems of interest.

II. METHODS

A. Förster resonance energy transfer

The rate of Förster excitation energy transfer varies with the inverse sixth power of the interaction distance between molecules and is given by[25]

$$k_F(d) = \frac{9c^4\kappa^2}{8\pi n d^6} \int_0^\infty \frac{d\omega}{\omega^4} I_D(\omega)\alpha_A(\omega), \qquad (1)$$

where ω is the angular frequency, c is the speed of light, n is the refractive index of the medium, and κ is a factor ranging from 0 to 2, which depends on the orientation between donor and acceptor dipole moments. The integral represents the overlap between the emission spectrum of the donor (I_D) and the absorption spectrum of the acceptor molecule (α_A).

The Förster radius (R_F) is defined as the distance for which the transfer rate is equal to the emission rate of the donor species ($k_{emi} = 1/\tau_D^0$), i.e., as

$$R_F^6 = \tau_D^0 \frac{9c^4\kappa^2}{8\pi n} \int_0^\infty \frac{d\omega}{\omega^4} I_D(\omega)\alpha_A(\omega). \qquad (2)$$

This allows the Förster transfer rate to be written in a simpler form as

$$k_F(d) = \frac{1}{\tau_D^0}\left(\frac{R_F}{d}\right)^6. \qquad (3)$$

The efficiency of this process is given by the ratio between the Förster rate and the sum of the Förster and the donor emission rates. Considering the Förster transfer as the main non-radiative pathway, the recombination probability is given by[26]

$$\Phi(d) = \frac{1}{1 + \left(\frac{d}{R_F}\right)^6} \qquad (4)$$

in which d is the distance between molecules.

B. Spectra simulations

To perform the spectra simulations, the ground state (S_0) and first excited state (S_1) optimized geometries of P6P and 6T were obtained by means of density functional theory (DFT) and time-dependent density functional theory (TD-DFT),

respectively. Frequency calculations were performed to ensure that the structures obtained in the previous calculations corresponded indeed to equilibrium geometries.

The CAM-B3LYP[27] and M062X[28] functionals were used along with the 6-31G(d, p) basis set. These functionals were chosen given their good track record in describing the spectroscopic properties of organic systems.[29–34] The Gaussian09[35] software suite was employed in all DFT and TD-DFT calculations.

A common technique used for spectrum simulations employs the Franck-Condon (FC) approximation. However, in molecules like P6P and 6T that suffer considerable changes in geometry when going from the ground to excited states, the FC approximation becomes unreliable and different methods are required.[36] To avoid this problem, we use the nuclear ensemble method[37] as implemented in the Newton-X[38] software. In this method for spectrum simulations, several non-equilibrium geometries are sampled from a probability distribution for a set of harmonic oscillators followed by single point TD-DFT calculations. Optimized geometries and normal modes for both S_0 and S_1 states are required as input to calculate absorption cross sections and emission rates with this method.

The absorption spectra took into account transitions from the ground state up to the third excited state, whereas emission spectra were calculated for transitions from the first excited state. The results are averaged to produce the final spectrum. A total of 500 geometries were sampled for each case. Gaussian line shapes were used in all simulations with a broadening factor of $\delta = 0.05$ eV.

C. The kinetic Monte Carlo model

The model begins by reproducing the system's morphology used in the experimental study,[4] that is, 10 alternating layers of P6P and 6T. This is done by creating a matrix whose first column corresponds to the 6T monolayer followed by a number L of columns representing the number of P6P monolayers that compose the actual P6P layer (Fig. 1).
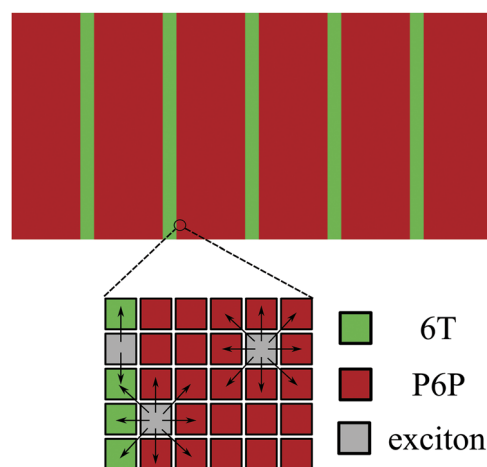

FIG. 1. Schematics of the multilayered system. In detail, the cells corresponding to each matrix entry that represents either the P6P or 6T portions of the system. As explained in the text, excitons in P6P may hop in every direction, whereas excitons in 6T may only hop to other 6T sites.

This arrangement is repeated 10 times and the number of lines in this matrix is set arbitrarily to 100, producing a $100 \times 10(L + 1)$ matrix. Each cell in this matrix is identified as being either composed of P6P or 6T. The multilayered structure of the system allows for the two-dimensional treatment used here.

Next, a number of excitons are generated randomly in the P6P layers, simulating the absorption of light by this material. The amount of excitons created is $N_{ex} = \rho_{ex}1000\,L$, where ρ_{ex} is the exciton concentration and 1000 L is the number of P6P cells in the model.

Once the excitons are generated, a simulation round starts. For each exciton, a two-step process defines whether it hops to a nearby cell, stays put, or recombines. In the first step, the program decides randomly with which of 9 cells the Förster transfer is going to be attempted. These 9 cells are the 8 first neighbors of the exciton in question plus the very cell where the exciton stands.

The probability of a cell being chosen was made proportional to the Förster rate of the intended transition [Eq. (3)]. The rate is calculated for each neighbor and divided by the sum of the calculated rates to compute probabilities. A random number is then generated to select the cell with which the Förster transfer is going to be attempted. In the second step, the program uses Eq. (4) to decide whether the exciton is transferred to the nearby cell or recombines. To do so, values of the distance to Förster radius ratios in P6P (P6P d/R_F) and in 6T (6T d/R_F) must be set as input to the model. This procedure is repeated for every exciton in the simulation after which the time step is increased by one unit.

The time it takes for an exciton to hop may be estimated as the inverse of its Förster rate ($t_{hop} = 1/k_F$). To take into account the fact that the transition rates k_F are different for each pair of materials, two measures are employed. First, the time step unit of the simulation is taken as the inverse of the largest Förster rate possible [$t_{step} = \min(t_{hop})$]. Second, at every time step, each exciton is tested for hopping only if a randomly generated number from 0 to 1 is less or equal to the ratio t_{step}/t_{hop}, where t_{hop} is the time it takes for hopping in the material where the exciton is. This ensures that the speed of the excitons in the different materials will be consistent.

Exciton-exciton interaction is also taken into account. In a previous work, we showed that for this type of system, it is necessary to consider the possibility of biexciton cascade emission to correctly reproduce the behavior of PL measurements in the first 0.5 ns after photoabsorption.[39] Biexciton cascade emission is a two-step process in which a low energy photon is emitted stimulating the emission of a second photon, this one with an energy corresponding to the excited state of the molecule. To include this effect, excitons that hop to the same site form biexcitons and recombine promptly. The amount of biexcitons generated in a simulation depends on exciton concentration. However, a non-radiative mechanism for biexciton recombination also exists, an Auger process in which the exciton's energy is transferred to electrons or holes in a kinetic form.[40,41] To take this possibility into account, a probability of biexciton cascade emission in 6T (P_{XX}) is included as a parameter to the simulation. In this way, this probability controls whether excitons that collide in the 6T portion of the system form biexcitons or annihilate each other non-radiatively.

Finally, when an exciton recombines, either by means of biexciton cascade emission or by regular recombination, the time of the event and the material where recombination occurred are registered. The simulation round ends either after all excitons have recombined or after the maximum time step has been reached. To improve the reliability of the results, this process is repeated several times and the results are added over.

Five parameters are needed to generate the time-resolved photoluminescence spectra: L, ρ_{ex}, P6P d/R_F, 6T d/R_F, and P_{XX}. By means of a genetic algorithm that compares our simulated spectra to the experimental ones, these parameters will be obtained for different temperatures.

D. The genetic algorithm

In order to obtain the best values for the five parameters, we took advantage of the results of time-resolved photoluminescence measurements performed at several different temperatures.[4]

In the genetic algorithm, the five parameters of the model (L, ρ_{ex}, P6P d/R_F, 6T d/R_F, P_{XX}) are the genes. We evaluate the "fitness" of our simulations quantitatively by calculating the root mean squared deviation between the simulated curve and the experimental one. To improve this evaluation, we add the root mean squared deviation between the derivative of the simulated and experimental curves. To smooth the data, a Savitzky-Golay filter[42] was applied to all curves. The genetic algorithm searches for the set of parameters that minimize this fitness function.

The process begins by randomly selecting N individuals, that is, N sets of genes. A simulation is then run for each set, after which the results are evaluated using the fitness function. These results are ordered from best to worst and the first S individuals are selected as survivors, their genes being used to produce a next generation of individuals.

The next generation is chosen in two steps. First, two of the surviving individuals are randomly selected as progenitors. The chance of an individual being chosen as a progenitor is inversely proportional to the fitness function, such that the closer the function is to zero, the higher the probability of this individual being chosen. Second, the new genes are selected randomly from a Gaussian distribution whose mean is the average between the corresponding genes from the progenitors and whose standard deviation is inserted by hand. This standard deviation controls how deterministic the gene selection is or, in other words, controls the effects of mutation in the production of a new individual. Care must be taken in choosing this number because, in one hand, a very high value of standard deviation may reduce significantly the correlation between progenitors and offspring, resulting in a mere random search for the configuration that minimizes the fitness function. On the other hand, a much too low standard deviation makes the optimization procedure too dependent on the initial sampling, eventually preventing the algorithm from exploring certain areas in the space of configurations. In this work, we set the standard deviation as 0.05 times the mean of the parameter in question.

The genetic algorithm was run for eight temperatures ranging from 80 K to 300 K. An initial generation of 10 individuals was created with d/R_F ratios randomly selected from 0.2 to 1.2 and exciton concentrations going from 0.001 to 0.01. The number of P6P monolayers and P_{XX} were also randomly selected from a 10 to 40 interval and from a 0.01 to 0.9 interval, respectively. Each subsequent generation of 10 individuals was created from crossings between the five best simulations obtained at that point. The algorithm ran for 40 generations. Each simulation was run with a total of 100 000 excitons.

III. RESULTS AND DISCUSSION

Figure 2 shows the overlap between the absorption and emission spectra for every possible donor-acceptor (D-A) pairing of P6P and 6T. Absorption and emission spectra are shown in black and blue, respectively. It can be seen that exciton diffusion by means of Förster transfer is possible within P6P and 6T individually and also from P6P to 6T, but not the other way around since the Förster radius, in this case, is zero, as there is no overlap between the emission spectrum of 6T and the absorption spectrum of P6P. Therefore, once excitons migrate from P6P to the 6T layer, their diffusion is limited to this region, that is, they become confined in the 6T layer until recombination occurs. This fact points to the importance of considering exciton interactions and justifies our more detailed treatment of biexciton formation in this material, as this confined region is likely to present high exciton concentration.

Calculating the Förster radius from these spectra shows that the rate of Förster transfer from P6P to 6T is an order of magnitude larger than for the other possible cases. Thus, the hopping time for this transfer is an order of magnitude shorter than for the other two since the Förster radius for this transition is much larger. For simplicity, the time step of the simulation was chosen then to be the lowest between the hopping time for the P6P-P6P and 6T-6T transfers. The P6P to 6T transfer probability was then set to 100% and was considered to take as long as the time step of the simulation. This approximation should not affect the results considerably since the number of P6P-6T transfers is much lower than the other two kinds given the layered structure of the system.

With the information obtained from the spectra, it is possible to start running simulations for this system. Figure 3 shows an example of configuration space explored by the genetic algorithm as it searches for the correct set of parameters that better reproduce the experimental results. Since there are five parameters in the model, it is not possible to visualize them simultaneously. Figure 3 shows the configuration space for the 300 K case with $\rho_{ex} = 0.007$ and $L = 16$. Cold colors represent simulations in closer agreement with experimental results. The top figure presents how the quality of the simulations varies with the d/R_F ratio for P6P and 6T. It can be seen that the ratio for P6P is more determinant to the quality of the simulations, with the best results (blue regions) obtained with a P6P d/R_F value between 0.44 and 0.45. The simulations seem to be less sensitive to changes in the 6T d/R_F ratio. For 300 K, the blue region extends for 6T ratios ranging from 0.38 to 0.48. With this in mind, Fig. 3, bottom, shows the quality of the simulated 6T time-resolved PL curves in terms of the P_{XX} and 6T d/R_F ratio for a P6P d/R_F ratio of 0.45. Results show an optimal region for P_{XX} values around 0.35 and d/R_F
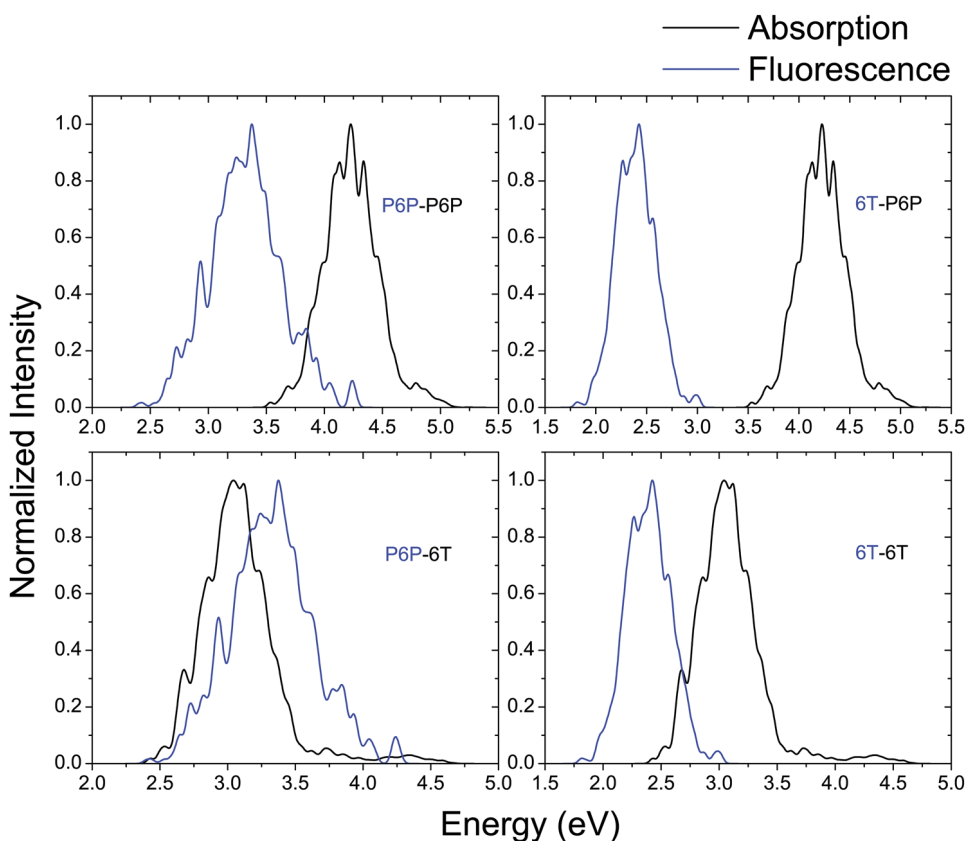

FIG. 2. Absorption (black) and emission (blue) spectra for each donor-acceptor pairing of P6P and 6T calculated with the M062X functional. Only the D-A combination of P6P-6T does not allow Förster transfer. CAM-B3LYP simulations show similar results.
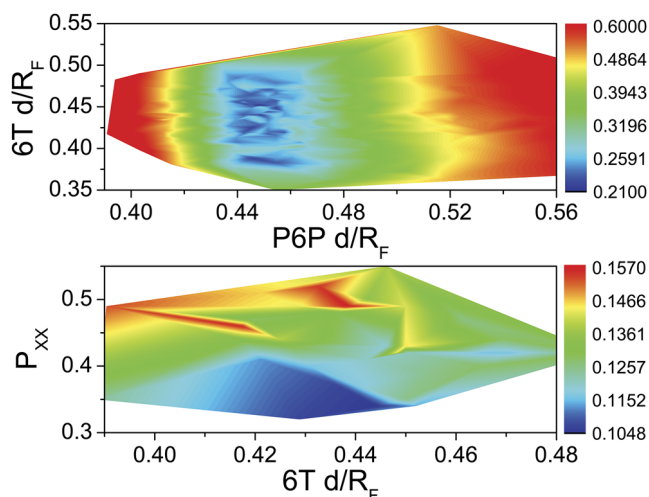
FIG. 3. Heat maps showing the configuration space for simulations performed with $L = 16$, $\rho_{ex} = 0.007$ at 300 K. Colder colors show the combination of parameters that best reproduce experimental results. Top: Configuration space for different values of the d/R_F ratio for both materials. Bottom: Configuration space for the 6T PL curve in terms of the 6T d/R_F ratio and P_{XX} with P6P d/R_F fixed at 0.45.

ratio for 6T around 0.42. The complex landscape of the configuration space justifies the necessity of a method such as the genetic algorithm in looking for the optimal parameters of the simulation.

These optimal parameters found by the genetic algorithm are shown in Fig. 4. Figure 4, top, shows the probability of cascade emission in 6T (P_{XX}) and intermolecular distances in P6P as a function of temperature. The values of P_{XX} do not change considerably with temperature, staying around 0.4. This indicates that the Auger process is temperature insensitive and responsible for as much as 60% of biexciton recombination in 6T. As to the intermolecular distances in P6P, these were estimated by dividing the thickness of the P6P layers (163 Å[4]) by the optimal number of P6P monolayers obtained by the genetic algorithm. This distance is found to be around 10 Å, with an optimal number of P6P monolayers of 16 in most cases, except for the 260 K and 300 K temperatures, for which

this number was 17. The difference is, however, negligible. It is worth noting that the genetic algorithm obtained similar values of intermolecular distances in P6P independently, which points to the reliability of the method.

In Fig. 4, bottom, the ratios between intermolecular distance and Förster radii are shown for both materials. In P6P, an increase in temperature produces a large drop in the d_{P6P}/R_F ratio, indicating an increase in the efficiency of Förster transfer. In 6T, on the other hand, this ratio remains practically constant for all temperatures. This difference in temperature sensitivity in both materials is in agreement with experimental results.[4]

Once the optimal parameters are found, we may plot the corresponding simulated time-resolved PL spectra. These spectra obtained from the optimal parameters show that exciton decay becomes faster with temperature, as more excitons migrate from the P6P to 6T layers. This results in a greater amount of excitons recombining in the 6T layers, which is responsible for the observed change in emitted color. The simulated time-resolved PL can be seen in Fig. 5 and match experimental results well.[4]

These time-resolved spectra may provide information on different aspects of the process. For instance, calculating the ratio between the number of excitons that recombine in the 6T layers and the number of excitons per P6P monolayer in the simulations and dividing this number by 18, the number of P6P/6T interfaces, we obtain the number of P6P monolayers from which excitons migrate to the 6T portion of the system. This number ranges from 2 to 4 P6P monolayers as temperature increases from 80 K to 300 K. This indicates that excitons generated at distances from 20 Å to 40 Å from the interfaces are drained to the 6T layers. This implies that similar experiments performed with P6P layers of thickness around 40 Å should show practically no emission from the P6P portion of the system.

Furthermore, by combining the results obtained for the d_{P6P}/R_F ratio and for the P6P intermolecular distance (Fig. 4), it is possible to calculate the Förster radius for different temperatures in this material. Figure 6 shows that the Förster radius in P6P increases significantly with temperature. This behavior is responsible for the substantial increase in exciton migration

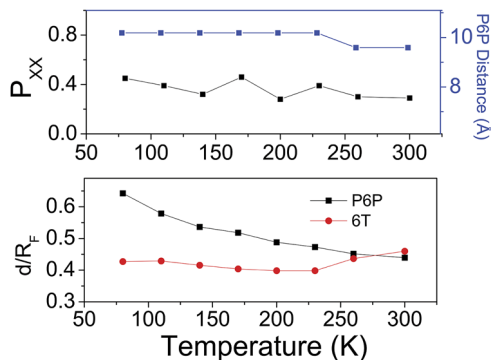

FIG. 4. Optimal parameters obtained by the genetic algorithm. Top: Biexciton probability in 6T (P_{XX}, black) and P6P intermolecular distance (blue) show virtually constant values for all temperatures. Bottom: d/R_F ratio for P6P (black squares) and 6T (red circles). The ratio in 6T remains practically constant, whereas in P6P it decays with temperature, showing an increase in Förster transfer efficiency in this material.
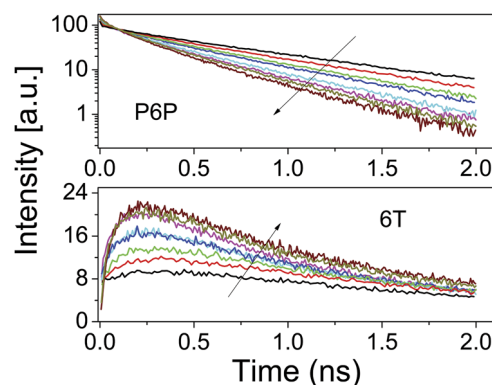

FIG. 5. Simulated time-resolved PL curves for P6P (top) and 6T (bottom) for different temperatures with the parameters obtained with the genetic algorithm. Arrows represent the direction of increasing temperature, from 80 K to 300 K. Results reproduce the experimental behavior of the PL spectra in the whole temperature range.
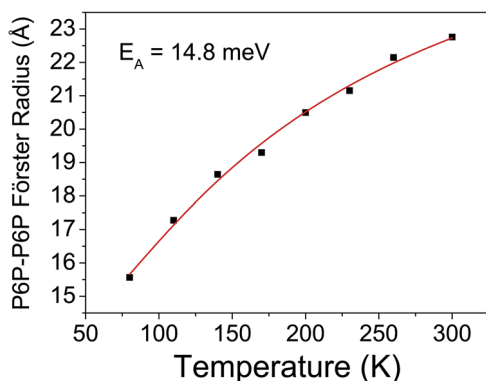
FIG. 6. Förster radius for the P6P/P6P transfer as a function of temperature. The line shows an exponential fit of the data with an activation energy of 14.8 meV.

from the P6P to the 6T layers which is observed experimentally. The curve in Fig. 6 is the result of fitting the data with the function

$$R_F(T) = R_0 + R_1 \exp\left(-\frac{E_A}{kT}\right), \tag{5}$$

with $R_0 = 13.8$ Å, $R_1 = 15.8$ Å, and $E_A = 14.8$ meV. R_0 corresponds to the Förster radius at 0 K, whereas $R_0 + R_1$ corresponds to the maximum radius, obtained in the $T \to \infty$ limit. Finally, we interpret E_A as the activation energy of Förster transfer in P6P. The value of 14.8 meV is close to the experimentally obtained value of 19 meV.[4] It is important to notice that the Förster radius in 6T presents a different behavior, remaining constant for all temperatures considered since the d_{6T}/R_F ratio remains mostly constant. This is in agreement with a previous study that found exciton diffusion in 6T to be temperature independent.[43] Furthermore, it has been noted that not all materials present a Boltzmann dependence of Förster radius with temperature as it is often assumed.[13] The method presented here allows for the obtainment of the correct temperature dependence without resorting to any functional form *a priori*.

IV. CONCLUSIONS

In this work, a combination of *ab initio* methods, kinetic Monte Carlo, and genetic algorithms was employed to simulate exciton dynamics in a system composed of alternating layers of P6P and 6T. DFT calculations and the nuclear ensemble method were used to calculate the absorption and emission spectra of both molecules. With these spectra, it was determined that Förster transfer is possible within P6P and 6T and also from P6P to 6T, but not the other way around. This means that excitons that migrate to the 6T layers become confined there until recombination.

With a kinetic Monte Carlo model, exciton diffusion was investigated. In this model, excitons are allowed to hop with certain probabilities. When Förster transfer fails, the exciton recombines and the time at which this happens, as well as the material where recombinations take place, is registered, which allows for the reproduction of time-resolved photoluminescence measurements. Exciton interactions are also

included in the form of biexciton formation. These biexcitons are allowed to recombine either radiatively, by means of a cascade emission process, or non-radiatively, through an Auger process.

The simulated measurements are then compared to the experimental ones for various temperatures. The genetic algorithm comes in as a key tool to find the parameters that better reproduce the experimental results. Analysis of the optimal parameters allows for the estimation of intermolecular distances in P6P. It also indicates that the Auger process that takes place in the 6T layers is temperature independent and accounts for around 60% of biexciton recombination. Furthermore, results show that the Förster radius in P6P increases exponentially with temperature, with an activation energy of 14.8 meV. This is responsible for the large increase with temperature in exciton migration from P6P to 6T layers. In addition, P6P presents a greater sensitivity to temperature changes, as evidenced by the fact that the efficiency of Förster transfer in 6T remains practically constant.

Simulations run with the obtained temperature dependence show good agreement with the experimental results. The simulated time-resolved photoluminescence measurements show the decrease in intensity of light emitted from the P6P material with a corresponding increase in light emitted from 6T as temperature is increased from 80 K to 300 K. Light emission in 6T reaches a maximum value before decaying exponentially, as it takes time for excitons to migrate from one material to the other. A closer look at exciton density in the P6P/6T interface shows how the excitons are drained from the P6P monolayers adjacent to the 6T one as the Förster radius for the P6P to 6T transfer is very high. Meanwhile, excitons in P6P monolayers farther from the interface diffuse only in the P6P portion and are responsible for the emission of light in this region. As temperature increases, P6P monolayers farther from the interface are also drained, increasing the emission of light from 6T. We estimate this number of P6P monolayers that contribute with excitons to 6T to range from 2 to 4, which translates into distances from 20 Å to 40 Å.

The combination of methods employed here allows for the inclusion of temperature effects to exciton dynamics directly from experimental results. The model is also capable of reproducing experimental measurements and provides information on different aspects of the process of exciton diffusion. These results show that the method may be used as a tool to improve device design and better understand its functioning. It may also be employed to simulate exciton dynamics in different materials and with different morphologies.

[1]C. Zhang, Y. S. Zhao, and J. Yao, Phys. Chem. Chem. Phys. **13**, 9060 (2011).
[2]F. S. Kim, G. Ren, and S. A. Jenekhe, Chem. Mater. **23**, 682 (2010).

[3] C. Simbrunner, F. Quochi, G. Hernandez-Sosa, M. Oehzelt, R. Resel, G. Hesser, M. Arndt, M. Saba, A. Mura, and G. Bongiovanni, ACS Nano **4**, 6244 (2010).

[4] L. Tavares, M. Cadelano, F. Quochi, C. Simbrunner, G. Schwabegger, M. Saba, A. Mura, G. Bongiovanni, D. A. da Silva Filho, and W. F. da Cunha, J. Phys. Chem. C **119**, 15689 (2015).

[5] C. Simbrunner, G. Hernandez-Sosa, F. Quochi, G. Schwabegger, C. Botta, M. Oehzelt, I. Salzmann, T. Djuric, A. Neuhold, and R. Resel, ACS Nano **6**, 4629 (2012).

[6] L. Kankate, F. Balzer, H. Niehus, and H.-G. Rubahn, Thin Solid Films **518**, 130 (2009).

[7] M. Schiek, F. Balzer, K. Al-Shamery, A. Lützen, and H.-G. Rubahn, J. Phys. Chem. C **113**, 9601 (2009).

[8] J. Kjelstrup-Hansen, J. E. Norton, D. A. da Silva Filho, J.-L. Brédas, and H.-G. Rubahn, Org. Electron. **10**, 1228 (2009).

[9] P. H. de Oliveira Neto, D. A. da Silva Filho, W. F. da Cunha, P. H. Acioli, and G. M. e Silva, J. Phys. Chem. C **119**, 19654 (2015).

[10] S. R. Yost, E. Hontz, S. Yeganeh, and T. Van Voorhis, J. Phys. Chem. C **116**, 17369 (2012).

[11] T. Förster, Ann. phys. **437**, 55 (1948).

[12] T. Förster, Discuss. Faraday Soc. **27**, 7 (1959).

[13] C. Madigan and V. Bulović, Phys. Rev. Lett. **96** 046404 (2006).

[14] J. A. Bjorgaard and M. E. Köse, RSC Adv. **5**, 8432 (2015).

[15] O. V. Mikhnenko, P. W. Blom, and T.-Q. Nguyen, Energy Environ. Sci. **8**, 1867 (2015).

[16] S. M. Menke and R. J. Holmes, J. Mater. Chem. C **4**, 3437 (2016).

[17] E. Kawashima, M. Fujii, and K. Yamashita, Phys. Chem. Chem. Phys. **18**, 26456 (2016).

[18] H. Bässler, Phys. Status Solidi B **175**, 15 (1993).

[19] K. Feron, W. J. Belcher, C. J. Fell, and P. C. Dastoor, Int. J. Mol. Sci. **13**, 17019 (2012).

[20] L. A. Ribeiro, P. H. de Oliveira Neto, W. F. da Cunha, R. Gargano, and G. M. e Silva, Chem. Phys. Lett. **555**, 168 (2013).

[21] S. Nandy, P. Chaudhury, and S. Bhattacharyya, J. Chem. Phys. **132**, 234104 (2010).

[22] J. Xu, H.-L. Zhou, Z. Chen, and C.-D. Lin, Phys. Rev. A **79**, 052508 (2009).

[23] L. F. Roncaratti, R. Gargano, and G. M. e Silva, J. Mol. Struct.: THEOCHEM **769**, 47 (2006).

[24] W. Ferreira Da Cunha, L. F. Roncaratti, R. Gargano, E. Silva, and G. Magela, Int. J. Quantum Chem. **106**, 2650 (2006).

[25] V. May and K. Oliver, *Charge and Energy Transfer Dynamics in Molecular Systems* (John Wiley & Sons, 2008).

[26] A. Köhler and H. Bässler, *Electronic Processes in Organic Semiconductors: An Introduction* (John Wiley & Sons, 2015).

[27] T. Yanai, D. P. Tew, and N. C. Handy, Chem. Phys. Lett. **393**, 51 (2004).

[28] Y. Zhao and D. G. Truhlar, Theor. Chem. Acc. **120**, 215 (2008).

[29] D. Lumpi, E. Horkel, F. Plasser, H. Lischka, and J. Fröhlich, ChemPhysChem **14**, 1016 (2013).

[30] A. Charaf-Eddin, A. Planchat, B. Mennucci, C. Adamo, and D. Jacquemin, J. Chem. Theory Comput. **9**, 2749 (2013).

[31] D. Jacquemin, A. Planchat, C. Adamo, and B. Mennucci, J. Chem. Theory Comput. **8**, 2359 (2012).

[32] I. T. Lima, C. Risko, S. G. Aziz, D. A. da Silva Filho, and J.-L. Brédas, J. Mater. Chem. C **2**, 8873 (2014).

[33] M. M. Oliva, T. M. Pappenfus, J. H. Melby, K. M. Schwaderer, J. C. Johnson, K. A. McGee, D. A. da Silva Filho, J.-L. Bredas, J. Casado, and J. T. López Navarrete, Chem.-A Eur. J. **16**, 6866 (2010).

[34] D. A. da Silva Filho, R. Friedlein, V. Coropceanu, G. Ohrwall, W. Osikowicz, C. Suess, S. L. Sorensen, S. Svensson, W. R. Salaneck, and J.-L. Bredas, Chem. Commun. **0**(15), 1702 (2004).

[35] M. J. Frisch, G. W. Trucks, H. B. Schlegel, G. E. Scuseria, M. A. Robb, J. R. Cheeseman, G. Scalmani, V. Barone, B. Mennucci, G. A. Petersson, H. Nakatsuji, M. Caricato, X. Li, H. P. Hratchian, A. F. Izmaylov, J. Bloino, G. Zheng, J. L. Sonnenberg, M. Hada, M. Ehara, K. Toyota, R. Fukuda, J. Hasegawa, M. Ishida, T. Nakajima, Y. Honda, O. Kitao, H. Nakai, T. Vreven, J. A. Montgomery, Jr., J. E. Peralta, F. Ogliaro, M. Bearpark, J. J. Heyd, E. Brothers, K. N. Kudin, V. N. Staroverov, R. Kobayashi, J. Normand, K. Raghavachari, A. Rendell, J. C. Burant, S. S. Iyengar, J. Tomasi, M. Cossi, N. Rega, J. M. Millam, M. Klene, J. E. Knox, J. B. Cross, V. Bakken, C. Adamo, J. Jaramillo, R. Gomperts, R. E. Stratmann, O. Yazyev, A. J. Austin, R. Cammi, C. Pomelli, J. W. Ochterski, R. L. Martin, K. Morokuma, V. G. Zakrzewski, G. A. Voth, P. Salvador, J. J. Dannenberg, S. Dapprich, A. D. Daniels, O. Farkas, J. B. Foresman, J. V. Ortiz, J. Cioslowski, and D. J. Fox, GAUSSIAN 09, Revision C.01, Gaussian, Inc., Wallingford, CT, 2009.

[36] L. E. de Sousa, L. A. Ribeiro, A. L. de Almeida Fonseca, and D. A. da Silva Filho, J. Phys. Chem. A **120**, 5380 (2016).

[37] R. Crespo-Otero and M. Barbatti, Theor. Chem. Acc. **131**, 1237 (2012).

[38] M. Barbatti, M. Ruckenbauer, F. Plasser, J. Pittner, G. Granucci, M. Persico, and H. Lischka, Wiley Interdiscip. Rev.: Comput. Mol. Sci. **4**, 26 (2014).

[39] L. Evaristo de Sousa, W. Ferreira da Cunha, D. Antônio da Silva Filho, and P. H. de Oliveira Neto, Appl. Phys. Lett. **112**, 143301 (2018).

[40] X. Huang, Q. Xu, C. Zhang, X. Wang, and M. Xiao, Nano Lett. **16**, 2492 (2016).

[41] F. Pevere, I. Sychugov, F. Sangghaleh, A. Fucikova, and J. Linnros, J. Phys. Chem. C **119**, 7499 (2015).

[42] A. Savitzky and M. J. E. Golay, Anal. Chem. **36**, 1627 (1964).

[43] A. Mani, J. Schoonman, and A. Goossens, J. Phys. Chem. B **109**, 4829 (2005).

Article 6

SCIENTIFIC REPORTS

OPEN

Exciton Diffusion in Organic Nanofibers: A Monte Carlo Study on the Effects of Temperature and Dimensionality

Leonardo Evaristo de Sousa[1], Demétrio Antônio da Silva Filho (ID)[1], Rafael Timóteo de Sousa Jr. (ID)[2] & Pedro Henrique de Oliveira Neto[1]

Organic nanofibers have found various applications in optoelectronic devices. In such devices, exciton diffusion is a major aspect concerning their efficiency. In the case of singlet excitons, Förster transfer is the mechanism responsible for this process. Temperature and morphology are factors known to influence exciton diffusion but are not explicitly considered in the expressions for the Förster rate. In this work, we employ a Kinetic Monte Carlo (KMC) model to investigate singlet exciton diffusion in para-hexaphenyl (P6P) and α-sexithiophene (6T) nanofibers. Building from previous experimental and theoretical studies that managed to obtain temperature dependent values for Förster radii, exciton average lifetimes and intermolecular distances, our model is able to indicate how these parameters translate into diffusion coefficients and diffusion lengths. Our results indicate that these features strongly depend on the coordination number in the material. Furthermore, we show how all these features influence the emitted light color in systems composed of alternating layers of P6P and 6T. Finally, we present evidence that the distribution of exciton displacements may result in overestimation of diffusion lengths in experimental setups.

Exciton diffusion is one of the key processes behind the operation of organic optoelectronic devices[1–3]. In organic photovoltaics, for instance, diffusion is responsible for the arrival of excitons at the interface where charge separation may occur[4,5]. Thus, a long diffusion length may translate into highly performant devices. For this reason, a great interest has been shown in predicting and measuring exciton diffusion length in organic materials[6,7].

Among the materials employed in optoelectronic applications, organic nanofibers have received considerable attention thanks to their capacity to self-assemble and the tunability of their optical properties[8–10]. In particular, para-hexaphenyl (P6P) has been found to crystallize in nanofiber shape with special ease[11,12]. Furthermore, it has been shown that deposition of α-sexithiophene molecules on P6P nanofibers also results in highly crystalline structures[13]. These findings make these two molecular species interesting material in which to investigate exciton diffusion.

The mechanism responsible for singlet exciton diffusion is the Förster resonance energy transfer[14–16]. This is a non-radiative transition that requires the existence of an overlap between the emission and absorption spectra of the donor and acceptor molecules, respectively. The rate of this transfer is given by[16,17]

$$k_F = \frac{1}{\tau_D}\left(\frac{R_F}{r}\right)^6 \tag{1}$$

where τ_D is the radiative lifetime of the donor species, r is the intermolecular distance and R_F is the Förster radius, a characteristic distance for which the Förster transfer rate equals the emission rate of the donor molecule. The above expression is known to overestimate transfer rates when intermolecular distances are similar or inferior to the corresponding transition dipole[18]. In the 1 nm range, which is the minimum intermolecular distance we consider here, these issues are mitigated.

[1]Institute of Physics, University of Brasília, 70.919-970, Brasília, Brazil. [2]Department of Electrical Engineering, University of Brasília, 70.919-970, Brasília, Brazil. Correspondence and requests for materials should be addressed to D.A.d.S.F. (email: dasf@unb.br)

1

When decay pathways other than exciton recombination are neglected, the probability of Förster transfer may be written as

$$\Phi(r) = \frac{1}{1 + \left(\frac{r}{R_F}\right)^6}$$

(2)

In spite of the simplicity of the above expressions, different features that affect exciton diffusion are not explicitly taken into account. Two such features that are known to play an important role in this process are temperature and morphology[19–22]. To take into account these more complex issues, Kinetic Monte Carlo (KMC) models are often employed in the study of exciton diffusion[7,18,23–26]. These models must be able to calculate Förster rates and probabilities to decide the behavior of each exciton at every step of the simulation. Exciton lifetimes, displacements and speeds are then registered allowing for the calculation of several properties. An analytical approach is also possible in some cases. Diffusion coefficients may be estimated by $R_F^6/\tau r^4$ for the one dimensional case with equal spacing between sites. In the two dimensional case, however, the distances between a site and all its neighbors are not equal. This affects the transfer rates, the recombination probability and ultimately the diffusion length. Furthermore, analytical models are impractical when studying systems composed by more than one material, since the Förster radii are different, resulting in an asymmetry between the possibility of Förster transfers from one material to the other.

When it comes to temperature effects, our previous work that combined experimental results, a KMC model and a genetic algorithm has shown that the average Förster radius in P6P presents a temperature dependence in the 80 K to 300 K temperature range that can be modeled by the following expression[27]:

$$R_F(T) = R_0 + R_1 \exp\left(-\frac{E_A}{kT}\right),$$

(3)

with $R_0 = 13.8$ Å, $R_1 = 15.8$ Å and $E_A = 14.8$ meV. The methodology relied upon experimental time-dependent photoluminescence spectra of P6P to obtain this result. This expression may be interpreted as taking into account two aspects of exciton diffusion: first, an initial downhill migration process that is temperature independent and dominant at low temperatures. In this process, excitons hop towards lower energy sites where they become trapped; second, this process is then combined with a temperature activated behavior that dominates at higher temperatures, resulting in larger exciton diffusion lengths. Such a behavior has been observed for singlet exciton diffusion in polymers, for instance[6].

On the other hand, the same study has also shown that exciton diffusion in 6 T is mainly temperature independent: for an average intermolecular distance of 10 Å, the Förster radius in 6 T can be estimated to be 24 Å for any temperature in the investigated range. This is in agreement with experimental results that found exciton diffusion lengths do not change with temperature[28]. This suggests very low energetic disorder in 6 T, which would prevent the appearance of a temperature activated character in exciton diffusion.

Energetic disorder is therefore taken into account by the behavior of the Förster radii with temperature. Regarding morphology, spatial disorder may also hinder exciton diffusion. In the context of nanofibers, however, this point is less important since the nanofibers tend to align parallel to each other, leading to highly ordered morphologies. But apart from disorder, recent advances in the techniques involved in the growth of these nanofibers have allowed for the production of extremely thin (~4 Å) layers of these materials[29], making for an essentially one-dimensional structure for excitons to diffuse. This points to the need of further investigating dimensionality effects in exciton diffusion.

Here, we investigate temperature and dimensionality effects on singlet exciton diffusion in P6P and 6 T. We employ a KMC model that takes experimental radiative lifetimes[29], the temperature dependent Förster radius (equation 3) and average intermolecular distances[27] to simulate exciton diffusion in one and two dimensional lattices. The KMC model allows us to understand how the changes in morphology and temperature are translated into diffusion coefficients and diffusion lengths. Results show values for these two parameters to be within typical range for organic materials. We also show that dimensionality affects these features significantly and track this effect to an increase in average intermolecular distance that may come with an increase in the coordination number in the lattice structure. We argue that the distribution of exciton displacements may lead to overestimation in exciton diffusion lengths under experimental conditions. Finally, we investigate the effects on exciton lifetime, diffusion length and emission properties in systems composed of one-dimensional 6 T monolayers alternated with thicker P6P layers for several temperatures.

Methods

A KMC model was employed to simulate exciton diffusion in P6P and 6 T nanofibers. Two morphologies were employed: one-dimensional and two-dimensional lattices. These simulated, respectively, exciton diffusion between nanofibers in a single layer and in the bulk. In the one-dimensional case, 1000 sites were considered, whereas in the two-dimensional one, a 100×100 grid was used. These lattice sizes were chosen for being large enough to prevent border effects.

Excitons were randomly generated throughout the grids. At every time step, the program decides with which neighbor the Förster transfer is going to be attempted. The probability of a neighbor being chosen is proportional to the Förster rate of each transfer. Once the neighbor is chosen, a random number is generated and compared to the probability of Förster transfer to decide whether the exciton hops to a nearby site or recombines. When a hop takes place, the simulation time is increased by an amount given by the inverse Förster rate of the chosen transfer. The time in which recombination takes place is registered along with the total displacement of the exciton during
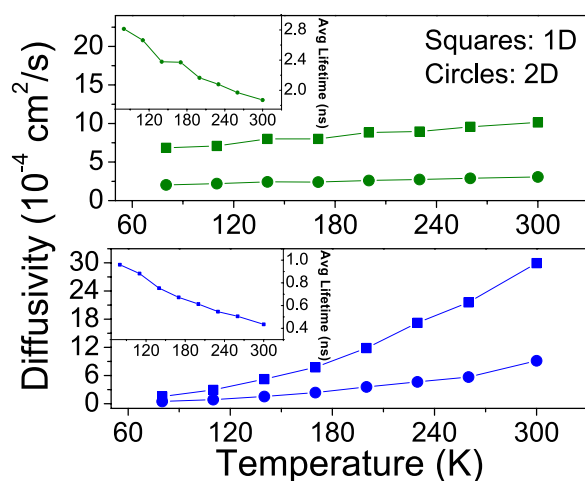
Figure 1. One-dimensional exciton diffusion coefficients as a function of temperature for 6 T (top, green) and P6P (bottom, blue) in the 1D (squares) and 2D (circles) morphologies. Inset: Average exciton lifetimes for different temperatures.

its lifetime. This enables us to obtain the distributions of exciton lifetimes, displacements and speeds. From these data we calculate the corresponding average amounts. Knowledge regarding the position where each exciton recombined also allows for the plotting of emission maps, which show the regions in space where recombination is more common.

To calculate the Förster rates and probabilities, radiative lifetimes, intermolecular distances and Förster radii are required. The latter two were taken from a previous work[27] that showed the temperature dependence of the P6P and 6 T Förster radii and estimated intermolecular distances in these materials. P6P and 6 T radiative lifetimes were obtained from an earlier experimental work[29].

In a first round, simulations were run with 100,000 excitons that had their total displacement and lifetimes registered. These simulations ran until all excitons had recombined. In a second round of simulations, 30,000 excitons had their positions registered at each time step up to 2000 ps. The variance of exciton displacements were evaluated as a function of time. These curves were fitted by straight lines, the slopes of which provide the diffusion constants. In all cases, simulations were performed for 8 temperature values ranging from 80 K to 300 K. Exciton-exciton interactions were not taken into account, so our results refer to exciton diffusion in low concentration regimes, as is often the case in experimental setups.

Results and Discussion

Simulations indicate that singlet excitons are subjected to a normal diffusion process in both morphologies. This is evidenced by the linear relationship between the variance of exciton displacement with time (Fig. 1, SI), which allows us to obtain diffusion coefficients. It is worth noting that even experimental techniques employed to measure diffusion constants and diffusion lengths rely on some form of analytical model for normal diffusion from which these quantities are extracted[6].

It is important to point out that for the 2D case it is possible to find diffusion coefficients in both x and y directions. Since both directions are treated equally, these two one-dimensional coefficients are equal. Figure 1-Top shows the one-dimensional diffusion coefficient in 6 T to increase from $6.9 \times 10^{-4} cm^2/s$ to $10.1 \times 10^{-4} cm^2/s$ in the 1D morphology and from $2.0 \times 10^{-4} cm^2/s$ to $3.1 \times 10^{-4} cm^2/s$ in the 2D one in the temperature range considered. In the case of P6P (Fig. 1-Bottom), the variation of diffusion constant with temperature is larger, ranging from $1.5 \times 10^{-4} cm^2/s$ to $30.0 \times 10^{-4} cm^2/s$ in the 1D morphology and from $0.4 \times 10^{-4} cm^2/s$ to $9.2 \times 10^{-4} cm^2/s$ in the 2D one.

These values are within typical values for organic materials[6]. Diffusivity values show an increase with temperature in spite of decreasing average exciton lifetimes (Fig. 1-Insets). This results from the fact that Förster radii either remains constant (in 6 T) or increases with temperature (in P6P). This goes to show that shifts towards lower energies in the absorption and emission spectra are producing increases with temperature in the overlap integral between both spectra, compensating or even outweighing the reductions in lifetime (Fig. 1-Insets).

Furthermore, an increasing detachment between the diffusivities obtained for both morphologies is observed, particularly in P6P. It is clear that 1D diffusion coefficients obtained for 2D morphologies should be inferior than those encountered in 1D morphologies, typically by a factor of two. However, results show this factor to be larger, even though exciton lifetimes are equal and the morphologies are similarly ordered.

The above mentioned difference also affects exciton diffusion lengths. These may be calculated by means of the equation

$$L_D = \sqrt{ZD\tau},$$

(4)

3
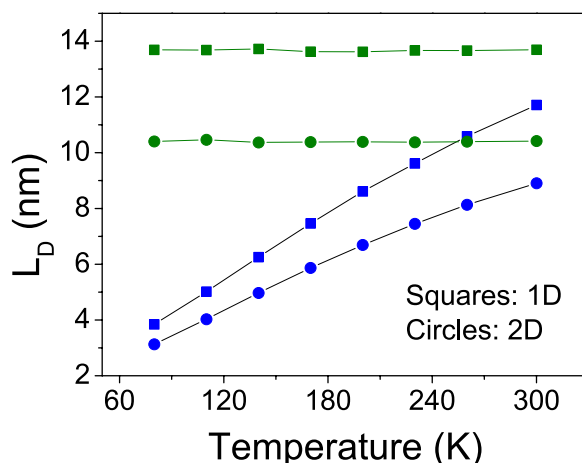
Figure 2. Diffusion lengths in 6 T (green) and P6P (blue) for the 1D (squares) and 2D (circles) morphologies as a function of temperature.

where $Z = 1, 2, 3$ is the dimensionality of the process, D is the diffusion coefficient and τ the average exciton lifetime. In Fig. 2, diffusion lengths for excitons in 6 T (green) and P6P (blue) are shown for the 1D morphology (squares) and for 2D morphologies (circles).

As expected, diffusion length in 6 T remains constant for all temperatures, as its Förster radius does not change. in the case of P6P, however, some features of the diffusion length curves stand out. First, it can be seen that the steep increase in diffusion coefficient observed for the 1D morphology does not translate itself fully to diffusion length. This is the case because of the corresponding large decrease in the average exciton lifetimes, indicating that this characteristic is indeed the main limiting factor to exciton diffusion length as already pointed out in a previous paper[18]. It's worth mention that all the factors that play a role in diffusion length are already coded in the Förster radius, which makes its temperature dependence the determining factor in the behavior of the curves.

A second important feature is the difference between the total diffusion length calculated for the 1D and 2D morphologies. For P6P, the first one ranges from 3.8 nm to 11.4 nm whereas the latter ranges from 3.1 nm to 8.9 nm. In the case of 6 T, 13.8 nm and 10.4 nm, respectively. Interestingly, the difference is very significant even though the Förster radii, average exciton lifetimes and nanofiber spacing are taken to be the same. To understand this effect, we calculate the distribution of exciton speeds in both morphologies (Fig. 2, SI). The calculations show that, at 300 K, not only average speeds decrease from around 300 m/s to 200 m/s in P6P and from 100 m/s to 65 m/s in 6 T when going from the 1D to 2D morphologies but there is also an increase in the standard deviation of the distribution.

In the one dimensional case, an exciton has only two neighbors with which a Förster transfer might be attempted. These neighbors are both situated at a 10 Å distance, resulting in equal hopping probabilities and in a single speed for all excitons. When other layers of P6P are juxtaposed, making for a 2D structure in which excitons may hop, the number of neighboring sites becomes 8. Given the square lattice, 4 of the neighbors (vertical and horizontal) are 10 Å away from the exciton position whereas the other 4 (diagonals) are 14.1 Å away. Because of the inverse sixth power dependence of the Förster rate on intermolecular distances (equation 1), this 41% increase in distance results in an 8 fold reduction in the transfer rate ($(14.1/10)^6 \approx 8$). In spite of this reduction, eventually an exciton will attempt a Förster transfer to a farther site. These transfers take a longer time to be performed and will also present a larger probability of recombination when compared to transfers to closer sites.

Therefore, the results indicate that the mere presence of extra adjacent nanofibers whose distances to the exciton site are larger than that of the closer neighbors, but small enough as to still possess non-negligible Förster rates effectively reduces the exciton's average speed and diffusion length. These results should also apply to molecular crystals, indicating that an increase in coordination number may actually hinder exciton transport.

There are several techniques for measuring exciton diffusion length, the most common being fluorescence quenching in bilayers[6]. This kind of experiment is able to measure one-dimensional diffusion lengths, so it is worth mentioning the one-dimensional projection of the diffusion length calculated for the 2D morphology. This projection was estimated to remain constant at 7.6 nm in 6 T and to range from 2.2 nm to 6.4 nm in P6P, well below the corresponding values obtained for the 1D morphology. Experimental estimates of one-dimensional diffusion length in P6P and 6 T have been obtained using the above mentioned experimental technique[10,28]. The reported values are of 60 nm in 6 T and 30 nm in P6P. These estimations are much higher than the results obtained in our simulations for even the most favorable case, i.e. the 1D morphology.

Given the observed mismatch between the experimental estimation and the simulations, it is worth considering the distribution of one-dimensional absolute displacements for excitons in both morphologies. Figure 3 shows these distributions at 300 K. It can be seen that absolute displacements of around 60 nm in 6 T and 30 nm in P6P correspond to the tail of the distributions. Only 3% and 0.1% of excitons recombine at least 30 nm away form their original positions in the 1D and 2D morphologies, respectively. In the case of 6 T, for a 60 nm distance, these numbers drop to 0.2% and 0.002%, respectively. Importantly, every exciton has a similar probability of recombination
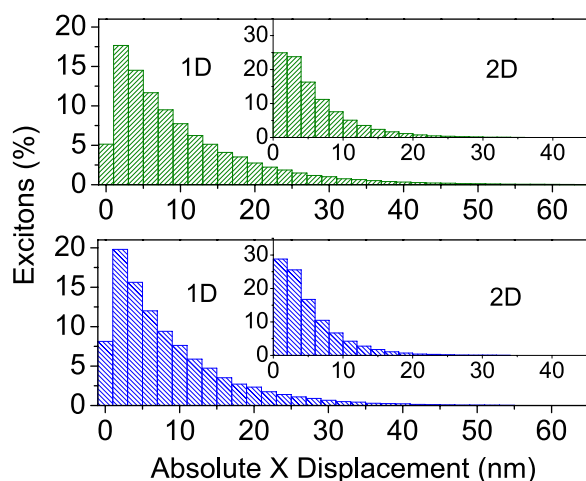
Figure 3. Histograms showing the distribution of absolute displacement in the x axis for excitons at 300 K in 6 T (top) and P6P (bottom) for 1D and 2D (inset) morphologies.
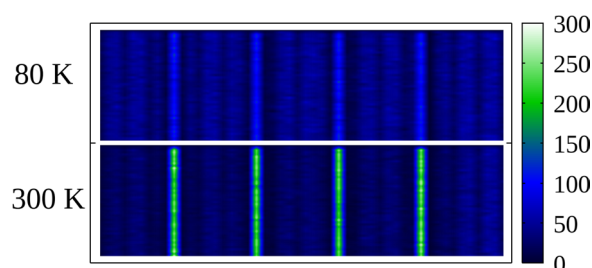

Figure 4. Emission map for singlet excitons in a P6P/6 T alternate layered morphology at 80 K (top) and 300 K (bottom).

regardless of its diffusion length. By chance, some of them live longer than the others, which allows them to reach larger distances. It is also worth noting that in the simulations excitons that may have reached the 30 nm or 60 nm mark could have diffused back, resulting in lower values than would have been observed experimentally, where exciton quenching prevents this return. However, this fact is not enough to explain the large difference between experimental and simulated values. We conclude that these experimental values overestimate singlet exciton diffusion length in both 6 T and P6P–which is by definition an average value–rather pointing to their maximum one-dimensional displacement. It is not to say that there is necessarily a discrepancy between simulation and experiment. It is just that the experiment seems to be measuring the distances covered by a small number of excitons and taking these values to be representative of the average distance an exciton travels.

Finally, we turn to the effects of combining P6P and 6 T nanofibers in a morphology that alternates 6 T monolayers (~4 Å thick) with thicker P6P layers (~160 Å). This setup has been experimentally investigated[10,29] and holds interest for at least two reasons. First, the combination of these two materials results in interesting exciton dynamics. Because of their spectroscopic properties, Förster transfers are possible from P6P to 6 T. Experimental estimates put the Förster radius of this transfer around 36 Å[10]. However, the reversed transfer, from 6 T to P6P, is not allowed[27]. As shown in Fig. 4, which presents the simulated emission maps for excitons in the alternate layered morphology, this results in changes in the emitted color from mainly blue to green as temperature increases. This is the case because diffusion lengths in P6P increase, allowing excitons to reach the interface and migrate towards the 6 T monolayers, changing the proportion of excitons that recombine in both materials.

A second reason of interest in such a system is the combination of two-dimensional–P6P layers–and one-dimensional–6 T monolayers–structures for excitons to diffuse. The effects of temperature on exciton diffusion length and lifetime are shown in Fig. 5. It can be seen that exciton lifetimes decrease from 1.4 ns to 1.3 ns in the 80 K to 300 K range. In this same range, the diffusion length increases from 6.8 nm to 11.2 nm. Interestingly, we note that the average lifetimes present a temperature sensitivity similar to the one in pure 6 T, changing only mildly in the temperature range considered. The reason is that exciton lifetimes are longer in 6 T than in P6P, as shown in the Fig. 1. When an exciton hops from P6P to 6 T, it ends up living longer, pushing average lifetimes as a whole upwards. Meanwhile, diffusion lengths follow the trend seen for pure P6P, with a temperature activated profile. This is expected since in the model excitons are generated in the P6P layers, which are much larger than the 6 T ones.
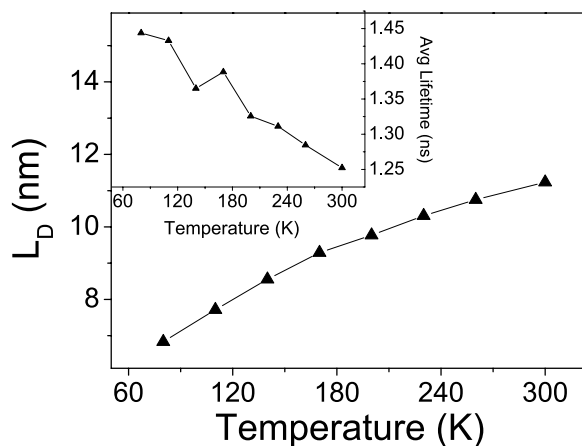
Figure 5. Exciton diffusion lengths in a system composed of alternating layers of P6P and 6 T as a function of temperature. (Inset) Average exciton lifetimes in this system.

Conclusions

In summary, we investigate temperature and dimensionality effects on exciton diffusion in 6 T and P6P nano-fibers. Both materials present different temperature sensitivities, with P6P presenting a temperature activated behavior whereas 6 T shows virtually no temperature dependence. As to dimensionality effects, our results show that exciton diffusion coefficients and diffusion lengths may be considerably affected by the coordination number found in the morphology of the system, particularly if a change in this number actually corresponds to an increase in the average intermolecular distance. We observe that because of this effect, simulations performed in 1D morphologies showed much larger diffusion coefficients and diffusion lengths than their 2D counterparts in spite of otherwise completely equal simulation parameters. We find further that in spite of considerable gains in diffusivity with temperature, diffusion lengths do not follow a similar increase, being offset by decreasing average exciton lifetimes.

We calculate one-dimensional exciton diffusion length in P6P to be around 6 nm at room temperature with a corresponding diffusion constant of $9 \times 10^{-4}\, cm^2/s$. In 6 T monolayers, these parameters are estimated to be 13.7 nm and $10 \times 10^{-4}\, cm^2/s$. These values are within typical values for organic materials. However, comparison between the distribution of exciton displacements with experimental estimates of diffusion length in both 6 T and P6P suggests that the experimental technique estimates maximum exciton displacement rather than diffusion lengths, which are an average quantity. This may result in large overestimation of exciton diffusion lengths. It is also worth noting that exciton-exciton interactions were not taken into account. Since such effects tend to reduce diffusion lengths, our estimates can be seen as upper limits. Thus, the inclusion of these effects in the model would not modify the conclusions we obtained for this paper.

Finally, we show the effects of combining P6P and 6 T in an alternate layered morphology. Emission maps show the change in emitted color with temperature caused by the corresponding increase in exciton diffusion lengths reaching around 11 nm. At the same time, average exciton lifetimes become less sensitive to temperature effects staying around the 1 ns mark. Our findings provide a better physical insight into the factors that play a role in exciton diffusion in general and in the particular case of P6P and 6 T nanofibers. More importantly, they also point to the necessity of reevaluating experimental estimates of exciton diffusion length.

References

1. Brabec, C. J., Hauch, J. A., Schilinsky, P. & Waldauf, C. Production aspects of organic photovoltaics and their impact on the commercialization of devices. *MRS bulletin* **30**, 50–52 (2005).
2. Brédas, J.-L., Norton, J. E., Cornil, J. & Coropceanu, V. Molecular understanding of organic solar cells: the challenges. *Accounts chemical research* **42**, 1691–1699 (2009).
3. de Oliveira Neto, P. H., da Silva Filho, D. A., da Cunha, W. F., Acioli, P. H. & e Silva, G. M. Limit of exciton diffusion in highly ordered p-conjugated systems. *The J. Phys. Chem. C* **119**, 19654–19659 (2015).
4. Peumans, P., Yakimov, A. & Forrest, S. R. Small molecular weight organic thin-film photodetectors and solar cells. *J. Appl. Phys.* **93**, 3693–3723 (2003).
5. Vandewal, K., Tvingstedt, K. & Inganäs, O. 8 charge transfer states in organic donor—acceptor solar cells. *Semicond. Semimetals* **85**, 261 (2011).
6. Mikhnenko, O. V., Blom, P. W. & Nguyen, T.-Q. Exciton diffusion in organic semiconductors. *Energy & Environ. Sci.* **8**, 1867–1888 (2015).
7. Bjorgaard, J. A. & Köse, M. E. Simulations of singlet exciton diffusion in organic semiconductors: a review. *RSC Adv.* **5**, 8432–8445 (2015).
8. Kankate, L., Balzer, F., Niehus, H. & Rubahn, H.-G. Organic nanofibers from thiophene oligomers. *Thin Solid Films* **518**, 130–137 (2009).
9. Resel, R. *et al.* Origins for epitaxial order of sexiphenyl crystals on muscovite (001). *Surf. Interface Analysis: An Int. J. devoted to development application techniques for analysis surfaces, interfaces thin films* **41**, 764–770 (2009).
10. Simbrunner, C. *et al.* Color tuning of nanofibers by periodic organic–organic hetero-epitaxy. *ACS nano* **6**, 4629–4638 (2012).
11. Simbrunner, C. *et al.* Epitaxial growth of sexithiophene on mica surfaces. *Phys. Rev. B* **83**, 115443 (2011).
12. Balzer, F. & Rubahn, H.-G. Growth control and optics of organic nanoaggregates. *Adv. Funct. Mater.* **15**, 17–24 (2005).
13. Simbrunner, C. *et al.* Organic- organic heteroepitaxy of red-, green-, and blue-emitting nanofibers. *ACS nano* **4**, 6244–6250 (2010).

14. Förster, T. Zwischenmolekulare energiewanderung und fluoreszenz. *Annalen der physik* **437**, 55–75 (1948).
15. Förster, T. 10th spiers memorial lecture. transfer mechanisms of electronic excitation. *Discuss. Faraday Soc.* **27**, 7–17 (1959).
16. May, V. & Oliver, K. Charge and energy transfer dynamics in molecular systems (John Wiley & Sons, 2008).
17. Köhler, A. & Bässler, H. Electronic processes in organic semiconductors: An introduction (John Wiley & Sons, 2015).
18. Yost, S. R., Hontz, E., Yeganeh, S. & Van Voorhis, T. Triplet vs singlet energy transfer in organic semiconductors: the tortoise and the hare. *The J. Phys. Chem. C* **116**, 17369–17377 (2012).
19. Oosterhout, S. D. *et al*. The effect of three-dimensional morphology on the efficiency of hybrid polymer solar cells. *Nat. materials* **8**, 818 (2009).
20. Lunt, R. R., Benziger, J. B. & Forrest, S. R. Relationship between crystalline order and exciton diffusion length in molecular organic semiconductors. *Adv. Mater.* **22**, 1233–1236 (2010).
21. Feron, K., Belcher, W. J., Fell, C. J. & Dastoor, P. C. Organic solar cells: understanding the role of förster resonance energy transfer. *Int. journal molecular sciences* **13**, 17019–17047 (2012).
22. Mikhnenko, O. *et al*. Temperature dependence of exciton diffusion in conjugated polymers. *The J. Phys. Chem. B* **112**, 11601–11604 (2008).
23. Madigan, C. & Bulović, V. Modeling of exciton diffusion in amorphous organic thin films. *Phys. review letters* **96**, 046404 (2006).
24. Menke, S. M. & Holmes, R. J. Evaluating the role of energetic disorder and thermal activation in exciton transport. *J. Mater. Chem. C* **4**, 3437–3442 (2016).
25. Kawashima, E., Fujii, M. & Yamashita, K. Thermal effect on the morphology and performance of organic photovoltaics. *Phys. Chem. Chem. Phys.* **18**, 26456–26465 (2016).
26. Evaristo de Sousa, L., Ferreira da Cunha, W., Antônio da Silva Filho, D. & de Oliveira Neto, P. H. Biexciton cascade emission in multilayered organic nanofibers. *Appl. Phys. Lett.* **112**, 143301 (2018).
27. de Sousa, L. E., de Oliveira Neto, P. H., Kjelstrup-Hansen, J. & da Silva Filho, D. A. Modeling temperature dependent singlet exciton dynamics in multilayered organic nanofibers. *The J. Chem. Phys.* **148**, 204101 (2018).
28. Mani, A., Schoonman, J. & Goossens, A. Photoluminescence study of sexithiophene thin films. *The J. Phys. Chem. B* **109**, 4829–4836 (2005).
29. Tavares, L. *et al*. Efficient exciton diffusion and resonance-energy transfer in multilayered organic epitaxial nanofibers. *The J. Phys. Chem. C* **119**, 15689–15697 (2015).

Acknowledgements

Author Contributions

L.E.S. wrote the code, ran the simulations and wrote the manuscript. P.H.O.N. created the figures and supervised the work. D.A.S.F. and R.T.S. reviewed the manuscript. All authors discussed the results.

Additional Information

Supplementary information accompanies this paper at https://doi.org/10.1038/s41598-018-32232-5.

Competing Interests: The authors declare no competing interests.

Publisher's note: Springer Nature remains neutral with regard to jurisdictional claims in published maps and institutional affiliations.

Article 7

ARTICLE TYPE

Dynamical Exciton Decay in Organic Materials: The Role of Bimolecular Recombination

Leonardo Evaristo de Sousa[a], Fernando Teixeira Bueno[a], Demétrio Antônio da Silva Filho[a], Luiz Antônio Ribeiro Junior[*b,c], and Pedro Henrique de Oliveira Neto[a]

Excitons play a critical role in light emission when it comes to organic semiconductors. In high exciton concentration regimes, monomolecular and bimolecular routes for exciton recombination can yield different products affecting significantly the material's optical properties. Here, the dynamical decay of excitons is theoretically investigated using a kinetic Monte Carlo approach that addresses singlet exciton diffusion. Our numerical protocol includes two distinct exciton-exciton interaction channels: exciton annihilation and biexciton cascade emission. Our findings reveal that these channels produce different consequences concerning diffusion and spectroscopic properties, being able to explain diverging experimental observations. Importantly, we estimate critical exciton densities for which bimolecular recombination becomes dominant and investigate its effect on average exciton lifetimes and diffusion lengths.

1 Introduction

In organic electronics, exciton dynamics play a significant role in the working of devices [1,2]. For instance, in Organic Light-Emitting Diodes (OLEDs), photons are emitted as a result of the recombination of excitons generated from injected holes and electrons [3]. Furthermore, excitons generated in Organic Photovoltaic devices (OPVs) must diffuse through the material until reaching a donor-acceptor interface where they may dissociate into free charges [4]. In these applications, exciton dynamics is, therefore, a crucial issue that should be understood in detail to guide the improvement of device performance.

For singlet excitons, limited diffusion lengths have required special care in the designing of devices, leading to the development of bulk heterojunctions [5–7]. Even though morphology has been found to be an essential factor in the efficiency of exciton diffusion [8] the primary limiting factor for singlet excitons diffusion lengths is their radiative lifetimes [9,10], which is the typical time it takes for excitons to recombine spontaneously. This phenomenon is a monomolecular process whose occurrence is proportional to exciton density in the material.

Experimentally, exciton dynamics are studied by different techniques such as time-resolved photoluminescence (TDPL) spectroscopy [11–14], in which a laser is used to excite a material and exciton depopulation is registered by the amount of light emitted as a function time. Depending on the pump fluences employed, exciton concentrations may reach large enough values to reveal the role of exciton-exciton interactions to be relevant. These interactions may affect exciton lifetimes significantly, as well as diffusion lengths.

Bimolecular phenomena, i.e., the interaction mechanism between quasiparticles lying in different moieties and its yielded products, may take place, for instance, in the form of exciton-exciton annihilation [15] or in the form of biexciton cascade emissions [16]. In the case of exciton-exciton annihilation, two singlet excitons that find each other result in the non-radiative recombination of one of them [17] ($S_1 + S_1 \rightarrow S_1 + S_0$). On the other hand, in the process known as biexciton cascade emission, two excitons that occupy the same space combine into a biexciton. Biexcitons have lifetimes much shorter than those of singlet excitons, thus recombining faster. The biexciton recombination produces a photon with an energy given by $2E_X - BE_{XX}$, where E_X is the exciton's energy and BE_{XX} the biexciton's binding energy. The emission of this first photon then stimulates the emission of the second one with energy E_X.

These two bimolecular phenomena are particularly important when exciton concentration is high, but are fundamentally different. Experimental observations of both effects in organic materials have been made [18–20]. In the particular case of para-hexaphenyl (P6P), experiments performed on films report exciton annihilation [21], stimulated emission [22,23] and even lasing [24]

[a] Institute of Physics, University of Brasília, Brasília, 70910-900, Brasília, Brazil
[b] Department of Physics, Chemistry and Biology (IFM), Linköping University, SE-581 83 Linköping, Sweden. E-mail: luiju@ifm.liu.se
[c] International Center for Condensed Matter Physics, University of Brasília, P.O. Box 04513, 70910-900, Brasília, Brazil

at high pump fluences.

Superlinear increases in light emission have been ascribed to biexciton generation [25] in organics, as is the case in other materials [26], and also to amplified spontaneous emission [27]. In addition, theoretical works predict the existence of biexcitons in π-conjugated systems [28–30]. This state of affairs makes for interesting grounds for studies on the possible experimental consequences of bimolecular models.

Herein, we implement two exciton-exciton interaction models and investigate their role in spectroscopic and exciton diffusion properties. The first model considers only singlet exciton annihilation and the second one includes the possibility of biexciton cascade emission. Taking advantage of previous studies on exciton diffusion in P6P [28,31,32], we use a Kinetic Monte Carlo (KMC) [33,34] program to simulate singlet exciton diffusion and interaction for various exciton concentrations. The KMC program allows for the simulation of TDPL and emission spectra which are compared to experimental results. We show that when only exciton-exciton annihilation is present monomolecular contributions to photoluminescence (PL) decay are dominant for most of the concentration range. However, when biexciton cascade emissions are taken into account, bimolecular contributions may drastically increase becoming the dominant effect. Critical exciton densities for both processes are estimated. Furthermore, concentration effects on exciton lifetime and diffusion length are discussed.

2 Methods

KMC simulations were run in a 100 x 100 square grid to simulate exciton diffusion between P6P nanofibers. In agreement with a previous study [31], the spacing between adjacent sites in the grid was set to 1 nm. Excitons are randomly distributed in the grid according to the desired concentration. Hops to any of the exciton's eight nearest neighbors are allowed (Figure 1-a). To decide to which neighbor an exciton hops, the Förster rates of all the possible transitions are calculated as [35–37]

$$k_F = \frac{1}{\tau} \left(\frac{R_F}{r} \right)^6 \tag{1}$$

in which τ is the exciton lifetime, R_F the Förster radius and r the distance between sites. The probability of a given site being chosen is calculated as $k_i / \sum_j k_j$ and a random number is generated to make the selection. Once the hopping site is chosen, a new random number is drawn to decide whether the exciton hops or recombines. The probability of the Förster transfer taking place is obtained by:

$$P = \frac{1}{1 + \left(\frac{r}{R_F} \right)^6}. \tag{2}$$

All simulations were performed at 300 K. At this temperature, the P6P Förster radius and exciton lifetime have been estimated to be 2.3 nm and 440 ps, respectively [28,31]. Exciton concentrations ranging from 0.01% to 4.9% (meaning excitons per site) were analyzed. Each simulation was repeated 1000 times and results were averaged over.

Two models for exciton-exciton interactions were studied.

These models attempt to explain two markedly different experimental results [22]. In this study, TDPL and emission spectra of P6P films show remarkably different properties depending on the orientation of growth of the P6P nanofibers, parallel or perpendicular to the substrate. Samples produced under these two conditions presented ordered domains of very different sizes, indicating that morphological aspects may be key to the prevalence of different bimolecular phenomena.

When molecules lay parallel to the substrate, short and long PL decay components are observed, with the emission spectra showing a large peak at 2.92 eV and a less intense peak at 2.77 eV. In light of these results, our first model took into account exciton-exciton annihilation. In this model (Figure 1-b), when two excitons hop to the same location, one of them is removed from the simulation whereas the other remains. The annihilated exciton does not contribute to the spectra since its recombination is non-radiative.

Now, when molecules stand perpendicular to the substrate, radiative lifetimes become much shorter and the emission spectra presents a new peak at 2.88 eV, whereas the 2.77 eV peak has its intensity greatly reduced. We attribute the appearance of this new peak in the P6P emission spectrum to a biexciton cascade emission. In this case, the redshift of the 2.88 eV nm peak with respect to the 2.92 eV one provides an estimate of the biexciton binding energy of 0.04 eV. Thus, in our second model (Figure 1-c), excitons that hop to the same site may either annihilate each other non-radiatively or generate a biexciton. The biexciton recombines promptly emitting two photons in a cascade effect. The energy of one of the photons corresponds to the site energy whereas for the second it is the site energy minus the biexciton binding energy, which was set to 0.04 eV in accordance with the discussion above. Whether the excitons annihilate each other or undergo a biexciton cascade emission depends on the energy of the site where they meet. We consider here that biexcitons are generated only if the site energy is under 2.85 eV. This amounts to allowing biexciton generation only when the $S1$ state corresponds to the $0 - 1$ vibronic band of P6P. This is justifiable as a new peak red shifted with respect to the 0-2 transition is not observed experimentally. In addition, the 0-0 transition is found to be much less intense [27], meaning that the 0-1 and 0-2 vibronic bands are the ones that contribute more significantly to the fluorescence spectrum.

To determine whether a site had an energy corresponding to the 0-1 or 0-2 vibronic band, each site was randomly assigned a number referring to the energy of emitted photons resulting from exciton recombination at that site. To reproduce the emission spectrum of P6P, these site energy values were sampled from two Gaussian distributions with means of 2.92 eV and 2.77 eV, corresponding to the $0 - 1$ and $0 - 2$ transitions, respectively (Figure 1-d). The standard deviation of the Gaussian distributions was set at $1.5kT$, which amounts to 0.0375 eV at 300 K. To account for the difference in intensities between the two peaks, 55% of the sites had energy values taken from the $0 - 1$ transition and the rest from the $0 - 2$.

When an exciton undergoes recombination, whether by spontaneous or stimulated emission, the time, position and energy value
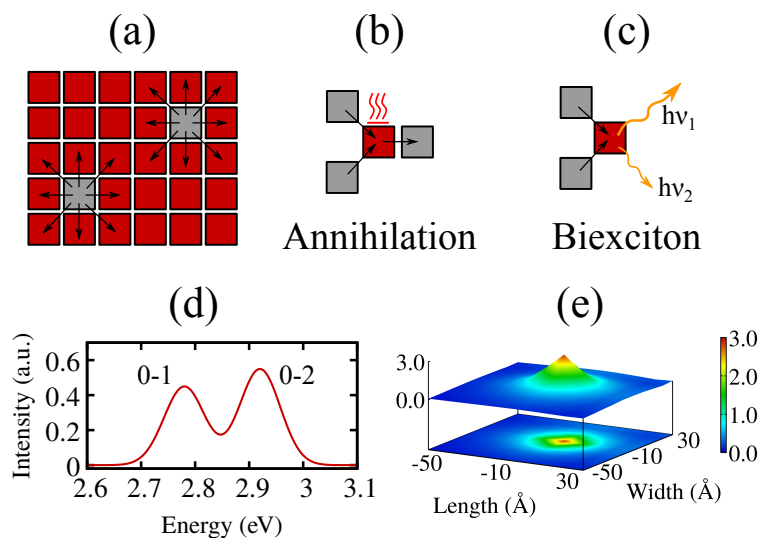
Fig. 1 a) Schematics of the KMC model. Excitons are generated randomly in a grid and may hop to their nearest neighbors. b) Annihilation model: when two excitons hop to the same site, one of them recombines non-radiatively. c) Biexciton model: when two excitons hop to the same site, both recombine radiatively with different energies. d) Site energy distribution simulating the 0-1 and 0-2 transitions that compose the emission spectra of P6P. e) Emission map showing the spatial distribution of emitted photons in the simulation.

of emitted photon are registered. This allows for the simulation of emission and TDPL spectra as well as for producing emission maps (Figure 1-e) and estimating exciton diffusion length and average lifetime.

3 Results and Discussion

To analyze the differences between the spectroscopic results of both models, we look into the simulated TDPL and emission spectra produced for several exciton concentrations. In the case of annihilation, TDPL spectra (Figure 2-a) show an increase in emitted intensity and a faster decay for initial times that become more evident as concentrations increase, indicating, as expected, the presence of two PL decay components. It is worth mention that the intensities shown in the simulated TDPL spectra are proportional to the number of excitons that have recombined radiatively at each moment in time. As to the emission spectra obtained from the annihilation model (Figure 2-b), the major effect of increasing concentration is a corresponding increase in emitted intensity, with the relative intensities between peaks remaining constant. It can also be seen that the relative increase in intensity from one concentration to the next reduces progressively. This means that the simulations are nearing the critical exciton concentration in which the non-radiative annihilation events become dominant. From this point on, emission intensities are bound to decrease with concentration.

For the biexciton model, TDPL spectra (Figure 2-c) also show a two-component decay PL with higher intensities when compared to the annihilation model results. This is explained by the fact that the non-radiative recombinations are restricted to sites with energies corresponding to the 0-2 transition. In addition, the emission spectra (Figure 2-d) present an increase in emitted intensity but also present a change in the relative intensities between peaks, as well as the appearance of a shoulder near the 0-1 transition

that becomes more pronounced as concentrations become larger. The relative intensity of the peaks changes with concentration because of the larger number of exciton annihilation events that happen for excitons with energies associated with the $0-2$ transition. Since these are non-radiative recombination events, the corresponding peak does not increase with concentration as significantly as the 0-1 transition peak, which undergoes biexciton cascade emissions. This is also responsible for the larger relative increase in intensity of the 0-1 peak from one concentration value to the next. As to the appearance of a shoulder, it is caused by the fact that the first photon emitted in the biexciton cascade process is slightly red shifted with respect to the second photon whose emission it stimulates. The amount of red shift is given by the biexciton's binding energy of 0.04 eV.
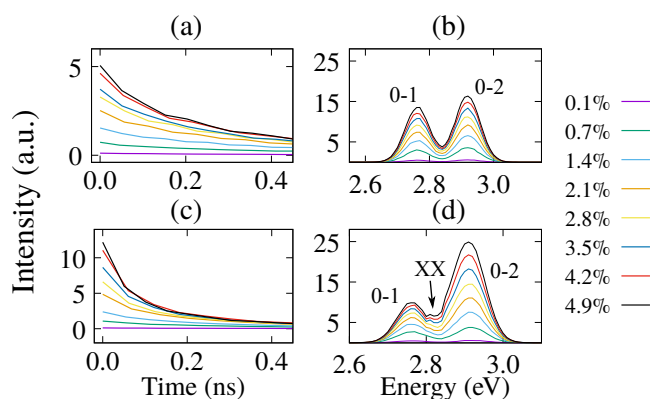
Fig. 2 Simulated TDPL and emission spectra for the annihilation model (a and b) and for the biexciton model (c and d). The 0–1 and 0–2 vibronic bands are shown, as well as the contribution from red shifted photons emitted in the biexciton cascade process (XX)

Concentration effects produced by both interaction models on
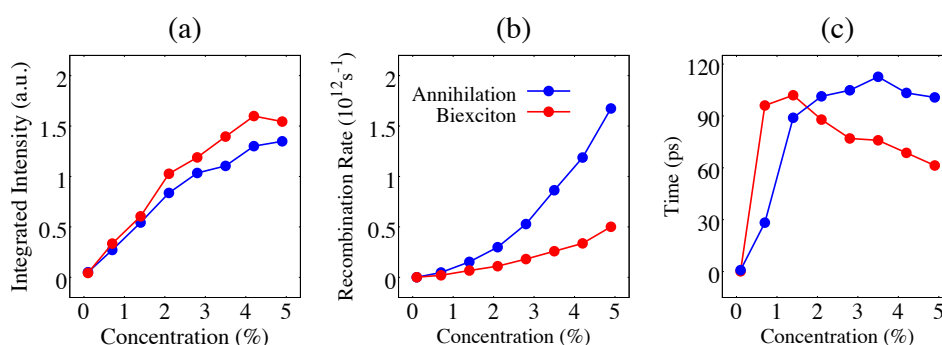
Fig. 3 a) Time integrated emission intensity as a function of exciton concentration. b) Annihilation rate at maximum density. c) Decay time t_b of the bimolecular PL component for both interaction models.

the TDPL spectra are not easily distinguishable, thus requiring a more detailed analysis. In Figure 3-a, the time integrated intensity is presented for both models as a function of exciton concentration. For low concentration values, both models show a similar linear behavior. This changes as the concentration moves from 1.4% to 2.1%. The biexciton model shows a superlinear transition, as opposed to the persistence of the linear behavior in the annihilation model. This superlinear transition quickly reverses to linear behavior again until a saturation point is reached near 4.2%. Similarly, the annihilation model also shows saturation signs as the response drops below linearity around 3.5% concentration.

The reason for saturation being achieved earlier in the annihilation model is its non-radiative nature. Even though the biexciton model also includes non-radiative annihilation effects, these are restricted to the 0-2 transition. This results in a lower annihilation coefficient (γ) in the biexciton model when compared to the annihilation one. We may compare the initial values for the annihilation rates in both models (γn_0, with n_0 being the initial exciton concentration). Figure 3-b shows these values for both models. These initial annihilation rates range from $7.3 \times 10^8\ s^{-1}$ to $1.7 \times 10^{12}\ s^{-1}$ in the annihilation only model and from $6.5 \times 10^8\ s^{-1}$ to $0.5 \times 10^{12}\ s^{-1}$ in the biexciton model.

The TDPL curves diverge further from monoexponential decay behavior as exciton density increases, becoming well fitted by bi-exponential functions. It is worth notice that in both models the number of emitted photons at each instant is due either partly (biexciton model) or totally (annihilation model) to spontaneous recombination of excitons. This process has a characteristic time given by the exciton radiative lifetime which is set to 440 ps for simulations at 300 K. Thus, we fit the TDPL curves with the function

$$I(t) = A_m \exp(-t/440) + A_b \exp(-t/t_b) \qquad (3)$$

where A_m and A_b correspond to the monomolecular and bimolecular amplitudes, respectively. The decay time of the monomolecular contribution is fixed at 440 ps and t_b is the characteristic decay time of the bimolecular contribution.

The bimolecular decay times are shown in Figure 3-c. For 0.1% concentration, the decay time is close to zero for both models,

as the bimolecular contribution is very small, making the TDPL spectrum of virtually monoexponential behavior. However, this characteristic time rises sharply in the biexciton model to around 100 ps only to drop continuously for concentrations larger than 1.4%, reaching 60 ps at 4.9%. This may be interpreted as a reduction in the typical time it takes for excitons to find each other and interact. Similar results should be expected for the annihilation model, but in the considered concentration range, its decay times remain near 100 ps.

The reason for this difference may be better understood by looking at the monomolecular and bimolecular amplitudes A_m and A_b. These are shown in Figure 4-a for the biexciton model and in Figure 4-b for the annihilation model. In the first case, the amplitudes begin to diverge around the 1.4% concentration mark. After that, the bimolecular contribution becomes clearly dominant, detaching completely from the monomolecular amplitude. The same cannot be said for the annihilation model. Both contributions show comparable values. The bimolecular amplitude matches the monomolecular one only at 5% concentration. Thus we may conclude that the critical concentrations from which bimolecular processes become dominant are estimated in 1.5% and 5% for the biexciton and annihilation models, respectively. This more than triple critical concentration required for bimolecular dominance in the annihilation model is responsible for the difference in behavior of the decay time in comparison to the one from the biexciton model.

It is important to put the current results in the context of experimental conditions. A conservative estimate of the pump fluences required to produce the exciton concentrations considered here can be made. Assuming a 3.26 eV laser pulse in our 10^6 Å^2 grid would make for pump fluences ranging from 0.05 $\mu J/cm^2$ to 2.6 $\mu J/cm^2$. Since perfect absorption is assumed, these are lower bound estimates that would put the pump fluences necessary to achieve critical exciton density at 0.84 $\mu J/cm^2$ and 2.8 $\mu J/cm^2$ for the biexciton and annihilation models, respectively. It is reported[27] that, at room temperature, a linear recombination regime is expected only for pump fluences up to 0.1 $\mu J/cm^2$. This is in line with our simulation results. Lower temperatures are also bound to push the onset of bimolecular behavior into higher concentrations as exciton diffusion is a temperature activated process
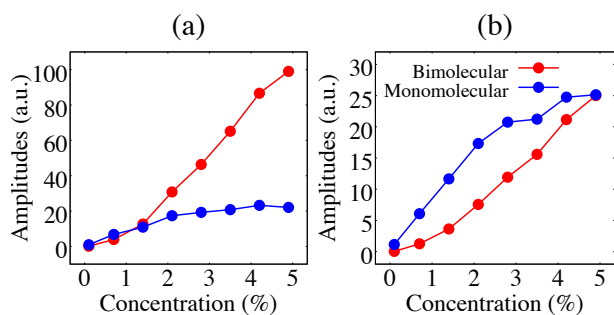
Fig. 4 Monomolecular and bimolecular amplitudes calculated from fitting simulated TDPL spectra produced with the biexciton (a) and annihilation (b) models.
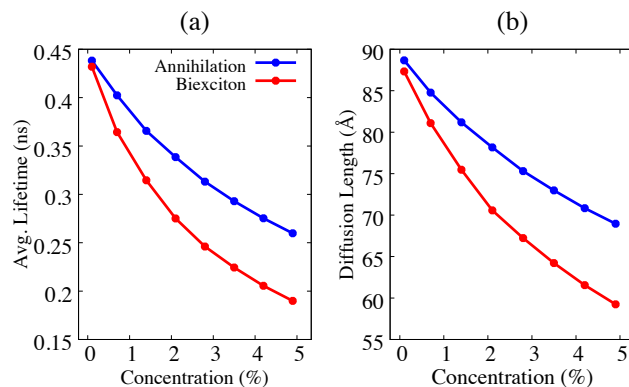

Fig. 5 Average exciton lifetime (a) and diffusion length (b) as a function of concentration for the two interaction models.

in P6P [11,31].

Furthermore, it is conceivable that, if the stimulated emission produced by the biexciton decay is not completely efficient, then critical exciton densities should also be higher. This may also make the observed biexciton shoulder (Figure 2-d) develop into a full peak [22], since for every photon emitted from biexciton recombination there would not necessarily be a photon with energy corresponding to the 0-1 transition. Also, at very high concentrations, it is then expected for the TDPL spectra to resume mono-exponential behavior with very fast decay times. This is precisely what has been experimentally observed [19,22].

The critical concentration is also a function of exciton diffusion length in the material. Materials with lower exciton diffusion length require higher pump fluences to achieve the same level of bimolecular recombination. In poly(para-phenylene)-type polymers, this critical concentration has been reported to be achieved at 3.1 $\mu J/cm^2$ [19], whereas exciton diffusion length in such materials are measured to be around only 5 nm [17].

Conversely, measurements of exciton diffusion length may also be affected by bimolecular processes. Thus, to conclude, we investigate the effects on exciton lifetime and diffusion length of both interaction models considered here. Figure 5 show how these two features change with increasing exciton concentration. It can be seen that the biexciton model decreases lifetimes and diffusion lengths more sharply than the annihilation model. This may be explained by the fact that in the biexciton model, both excitons that generate the biexciton recombine at once. In the case of annihilation, only one of the excitons recombines non-radiatively whereas the other remains active.

In both models, lifetime and diffusion length reduction become less steep as concentration becomes higher. In the 0.01% to 5% concentration range, average exciton lifetime drops from 440 ps, which is the assumed radiative lifetime, to 260 ps and 190 ps for the annihilation and biexciton models, respectively. In the same concentration range, exciton diffusion length reduces from around 9 nm to 6.8 nm and 5.9 nm. These values correspond to a 25% and a 34% decrease in diffusion length, respectively. These results show that exciton-exciton interactions are an important factor to be considered in applications that rely on exciton diffusion regardless of the particular type of interaction present.

4 Conclusion

In summary, we analyzed two models for exciton-exciton interactions that are able to explain different experimental results. In the exciton annihilation model - in which when two excitons find each other one of them recombines non-radiatively while the other remains active -, concentration effects are observed in the emission spectra, where an increase in concentration is associated to an increase in emitted intensity with no change in relative intensity between peaks.

In the biexciton model, excitons may form a biexciton if their energy correspond to the 0-1 transition energy. Otherwise, they may recombine non-radiatively. This model predicts changes in the relative intensity between peaks as concentration becomes larger. It also produces a new peak, slightly red shifted with respect to the 0-1 transition, corresponding to the biexciton recombination.

The two interaction models produce changes in the TDPL spectra, with the appearance of a two-component PL decay which is well fitted by biexponential functions. They differ, however, on the evolution of the amplitudes with concentration. Critical exciton concentrations are estimated for both processes and are found to be within reasonable values when compared to experimental results.

Finally, it is shown how both models affect average exciton lifetime and diffusion length. Exciton concentrations of around 5% are enough to practically half both features under the simulated conditions. For materials with higher Förster radii, this may happen for even lower concentrations. These results stress the importance of taking exciton-exciton interactions into account in the design of devices that rely on exciton diffusion for optimal performance, such as organic photovoltaic devices and also in the performance of exciton diffusion length measurements.

Acknowledgements

References

1 C. J. Brabec, J. A. Hauch, P. Schilinsky and C. Waldauf, *MRS bulletin*, 2005, **30**, 50–52.

2 J.-L. Brédas, J. E. Norton, J. Cornil and V. Coropceanu, *Accounts of chemical research*, 2009, **42**, 1691–1699.

3 K. Saxena, V. Jain and D. S. Mehta, *Optical Materials*, 2009, **32**, 221–233.

4 B. Kippelen and J.-L. Brédas, *Energy & Environmental Science*, 2009, **2**, 251–261.

5 M. C. Scharber and N. S. Sariciftci, *Progress in polymer science*, 2013, **38**, 1929–1940.

6 M. C. Scharber, D. Mühlbacher, M. Koppe, P. Denk, C. Waldauf, A. J. Heeger and C. J. Brabec, *Advanced materials*, 2006, **18**, 789–794.

7 Y. Liang, Z. Xu, J. Xia, S.-T. Tsai, Y. Wu, G. Li, C. Ray and L. Yu, *Advanced materials*, 2010, **22**, E135–E138.

8 R. R. Lunt, J. B. Benziger and S. R. Forrest, *Advanced Materials*, 2010, **22**, 1233–1236.

9 S. R. Yost, E. Hontz, S. Yeganeh and T. Van Voorhis, *The Journal of Physical Chemistry C*, 2012, **116**, 17369–17377.

10 H. Gommans, S. Schols, A. Kadashchuk, P. Heremans and S. Meskers, *The Journal of Physical Chemistry C*, 2009, **113**, 2974–2979.

11 L. Tavares, M. Cadelano, F. Quochi, C. Simbrunner, G. Schwabegger, M. Saba, A. Mura, G. Bongiovanni, D. A. d. S. Filho and W. F. da Cunha, *The Journal of Physical Chemistry C*, 2015, **119**, 15689–15697.

12 J. C. de Mello, H. F. Wittmann and R. H. Friend, *Advanced materials*, 1997, **9**, 230–232.

13 S. Heun, R. Mahrt, A. Greiner, U. Lemmer, H. Bassler, D. Halliday, D. Bradley, P. Burn and A. Holmes, *Journal of Physics: Condensed Matter*, 1993, **5**, 247.

14 H. Najafov, B. Lee, Q. Zhou, L. Feldman, Podzorov and V, *Nature materials*, 2010, **9**, 938.

15 A. Köhler and H. Bässler, *Electronic processes in organic semiconductors: An introduction*, John Wiley & Sons, 2015.

16 T. Ihara, *Physical Review B*, 2016, **93**, 235442.

17 O. V. Mikhnenko, P. W. Blom and T.-Q. Nguyen, *Energy & Environmental Science*, 2015, **8**, 1867–1888.

18 V. Klimov, D. McBranch, N. Barashkov and J. Ferraris, *Physical Review B*, 1998, **58**, 7654.

19 G. Kranzelbinder, M. Nisoli, S. Stagira, S. De Silvestri, G. Lanzani, K. Müllen, U. Scherf, W. Graupner and G. Leising, *Applied physics letters*, 1997, **71**, 2725–2727.

20 A. Dogariu, D. Vacar and A. J. Heeger, *Physical Review B*, 1998, **58**, 10218.

21 A. Piaggi, G. Lanzani, G. Bongiovanni, A. Mura, W. Graupner, F. Meghdadi, G. Leising and M. Nisoli, *Physical Review B*, 1997, **56**, 10133.

22 E. Faulques, J. Wéry, S. Lefrant, V. Ivanov and G. Jonusauskas, *Physical Review B*, 2002, **65**, 212202.

23 G. Leising, S. Tasch, C. Brandstätter, W. Graupner, S. Hampel, E. List, F. Meghdadi, C. Zenz, P. Schlichting, U. Rohr *et al.*, *Synthetic metals*, 1997, **91**, 41–47.

24 F. Quochi, F. Cordella, A. Mura, G. Bongiovanni, F. Balzer and H.-G. Rubahn, *Applied Physics Letters*, 2006, **88**, 041106.

25 S. Frolov, W. Gellermann, M. Ozaki, K. Yoshino and Z. Vardeny, *Physical review letters*, 1997, **78**, 729.

26 J. Q. Grim, S. Christodoulou, F. Di Stasio, R. Krahne, R. Cingolani, L. Manna and I. Moreels, *Nature nanotechnology*, 2014, **9**, 891.

27 F. Quochi, *Journal of Optics*, 2010, **12**, 024003.

28 L. Evaristo de Sousa, W. Ferreira da Cunha, D. Antônio da Silva Filho and P. H. de Oliveira Neto, *Applied Physics Letters*, 2018, **112**, 143301.

29 M. A. Pasquinelli and D. Yaron, *The Journal of chemical physics*, 2003, **118**, 8082–8092.

30 M. Chandross, Y. Shimoi and S. Mazumdar, *Chemical physics letters*, 1997, **280**, 85–90.

31 L. E. de Sousa, P. H. de Oliveira Neto, J. Kjelstrup-Hansen and D. A. da Silva Filho, *The Journal of Chemical Physics*, 2018, **148**, 204101.

32 L. E. de Sousa, D. A. da Silva Filho, R. T. de Sousa Jr. and de Oliveira Neto, *Scientific reports*, 2018, accepted.

33 J. A. Bjorgaard and M. E. Köse, *RSC Advances*, 2015, **5**, 8432–8445.

34 P. K. Watkins, A. B. Walker and G. L. Verschoor, *Nano letters*, 2005, **5**, 1814–1818.

35 V. May and K. Oliver, *Charge and energy transfer dynamics in molecular systems*, John Wiley & Sons, 2008.

36 T. Förster, *Annalen der physik*, 1948, **437**, 55–75.

37 T. Förster, *Discussions of the Faraday Society*, 1959, **27**, 7–17.

Bibliography

[1] Leonardo Evaristo de Sousa, Luiz Antonio Ribeiro, Antonio Luciano de Almeida Fonseca, and Demétrio Antonio da Silva Filho. Modeling the emission spectra of organic molecules: A competition between franck–condon and nuclear ensemble methods. *The Journal of Physical Chemistry A*, 120(27):5380–5388, 2016.

[2] Luciana Tavares, Michele Cadelano, Francesco Quochi, Clemens Simbrunner, Gunther Schwabegger, Michele Saba, Andrea Mura, Giovanni Bongiovanni, Demetrio Antonio da Silva Filho, Wiliam Ferreira da Cunha, et al. Efficient exciton diffusion and resonance-energy transfer in multilayered organic epitaxial nanofibers. *The Journal of Physical Chemistry C*, 119(27):15689–15697, 2015.

[3] Leonardo Evaristo de Sousa, Pedro Henrique de Oliveira Neto, Jakob Kjelstrup-Hansen, and Demétrio Antônio da Silva Filho. Modeling temperature dependent singlet exciton dynamics in multilayered organic nanofibers. *The Journal of Chemical Physics*, 148(20):204101, 2018.

[4] Leonardo Evaristo de Sousa, Wiliam Ferreira da Cunha, Demétrio Antônio da Silva Filho, and Pedro Henrique de Oliveira Neto. Biexciton cascade emission in multilayered organic nanofibers. *Applied Physics Letters*, 112(14):143301, 2018.

[5] Leonardo Evaristo de Sousa, Demétrio Antônio da Silva Filho, Rafael Timóteo de Sousa, and Pedro Henrique de Oliveira Neto. Exciton diffusion in organic nanofibers: A monte carlo study on the effects of temperature and dimensionality. *Scientific reports*, 8(1):14066, 2018.

[6] Volkhard May and K Oliver. *Charge and energy transfer dynamics in molecular systems*. John Wiley & Sons, 2008.

[7] Lukas Schmidt-Mende and Jonas Weickert. *Organic and hybrid solar cells: an introduction*. Walter de Gruyter GmbH & Co KG, 2016.

[8] David L Dexter. A theory of sensitized luminescence in solids. *The Journal of Chemical Physics*, 21(5):836–850, 1953.

[9] Th Förster. Zwischenmolekulare energiewanderung und fluoreszenz. *Annalen der physik*, 437(1-2):55–75, 1948.

[10] Yingli Niu, Qian Peng, Chunmei Deng, Xing Gao, and Zhigang Shuai. Theory of excited state decays and optical spectra: Application to polyatomic molecules. *The Journal of Physical Chemistry A*, 114(30):7817–7831, 2010.

[11] Vincenzo Barone, Julien Bloino, Malgorzata Biczysko, and Fabrizio Santoro. Fully integrated approach to compute vibrationally resolved optical spectra: from small molecules to macrosystems. *Journal of chemical theory and computation*, 5(3):540–554, 2009.

[12] Mario Barbatti, Matthias Ruckenbauer, Felix Plasser, Jiri Pittner, Giovanni Granucci, Maurizio Persico, and Hans Lischka. Newton-x: a surface-hopping program for nonadiabatic molecular dynamics. *Wiley Interdisciplinary Reviews: Computational Molecular Science*, 4(1):26–33, 2014.

[13] Rachel Crespo-Otero and Mario Barbatti. Spectrum simulation and decomposition with nuclear ensemble: formal derivation and application to benzene, furan and 2-phenylfuran. *Theoretical Chemistry Accounts*, 131(6):1237, 2012.

[14] M. J. Frisch, G. W. Trucks, H. B. Schlegel, G. E. Scuseria, M. A. Robb, J. R. Cheeseman, G. Scalmani, V. Barone, B. Mennucci, G. A. Petersson, H. Nakatsuji, M. Caricato, X. Li, H. P. Hratchian, A. F. Izmaylov, J. Bloino, G. Zheng, J. L. Sonnenberg, M. Hada, M. Ehara, K. Toyota, R. Fukuda, J. Hasegawa, M. Ishida, T. Nakajima, Y. Honda, O. Kitao, H. Nakai, T. Vreven, J. A. Montgomery, Jr., J. E. Peralta, F. Ogliaro, M. Bearpark, J. J. Heyd, E. Brothers, K. N. Kudin, V. N. Staroverov, R. Kobayashi, J. Normand, K. Raghavachari, A. Rendell, J. C. Burant, S. S. Iyengar, J. Tomasi, M. Cossi, N. Rega, J. M. Millam, M. Klene, J. E. Knox, J. B. Cross, V. Bakken, C. Adamo, J. Jaramillo, R. Gomperts, R. E. Stratmann, O. Yazyev, A. J. Austin, R. Cammi, C. Pomelli, J. W. Ochterski, R. L. Martin, K. Morokuma, V. G. Zakrzewski, G. A. Voth, P. Salvador, J. J. Dannenberg, S. Dapprich, A. D. Daniels, . Farkas, J. B. Foresman, J. V. Ortiz, J. Cioslowski, and D. J. Fox. Gaussian 09 revision c.01. Gaussian Inc. Wallingford CT 2009.

[15] Leonardo Evaristo de Sousa, Arthur Akira Mamiya, Jakob Kjelstrup-Hansen, and Demétrio Antônio da Silva Filho. A joint theoretical and experimental characterization of two acene-thiophene derivatives. *Journal of molecular modeling*, 23(2):52, 2017.

[16] Igo T Lima, Leonardo Sousa, Renato da S Freitas, Luiz Antonio Ribeiro Junior, Rafael Timóteo de Sousa Júnior, and Demétrio A da Silva Filho. A dft study of a set of natural dyes for organic electronics. *Journal of molecular modeling*, 23(12):343, 2017.

[17] Eric J Heller. Quantum corrections to classical photodissociation models. *The Journal of Chemical Physics*, 68(5):2066–2075, 1978.

[18] John P Bergsma, Peter H Berens, Kent R Wilson, Donald R Fredkin, and Eric J Heller. Electronic spectra from molecular dynamics: a simple approach. *The Journal of Physical Chemistry*, 88(3):612–619, 1984.

[19] Mario Barbatti, Adelia JA Aquino, and Hans Lischka. The uv absorption of nucleobases: semi-classical ab initio spectra simulations. *Physical Chemistry Chemical Physics*, 12(19):4959–4967, 2010.

[20] Richard P Feynman. *Statistical Mechanics: A Set of Lectures (Advanced Book Classics)*. Westview Press Incorporated, 1998.

[21] Donald Allan McQuarrie. Statistical mechanics. 1976.

[22] Kanchan Saxena, VK Jain, and Dalip Singh Mehta. A review on the light extraction techniques in organic electroluminescent devices. *Optical Materials*, 32(1):221–233, 2009.

[23] Jean-Luc Brédas, Joseph E Norton, Jérôme Cornil, and Veaceslav Coropceanu. Molecular understanding of organic solar cells: the challenges. *Accounts of chemical research*, 42(11):1691–1699, 2009.

[24] Shane R Yost, Eric Hontz, Sina Yeganeh, and Troy Van Voorhis. Triplet vs singlet energy transfer in organic semiconductors: the tortoise and the hare. *The Journal of Physical Chemistry C*, 116(33):17369–17377, 2012.

[25] Markus C Scharber, David Mühlbacher, Markus Koppe, Patrick Denk, Christoph Waldauf, Alan J Heeger, and Christoph J Brabec. Design rules for donors in bulk-heterojunction solar cellstowards 10% energy-conversion efficiency. *Advanced materials*, 18(6):789–794, 2006.

[26] Yongye Liang, Zheng Xu, Jiangbin Xia, Szu-Ting Tsai, Yue Wu, Gang Li, Claire Ray, and Luping Yu. For the bright futurebulk heterojunction polymer solar cells with power conversion efficiency of 7.4%. *Advanced materials*, 22(20):E135–E138, 2010.

[27] Th Förster. 10th spiers memorial lecture. transfer mechanisms of electronic excitation. *Discussions of the Faraday Society*, 27:7–17, 1959.

[28] Anna Köhler and Heinz Bässler. *Electronic processes in organic semiconductors: An introduction*. John Wiley & Sons, 2015.

[29] GLJA Rikken. Enhancement and inhibition of spontaneous emission. *Physica B: Condensed Matter*, 204(1-4):353–358, 1995.

[30] Tai-ichi Shibuya. The refractive-index correction to the radiative rate constant. *Chemical physics letters*, 103(1):46–48, 1983.

[31] David Phillips. A lifetime in photochemistry; some ultrafast measurements on singlet states. *Proc. R. Soc. A*, 472(2190):20160102, 2016.

[32] Riccardo Volpi, Sathish Kottravel, Morten Steen Nørby, Sven Stafstrom, and Mathieu Linares. Effect of polarization on the mobility of c60: A kinetic monte carlo study. *Journal of chemical theory and computation*, 12(2):812–824, 2016.

[33] Leonardo Sousa, Riccardo Volpi, Demétrio Antônio da Silva Filho, and Mathieu Linares. Mobility field and mobility temperature dependence in pc61bm: A kinetic monte-carlo study. *Chemical Physics Letters*, 689:74–81, 2017.

[34] Luiz Antonio Ribeiro, Pedro Henrique de Oliveira Neto, Wiliam Ferreira da Cunha, Ricardo Gargano, and Geraldo Magela e Silva. Predicting the equilibrium structure of organic semiconductors with genetic algorithms. *Chemical Physics Letters*, 555:168–172, 2013.

[35] Subhajit Nandy, Pinaki Chaudhury, and SP Bhattacharyya. Coulomb explosion in dicationic noble gas clusters: A genetic algorithm-based approach to critical size estimation for the suppression of coulomb explosion and prediction of dissociation channels. *The Journal of chemical physics*, 132(23):234104, 2010.

[36] Junliang Xu, Hsiao-Ling Zhou, Zhangjin Chen, and Chii-Dong Lin. Genetic-algorithm implementation of atomic potential reconstruction from differential electron scattering cross sections. *Physical Review A*, 79(5):052508, 2009.

[37] Luiz Fernando Roncaratti, Ricardo Gargano, and Geraldo Magela e Silva. A genetic algorithm to build diatomic potentials. *Journal of Molecular Structure: THEOCHEM*, 769(1):47–51, 2006.

[38] Wiliam Ferreira Da Cunha, Luiz Fernando Roncaratti, Ricardo Gargano, E Silva, and Geraldo Magela. Fitting potential energy surface of reactive systems via genetic algorithm. *International journal of quantum chemistry*, 106(13):2650–2657, 2006.

[39] Abraham. Savitzky and M. J. E. Golay. Smoothing and differentiation of data by simplified least squares procedures. *Analytical Chemistry*, 36(8):1627–1639, 1964.

[40] Oleksandr V Mikhnenko, Paul WM Blom, and Thuc-Quyen Nguyen. Exciton diffusion in organic semiconductors. *Energy & Environmental Science*, 8(7):1867–1888, 2015.

[41] VI Klimov, DW McBranch, N Barashkov, and J Ferraris. Biexcitons in π-conjugated oligomers: Intensity-dependent femtosecond transient-absorption study. *Physical Review B*, 58(12):7654, 1998.

[42] Toshiyuki Ihara. Biexciton cascade emission reveals absolute absorption cross section of single semiconductor nanocrystals. *Physical Review B*, 93(23):235442, 2016.

[43] Xiangnan Huang, Qinfeng Xu, Chunfeng Zhang, Xiaoyong Wang, and Min Xiao. Energy transfer of biexcitons in a single semiconductor nanocrystal. *Nano letters*, 16(4):2492–2496, 2016.

[44] Federico Pevere, Ilya Sychugov, Fatemeh Sangghaleh, Anna Fucikova, and Jan Linnros. Biexciton emission as a probe of auger recombination in individual silicon nanocrystals. *The Journal of Physical Chemistry C*, 119(13):7499–7505, 2015.

[45] Anahita Mani, Joop Schoonman, and Albert Goossens. Photoluminescence study of sexithiophene thin films. *The Journal of Physical Chemistry B*, 109(11):4829–4836, 2005.

[46] OV Mikhnenko, F Cordella, AB Sieval, JC Hummelen, PWM Blom, and MA Loi. Temperature dependence of exciton diffusion in conjugated polymers. *The Journal of Physical Chemistry B*, 112(37):11601–11604, 2008.

[47] Pedro Henrique de Oliveira Neto and Leonardo Evaristo de Sousa. Activation energies and diffusion coefficients of polarons and bipolarons in organic conductors. *The Journal of Physical Chemistry A*, 122(28):5925–5930, 2018.

[48] Clemens Simbrunner, Gerardo Hernandez-Sosa, Francesco Quochi, Gunther Schwabegger, Chiara Botta, Martin Oehzelt, Ingo Salzmann, Tatjana Djuric, Alfred Neuhold, and Roland Resel. Color tuning of nanofibers by periodic organic–organic hetero-epitaxy. *ACS nano*, 6(6):4629–4638, 2012.

[49] Aurora Munoz-Losa, Carles Curutchet, Brent P Krueger, Lydia R Hartsell, and Benedetta Mennucci. Fretting about fret: failure of the ideal dipole approximation. *Biophysical journal*, 96(12):4779–4788, 2009.

[50] Kim F Wong, Biman Bagchi, and Peter J Rossky. Distance and orientation dependence of excitation transfer rates in conjugated systems: beyond the förster theory. *The Journal of Physical Chemistry A*, 108(27):5752–5763, 2004.

[51] Richard R Lunt, Jay B Benziger, and Stephen R Forrest. Relationship between crystalline order and exciton diffusion length in molecular organic semiconductors. *Advanced Materials*, 22(11):1233–1236, 2010.

[52] Sébastien Faure, Christine Stern, Roger Guilard, and Pierre D Harvey. Role of the spacer in the singlet- singlet energy transfer mechanism (förster vs dexter) in cofacial bisporphyrins. *Journal of the American Chemical Society*, 126(4):1253–1261, 2004.

[53] Pedro Henrique de Oliveira Neto, Demetrio A da Silva Filho, Wiliam F da Cunha, Paulo H Acioli, and Geraldo Magela e Silva. Limit of exciton diffusion in highly ordered π-conjugated systems. *The Journal of Physical Chemistry C*, 119(34):19654–19659, 2015.

[54] Gleb M Akselrod, Parag B Deotare, Nicholas J Thompson, Jiye Lee, William A Tisdale, Marc A Baldo, Vinod M Menon, and Vladimir Bulović. Visualization of exciton transport in ordered and disordered molecular solids. *Nature communications*, 5:3646, 2014.

[55] Lekshmi Sudha Devi, Mohammad K Al-Suti, Carsten Dosche, Muhammad S Khan, Richard H Friend, and Anna Köhler. Triplet energy transfer in conjugated polymers. i. experimental investigation of a weakly disordered compound. *Physical Review B*, 78(4):045210, 2008.

[56] Yasunari Tamai, Yuu Matsuura, Hideo Ohkita, Hiroaki Benten, and Shinzaburo Ito. One-dimensional singlet exciton diffusion in poly (3-hexylthiophene) crystalline domains. *The journal of physical chemistry letters*, 5(2):399–403, 2014.

[57] M. J. Frisch, G. W. Trucks, H. B. Schlegel, G. E. Scuseria, M. A. Robb, J. R. Cheeseman, G. Scalmani, V. Barone, G. A. Petersson, H. Nakatsuji, X. Li, M. Caricato, A. V. Marenich, J. Bloino, B. G. Janesko, R. Gomperts, B. Mennucci, H. P. Hratchian, J. V. Ortiz, A. F. Izmaylov, J. L. Sonnenberg, D. Williams-Young, F. Ding, F. Lipparini, F. Egidi, J. Goings, B. Peng, A. Petrone, T. Henderson, D. Ranasinghe, V. G. Zakrzewski, J. Gao, N. Rega, G. Zheng, W. Liang, M. Hada, M. Ehara, K. Toyota, R. Fukuda, J. Hasegawa, M. Ishida, T. Nakajima, Y. Honda, O. Kitao, H. Nakai, T. Vreven, K. Throssell, J. A. Montgomery, Jr., J. E. Peralta, F. Ogliaro, M. J. Bearpark, J. J. Heyd, E. N. Brothers, K. N. Kudin, V. N. Staroverov, T. A. Keith, R. Kobayashi, J. Normand, K. Raghavachari, A. P. Rendell, J. C. Burant, S. S. Iyengar, J. Tomasi, M. Cossi, J. M. Millam, M. Klene, C. Adamo, R. Cammi, J. W. Ochterski, R. L. Martin, K. Morokuma, O. Farkas, J. B. Foresman, and D. J. Fox. Gaussian16 Revision B.01, 2016. Gaussian Inc. Wallingford CT.

[58] Demetrio A da Silva Filho, Rainer Friedlein, Veaceslav Coropceanu, Gunnar Öhrwall, Wojciech Osikowicz, Christian Suess, Stacey L Sorensen, Svante Svensson, William R Salaneck, and Jean-Luc Brédas. Vibronic coupling in the ground and excited states of the naphthalene cation. *Chemical Communications*, (15):1702–1703, 2004.

[59] F Heisel, JA Miehe, M Schott, and B Sipp. Measurement of singlet exciton diffusion coefficient in the c-direction in crystalline naphthalene. *Molecular Crystals and Liquid Crystals*, 41(9):251–255, 1978.

[60] Mendel D Cohen, Eugenia Klein, and Zvi Ludmer. Micromeasurements of exciton diffusion lengths in single crystals of anthracene. *Chemical Physics Letters*, 37(3):611–613, 1976.

[61] Donato Donati and John O Williams. Exciton diffusion lengths for pure and doped anthracene single crystals from microscopic measurements. *Molecular Crystals and Liquid Crystals*, 44(1-2):23–32, 1978.

[62] G Vaubel and H Baessler. Diffusion of singlet excitons in tetracene crystals. *Molecular crystals and liquid crystals*, 12(1):47–56, 1970.

[63] Seunghyup Yoo, Benoit Domercq, and Bernard Kippelen. Efficient thin-film organic solar cells based on pentacene/c 60 heterojunctions. *Applied Physics Letters*, 85(22):5427–5429, 2004.

[64] DZ Garbuzov, V Bulović, PE Burrows, and SR Forrest. Photoluminescence efficiency and absorption of aluminum-tris-quinolate (alq3) thin films. *Chemical Physics Letters*, 249(5-6):433–437, 1996.

[65] Josiah A Bjorgaard and Muhammet Erkan Köse. Simulations of singlet exciton diffusion in organic semiconductors: a review. *RSC Advances*, 5(11):8432–8445, 2015.

[66] Peter Peumans, Aharon Yakimov, and Stephen R Forrest. Small molecular weight organic thin-film photodetectors and solar cells. *Journal of Applied Physics*, 93(7):3693–3723, 2003.

[67] D Kurrle and J Pflaum. Exciton diffusion length in the organic semiconductor diindenopery-lene. *Applied Physics Letters*, 92(13):117, 2008.

[68] Michael H. Stewart, Alan L. Huston, Amy M. Scott, Eunkeu Oh, W. Russ Algar, Jef-frey R. Deschamps, Kimihiro Susumu, Vaibhav Jain, Duane E. Prasuhn, Juan Blanco-Canosa, Philip E. Dawson, and Igor L. Medintz. Competition between frster resonance energy transfer and electron transfer in stoichiometrically assembled semiconductor quan-tum dotfullerene conjugates. *ACS Nano*, 7(10):9489–9505, 2013.

[69] Pavel Moroz, Zhicheng Jin, Yuya Sugiyama, D'Andree Lara, Natalia Razgoniaeva, Mingrui Yang, Natalia Kholmicheva, Dmitriy Khon, Hedi Mattoussi, and Mikhail Zamkov. The competition of charge and energy transfer processes in donor-acceptor fluorescence pairs: Calibrating the spectroscopic ruler. *ACS nano*, 2018.

[70] Veaceslav Coropceanu, Jean-Luc Brédas, and Shafigh Mehraeen. Impact of active layer morphology on bimolecular recombination dynamics in organic solar cells. *The Journal of Physical Chemistry C*, 121(45):24954–24961, 2017.